INSIGHTS INTO ALKALI-SILICA REACTION AND DELAYED ETTRINGITE FORMATION THROUGH ADVANCED CHARACTERIZATION TECHNIQUES

A Dissertation
Presented to
The Academic Faculty

by

Mohammad Mehdi Niki Rashidi

In Partial Fulfillment
of the Requirements for the Degree
Doctor of Philosophy in the
School of Civil and Environmental Engineering

Georgia Institute of Technology
May 2018

INSIGHTS INTO ALKALI-SILICA REACTION AND DELAYED ETTRINGITE FORMATION THROUGH ADVANCED CHARACTERIZATION TECHNIQUES

Approved by:

Dr. Kimberly E. Kurtis, Advisor
School of Civil and Environmental Engineering
Georgia Institute of Technology

Dr. Laurence J. Jacobs, Advisor
School of Civil and Environmental Engineering
Georgia Institute of Technology

Dr. Jin-Yeon Kim
School of Civil and Environmental Engineering
Georgia Institute of Technology

Dr. Reza Zoughi
School of Electrical and Computer Engineering
Missouri University of Science and Technology

Dr. Yuanzhi Tang
School of Earth and Atmospheric Sciences
Georgia Institute of Technology

Date Approved: December 8, 2017

To my beloved family

ACKNOWLEDGEMENTS

Throughout my Ph.D. studies, I was honored to work with passionate, knowledgeable, and caring individuals whose support extended beyond my academic life. The people who played a significant role in my personal, interpersonal and professional developments, believed in me when I doubted my capabilities, and filled me with love, hope, and happiness. It is hard to put my sincere gratitude into words, but it is all I got: thank you.

My sincerest thanks goes to my dear advisors: Kim Kurtis and Larry Jacobs. You made my Ph.D. studies an unforgettable experience. I am proud of my dissertation, which is the result of your valuable advice while giving me the freedom to explore and think. I will not forget the amazing moments including the end of semester gatherings at Dr. Kurtis house, the pizza parties at Antico, and coffee and ice cream runs. Thank you Jin-Yeon Kim for your invaluable advice, detailed conversations, and helping me with experiments. Your knowledge about the theory and experiments broadened my view and made me a better researcher. During my Ph.D. journey, when I was lost in the details of my research, you helped me to see the big picture, ask the right question, and organize my thought process. I also appreciate you for reading my paper drafts over and over.

I would also like to appreciate Dr. Zoughi and Dr. Tang for serving on my committee. Since the beginning of my Ph.D. studies, Dr. Zoughi's comments on the microwave materials characterization measurements brought a new perspective into our collaborative research and opened new doors for further studies. Thank you Dr. Tang for the geochemistry class. It provided me the fundamentals for the deeper understanding of

silicates. Your time and input both during my dissertation proposal and the final version of the dissertation are highly appreciated.

Working on a multidisciplinary research project, I was honored to work with researchers outside the civil engineering department. I would like to thank our collaborators at Missouri Science and Technology, Dr. Kristen Donnell and Dr. Ashkan Hashemi, for their excellent research efforts. I would also appreciate Dr. Johannes Leisen, the research scientist at the Georgia Tech nuclear magnetic resonance (NMR) center, for his help and insights during the NMR measurements. I would like to thank Dr. Chetali Gupta for the rheological measurements of alkali-silicate samples. Thank you Dr. Changwoo Do, the scientist for the extended q-range small-angle neutron scattering (EQ-SANS) diffractometer, for your help in analyzing SANS results. This dissertation would not be possible without your contributions.

I would also like to thank the Civil and Environmental Engineering (CEE) department at Georgia Tech for creating a diverse and inclusive environment. The help of the staff at the business office, building support office, front office, and student service office is highly appreciated. Especially, I would like to thank Robert Simon for his valuable advice on the graduate program. Thank you Daniela Estrada for being an amazing friend, and keeping the track of all the paperwork required for the graduation of graduate students. You are an asset to the CEE department and student service office.

I would like to acknowledge the funding resources of this research including National Science Foundation (NSF), Georgia Department of Transportation (GDOT), Barrier One International (BOI), and U.S. Army Engineer Research and Development Center (ERDC).

I am also grateful to be the recipient of the Sam Nunn Security Program fellowship, Anderson fellowship, and the American Society of Nondestructive Testing (ASNT) student travel grant award.

I was fortunate to have known talented students at Georgia Tech. My fellow students patiently shared their knowledge and experience with me and we made life-long friendships. I am thankful to Mr. Marc Knapp for starting on the alkali-silica reaction (ASR) project before I join the research group. His diligent work in the microstructural characterization of cement-based materials is highly appreciated. My special thanks goes to Dr. Alvaro Paul. During my Ph.D. studies, we worked on several research projects together. Through insightful discussions, valuable inputs, and different perspectives, we have co-authored several publications. I would also like to acknowledge Dr. Behnaz Zaribaf. Her presence made the office a better place. Thank you Mr. Lawrence Wolffis, the undergraduate researcher, for all of your hard work in our lab. I would like to thank the former and current group members including Dr. Amal Jayapalan, Dr. Passarin Jongvisuttisun, Dr. Chris Shearer, Dr. Nathan Mayercsik, Dr. Elizabeth Nadelman, Dr. Bradley Dolphyn, Dr. Lisa Burris, Dr. Giovanni Loreto, Dr. Katie Matlack, Dr. David Torello, Mr. Ahmad Shalan, Ms. La Sasha Walker, Mr. Prasanth Alapati, Ms. Natalia Cardelino, Mr. William Cole Spencer, Mr. Bill Jin, Mr. Scotty Smith, Mr. Daniel Benkeser, Ms. Katie Scott, and “the Germans”. I also like to thank visiting scholars and students including Dr. Burak Uzal, Ms. Francesca Lolli, and Ms. Molly Canet, as well as the undergraduate students. Thank you Mahdi Roozbahani and Esmaeel Bakhtiary for the afternoon chats.

Last but not least, my sincere thanks goes to my family for their understanding, support, and encouragement throughout my whole life. I will be always grateful to my parents (Mehri and Hamid), brothers (Hadi and Javad), and grandparents (Fatemeh and Zahra) for their endless love and encouragements. I hope my current and future achievements put a smile on their faces.

TABLE OF CONTENTS

LIST OF TABLES

LIST OF FIGURES

LIST OF SYMBOLS AND ABBREVIATIONS

A	acceleration amplitude
A^+	Monovalent alkali cation
A^{n+}	Cation with charge $n+$
A_1	Amplitude of the first harmonic wave
A_2	Amplitude of the second harmonic wave
C	Number fraction
D	Mass fractal dimension
D_s	Surface fractal dimension
E_0	Linear elastic modulus
f	Resonance frequency at the strain/acceleration amplitude
f_0	Linear resonant frequency
$F(q)$	form factor
$I(q)$	Scattering intensity
I_{IS}	Scattering intensity of isolated structures
I_{MFA}	Scattering intensity of mass fractal agglomerates
K	Scattered wave vector
K_0	Incident wave vector
$(Na_2O)_e$	Alkali equivalent
$\langle N \rangle$	Number of scattering structures per unit volume
q	Scattering vector
q_{ip}	Scattering vector at the initiation of Porod region

R_s	Radius of smallest structure
S	Total surface area
sgn	Signum function
$S(q)$	structure factor
S_s	Standard deviation of slope
T	Time
T_2	spin-spin relaxation time
$1/T_2^*$	Measured spin-spin relaxation rate
V	Volume
V_0	Sample volume
W_1	Fraction of free water
X	Propagation distance
α	Hysteresis nonlinearity parameter
α'	(Hysteresis) average nonlinearity parameter
β	Quadratic nonlinearity parameter
Γ	Gamma function
δ	Cubic nonlinearity parameter
$\Delta\varepsilon$	Strain amplitude
ε	Strain
$\dot{\varepsilon}$	Strain rate
λ	Wavelength
η_{sp}	Specific viscosity
2θ	Scattering angle
κ	wavenumber

v_1	Average sample volume per scatterer.
ξ	Correlation length
ρ	Scattering length density
ρ_0	Scattering length density of a solvent
σ	Stress

ABBREVIATIONS

AIC	Akaike information criterion
AS	Acidic sand
AMBT	Accelerated mortar bar test
ASR	Alkali-silica reaction
ASTM	American Society for Testing and Materials
CPMG	Carr-Purcell-Meiboom-Gill
CPT	Concrete prism test
CS	Control sand
DEF	Delayed ettringite formation
DLA	Diffusion-limited aggregation
DLCA	Diffusion-limited Cluster aggregation
DRI	Damage rating index
EDS	Energy dispersive X-ray spectroscopy
EQ-SANS	Extended q-range small angle neutron scattering
FFT	Fast Fourier transform
ITZ	Interfacial transition zone
MS/s	Mega samples per second

NIRAS	Nonlinear impact resonance acoustic spectroscopy
NMR	Nuclear magnetic resonance
RLCA	Reaction-limited cluster aggregation
SANS	Small-angle neutron scattering
SAS	Small-angle scattering
SCMs	Supplementary cementitious materials
S/A	Silica-to-alkali molar mass ratio
s/c	Sand-to-cement mass ratio
UV-Vis	Ultraviolet visible spectrophotometer
VP-SEM	Variable pressure scanning electron microscopy
W/A	Water-to-alkali molar mass ratio
w/c	Water-to-cement mass ratio
XRD	X-ray diffraction

SUMMARY

Alkali-silica reaction (ASR) and delayed ettringite formation (DEF) are expansive chemical reactions, which can damage concrete structures. However, for both ASR and DEF, the relationships between constituent materials, microscale damage propagation, and bulk expansion are not well understood. To address these knowledge gaps, this study quantifies ASR and DEF-induced damage at the microscale by nonlinear impact resonance acoustic spectroscopy (NIRAS), and when augmented with data from other standard and advanced materials characterization approaches, provides a basis for the new understanding of the factors influencing the extent and rate of damage by these reactions.

This dissertation makes three main contributions. First, the influence of ASR gel composition on its structure and the potential for expansion is explored through the characterization of lab-produced samples by small-angle neutron scattering, ^{1}H nuclear magnetic resonance relaxometry, and rheological measurements. Relying upon that improved understanding of the effects of gel composition along with an understand physics of nonlinear acoustic measurements, in the second part, a hypothesis is presented for interpreting the relationship between measured expansion and temporal material nonlinearity. In the third part, a similar approach is used to explore the relationship between compositional and environmental factors, and microscale damage and expansion derived from DEF.

CHAPTER 1. INTRODUCTION

Better understanding of degradation mechanisms in cement-based materials will allow for the design of more durable new structures, improved repair and mitigation strategies, and more accurate assessment of the remaining life of existing concrete infrastructure. Among the degradation mechanisms, expansive deleterious chemical reactions such as alkali-silica reaction (ASR) and delayed ettringite formation (DEF) significantly contribute to the degradation of concrete structures.

The deleterious ASR occurs between poorly crystalline or amorphous siliceous minerals in some aggregates and the alkaline pore solution of cement-based materials to produce ASR gel. In the presence of sufficient water (i.e., internal relative humidity $\geq$ 85%) (Figure 1), the gel product swells and can lead to expansion and cracking in cement-based materials (Figure 2), ultimately compromising the service life of the affected concrete infrastructure. In particular, critical infrastructure such as bridges, pavements (including airfield pavements), hydrostructures, and nuclear power plants are prone to ASR, due to (1) the availability of water, which promotes ASR gel expansion, (2) the use of massive amounts of regionally sourced aggregates, which may contain reactive minerals, and (3) the lengthy intended service life of these critical structures. For instance, by 1995, 100+ dams and spillways were significantly damaged by ASR worldwide [1], with this number significantly increasing as infrastructure ages and more ASR is detected. Recently, it has been learned that irradiation effects can contribute to increasing the vulnerability of nuclear power plants to ASR [2,3]. Gamma irradiation favors ASR by increasing disorders in the structure of siliceous minerals present in aggregates, weakening the bulk concrete structure

by increasing the volume of aggregates and inducing microcracks in the paste; these effects allow for increased intrusion of external moisture and alkali ions and decrease the stiffness and tensile capacity of the concrete to resist expansion [4,5]. At least one nuclear structure is reported to be ASR-affected (i.e., Seabrook [6]), despite that aggregates used in the construction of those structures were deemed as potentially innocuous. Together, the increasing incidence of ASR, especially in critical structures, demonstrates the need for a more fundamental understanding of the reaction, as well as its damage mechanisms and damage accumulation rate.

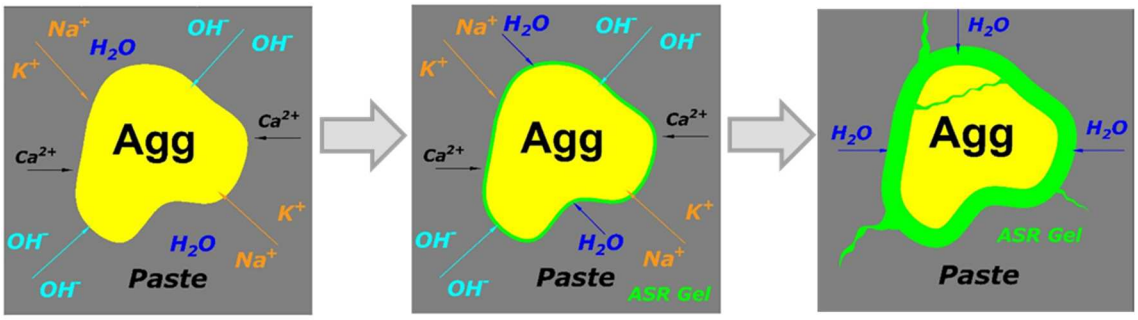

Figure 1. Formation of ASR gel, reproduced from [7].

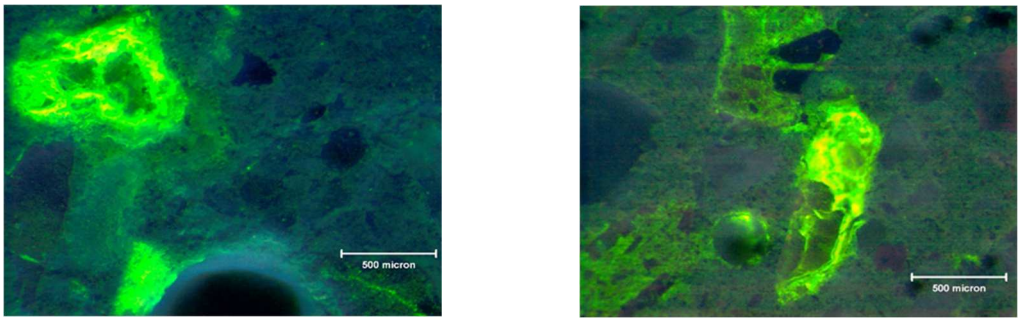

Figure 2. Fluorescence of ASR gel stained with uranyl acetate, under short-wave UV light [8].

Delayed ettringite formation (DEF) is often associated with the later formation of ettringite within concrete or mortar exposed to high temperatures during early stages of cement hydration and can lead to expansion, cracking, and loss of mechanical properties and durability in cement-based materials. DEF has been noted in precast concrete when steam and high-temperature curing are used, and in mass concrete elements, where the evolved heat during cement hydration can result in high internal temperatures if improperly designed [9–12]. DEF and ASR are often found in the field concrete together, contributing to the degradation of cement-based materials [10]. Compared to ASR, DEF is a less-studied subject with most DEF studies have focused on the binder chemistry and exposure condition, while the role of aggregate mineralogy on expansion remains poorly understood. Furthermore, the lack of a standard test method to investigate the potential for DEF-expansion of cement-based materials necessitates further study in this area.

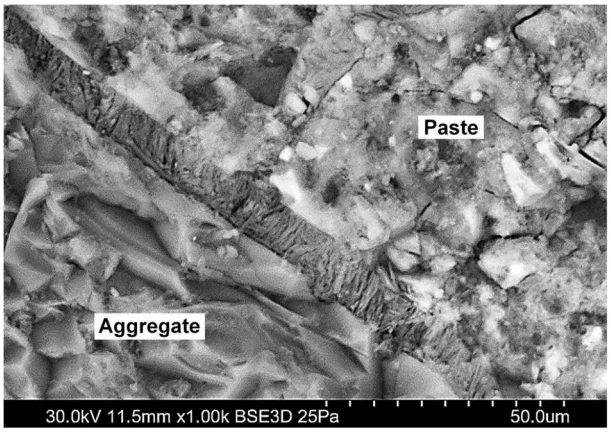

Figure 3. SEM image of ettringite filling the gap between paste and aggregate in the DEF-affected mortar [13].

1.1 Motivation

Despite numerous studies on ASR and DEF affected cement-based materials, the relationship between microstructural evolution, expansion, and damage is not well understood. To provide better insights into these reactions, this dissertation quantifies microscale damage using a nonlinear resonance acoustic technique, nonlinear impact resonance acoustic spectroscopy (NIRAS), and uses various characterization techniques to draw connection between the microstructural features and the properties of reaction products at multiscale, and the measured damage. For instance, for ASR and DEF affected materials, Figure 4 shows the role of reaction products in the NIRAS results.

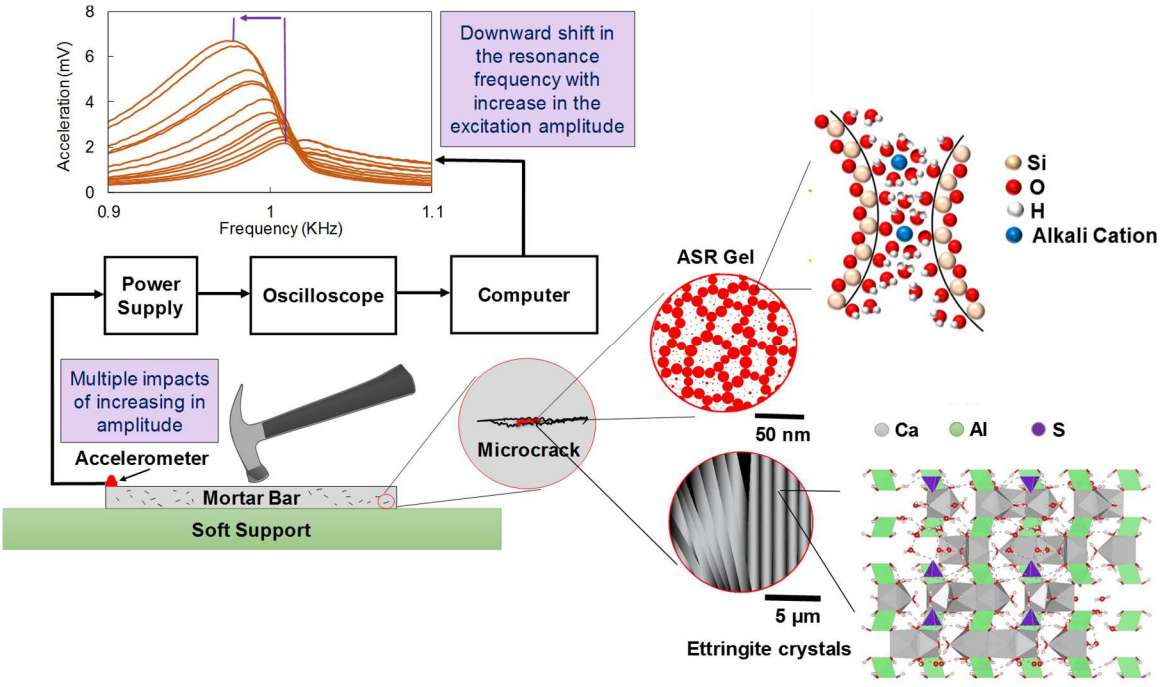

Figure 4. The connection of damage—measured by the downward shift in the resonance frequency of an ASR- and DEF-affected mortar bar during NIRAS measurements—and the properties of reaction products.

NIRAS is an efficient nondestructive measurement technique for the evaluation of microstructural defects in cement-based materials. The nondestructive nature of this technique allows for the temporal measure of damage as it accumulates. Furthermore, compared to the linear acoustic techniques, this technique shows a significantly higher sensitivity to the presence of microcracks. For instance, the ratio of relative increase in the hysteresis nonlinearity measured by NIRAS to the relative decrease in the dynamic elastic modulus for the ASR-affected concrete may exceed two orders of magnitude [14].

However, correlating NIRAS results to the number of a specific microstructural feature, such as the amount of microcracking, is challenging. In fact, rather than directly quantifying flaws, NIRAS evaluates the state of defects—including the interfacial transition zone (ITZ), microcracks, or any discontinuity in which asperities can be induced to vibrate—by capturing the nonlinear response of the material, which is caused by the energy dissipation at the microcracks' surfaces during the resonance test [15]. Clearly, the energy dissipation, which shows itself by the downward shift in the resonance frequency of a sample (Figure 4), not only depends on the properties of microcracks (i.e., surface morphology), but also the properties of reaction products within them. This effect is more significant in measuring the acoustic nonlinearity of expansive deleterious chemical reactions such as ASR and DEF, where cracks are at least partially filled with reaction products (Figure 4). As a result, an improved understanding of microscale damage measured by nonlinear resonance techniques requires knowledge about the underlying physics of nonlinear acoustics and the properties of reaction products. Compared to ettringite, which has a known composition, and crystalline structure, the composition, structure, and expansivity of ASR gel can vary through the same sample. To better

understand the gel properties, Chapter 5 presents the role of composition in the ASR mixes, while Chapter 2 includes the underlying physics of acoustic nonlinearity during the resonance techniques. Based on the above explanation, this dissertation follows three objectives.

1.2 Objectives

1.2.1 Objective 1: To understand the role of composition on the ASR gel structure and damage

To develop better understanding of the role of ASR composition on the gel structure, water-binding ability, and rheological properties, lab-produced ASR samples were prepared at various silicate content and differed in the type of alkali cations (Na^+ versus K^+). Samples were tested using small angle neutron scattering (SANS) to provide structural information, proton nuclear magnetic resonance (^1H NMR) relaxometry for examining the water binding ability, and dynamic viscosity measurements to identify their rheological behavior.

1.2.2 Objective 2: To better understand the relationship between expansion, acoustic nonlinearity, and microstructural distress due to ASR

To address this objective, mortars with potentially reactive and innocuous aggregates were cast and exposed to the accelerated mortar bar test condition. Expansion and acoustic nonlinearity of samples were measured daily, while the microstructural damage was quantified by performing damage rating index (DRI) on the sections of mortar cut on days six, ten, and fourteen of exposure. Based on the knowledge developed in

Objective 1, and the data provided in the literature, Chapter 6 presents a hypothesis to interpret the nonlinear acoustic measurements on the ASR-affected cement-based materials

1.2.3 Objective 3: To better understand the progression of DEF-associated damage

To address this objective, mortars were prepared with cements of varying composition and two types of aggregates, and exposed to the early-age high-temperature curing and subsequent 23 °C limewater exposure. Along with expansion measurements, the acoustic nonlinearity of samples was measured periodically over more than a year, as detailed in Chapter 7.

1.3 Dissertation Structure

This dissertation is organized as follows. This chapter introduces the research problem and identifies the goals. Chapter 2 provides a literature review on the chemistry of ASR and DEF, and the nonlinear acoustic measurements on the ASR-affected cement-based materials. It explains the underlying physics of materials' nonlinearity and the techniques to capture it. Chapter 3 contains the materials and techniques used to achieve the research goals. It provides information on the sample preparation and experimental procedure. Chapter 4 includes the theoretical background on SANS required for the analysis of scattering results of ASR products. Chapter 5 addresses Objective 1, Chapter 6 focuses on Objective 2, and Chapter 7 deals with Objective 3. Chapter 8 summarizes the research findings and suggests opportunities for future work. In an Appendix, the performance of NIRAS on the ASR-affected samples prepared for microwave materials characterization measurements are detailed. The Appendix creates opportunities for the multiphysics study of cement-based materials on the same sample.

CHAPTER 2. LITERATURE REVIEW

2.1 Overview

This chapter provides a literature review on the chemistry of ASR and DEF, and their mechanism of damage accumulation. It also reviews the nonlinear acoustic approaches to detect the microcracks due to ASR. Through identification of knowledge gaps in the literature and the approach that this study takes to fill them, this chapter demonstrates the importance of the contribution of this dissertation to the body of knowledge.

2.2 Alkali-Silica Reaction (ASR)

ASR was first found in 1940 by Stanton [16], who observed expansion for concrete containing high alkaline cement and reactive siliceous minerals, such as opal. Later, Glasser and Kataoka [17] proposed a two-stage process for ASR. Based on their model, in the first step, hydroxyl ions react with the reactive silica, in which Na^+ or K^+ creates bond with silicate oxide to form ASR gel. That is either by ionization of surface of silanol groups:

$$\equiv Si-OH + A^+OH^- \rightarrow Si-O^-A^+ + H_2O \quad (1)$$

where A is a monovalent alkali cation, or dissolution of silica by breaking siloxane bonds:

$$\equiv Si-O-Si \equiv + \ 2(A^+OH^-) \rightarrow 2\left(\equiv Si-O^-A^+\right) + H_2O \ \text{[18]} \quad (2)$$

In the second step, the alkali-silica gel produced (shown in the general form as $SiO_2 \cdot (Na_2O)_n.(K_2O)_k.(CaO)_c.(H_2O)_x$, where n, k, c, and x are molar mass ratios) imbibes water from pores in cement paste and expands. While the mechanism of gel expansion is

not quite clear, osmotic pressure and repulsion due to the electrical double layer [19–21] have been proposed. This two-stage model is well accepted among researchers, although fundamental questions about the relationship between the ASR gel composition, the volume of gel produced, and the potential for damage in concrete remain unresolved [17,22–25].

Water and alkali content of concrete play significant roles in ASR. Water transports alkali ions from pores to the reactive regions, and affects the expansivity of ASR gel. ASR-associated degradation was not observed when the relative humidity (RH) was below 80-85% at 20 $^{\circ}$C [26], 80% at 23 $^{\circ}$C [27], and 75% at 38 $^{\circ}$C [28]. As a result, it is generally accepted that the deleterious ASR occurs when internal RH $\geq$ 85%. On the other hand, cement is typically the source of alkali ions present in concrete. However, alkali ions may leach from supplementary cementitious materials (SCMs) typically used as partial replacement of cement, and from aggregates. In addition, alkali ions may come from external sources such as deicing salts and seawater [21]. Therefore, restricting the availability of water and limiting the alkali content of concrete are key strategies for mitigating ASR.

As the tensile stress generated due to the gel expansion exceeds the tensile capacity of concrete (typically less than 8 MPa), microcracking occurs. Microcracks may further coalesce to form larger cracks. This process shows itself at macroscale with the expansion of ASR-affected structural members or the whole structure. However, expansion does not scale up with the amount of reactive silica. The amount of reactive silica yielding to maximum expansion is called the pessimum content [29]. Therefore, concretes containing

a larger amount of reactive silica are not necessary the ones experiencing greater extents of expansion and damage.

The viscosity of gel and the pore connectivity of cement paste affects the tensile stress developed during ASR [21]. To apply significant stresses to cause microcracking, ASR gel should be confined in pores. At the early stages of reactions, when silicate oligomers are small and the viscosity and yield stress of ASR gel is low, ASR gel pressure may be relieved by the movement of gel to adjacent pores. However, as ASR gel moves through pores, it dissolves calcium hydroxide, which is believed to increase the gel viscosity by the aggregation of silicate oligomers or colloidal species in the gel [18]. A high-viscous and high-yield-stress gel and crystallization within the gel (due to the presence of calcium) can apply significant stresses in confined pores, leading to damage [30].

As calcium ion replaces the monovalent cations, the latter will be released to the pore solution for further alkali-silica reaction [21]. Gels with high calcium content have structures similar to calcium-silicate-hydrate (C-S-H) and they are not expansive. The addition of calcium also favors the depolymerization of ASR gel [31,32], which at the atomic scale shows similarities to the kanemite crystal [33,34]. In other words, ASR gel is dominated by a layered structure [31]. Overall, the calcium content of ASR gel seem to follow a spectrum, with the exterior part of a gel is likely higher in calcium and behave similarly to C-S-H. The higher calcium content results in a more open structure of C-S-H than a more polymerized gel [35]. It is hypothesized that the outer porous C-S-H allows for the transport of water while traps silicate structures [36]. With the increase in the concentration of silicate structures nanoscale agglomerates form, which can further connect

to form a macroscopic gel. Since gels with low calcium content and low viscosity can pass through porosities and the high calcium ones are not expansive, ASR gels with intermediate calcium content seem to be the most deleterious ones [30]. In conclusion, in massive concrete structures such as dams, where an only small portion of alkali ions may leach from the structure, and in the presence of sufficient moisture and reactive silica, ASR may continue for a long period as calcium ion replaces monovalent alkali cations, the process also known as alkali recycling [21].

In addition to the exchange of monovalent cations with calcium ion, gel ripening during aging modifies the gel structure [25,37,38]. ASR gel has a heterogeneous structure. It is made of agglomerates, colloidal species, silicate oligomers, and macroscopic gel [25]. In such a heterogeneous material, smaller structures or the tip of agglomerates, which have a higher solubility, can dissolve and deposit on larger structures through the process known as Ostwald ripening [37,38]. This phenomenon can result in the collapse of gel structure, phase separation, and the release of water and alkali ions to the pore solution even without cation exchange with calcium ion [25]. The tendency for phase separation increases with the decrease in the size of alkali cation [39]. Such a behavior shows the important role of composition and aging on the physical and chemical properties of ASR gel.

2.2.1 The role of monovalent alkali cation in ASR

Among gel composition, the effect of alkali cation type (Na^+ versus K^+) on the nucleation and growth, structure, and water-binding ability of alkali-silicate products, and also the influence of these on rheology and swelling characteristics [30,40,41] is not well understood. For instance, the alkali content of cement is generally expressed as the ‘soda’

or Na_2O equivalent, which only differentiates between Na_2O and K_2O based on their molar mass:

$$\left(Na_2O\right)_e = Na_2O + 0.658K_2O \text{ [42]} \quad (3)$$

where 0.658 is the molar mass ratio of Na_2O to K_2O. However, this approach neglects any differences between Na^+ and K^+, including their different (hydrated) ionic radii [43], ability to pair with silicate oligomers [44], dissolution rate of silica [45], and capability to coagulate silicate structures above pH 11 [37], which influence their participation in alkali-silica reaction (ASR) and subsequent ASR gel expansion.

From a practical point of view, these differences among the alkali cations common in cement-based materials are likely to have important influences on ASR, including ASR gel structure and its potential for expansion and damage experienced in the concrete. Also, improved understanding of the role of the alkali cation on ASR can explain the potential differences between gels formed in field concrete and damage propagation in structures (where generally K^+ is the prevalent alkali cation contributed by the cement), versus the gel produced and damage exhibited under laboratory condition (where Na^+ is often the dominant cation) as prescribed by standardized test methods [46–54].

Due to the hydrous and amorphous nature of ASR gel, it is difficult to study the ASR products using traditional techniques, which involve drying. Better understanding of ASR products can be achieved through characterization of ASR sols and gels of varying composition using a variety of complementary techniques: examining nanostructure by small angle scattering (SAS), investigating water-binding ability by ^1H Nuclear Magnetic Resonance (NMR) relaxometry, and evaluating viscosity by measuring dynamic viscosity.

Throughout this dissertation, the term “sol” is attributed to the alkali silicate mixes, where the continuous phase is alkaline solution, and the discrete phase is alkali-silicate structures (Figure 5a); while the term “gel” refers to the mixes, where the continuous phase is alkali-silicate structures, and alkaline solution forms the discrete phase (Figure 5b).

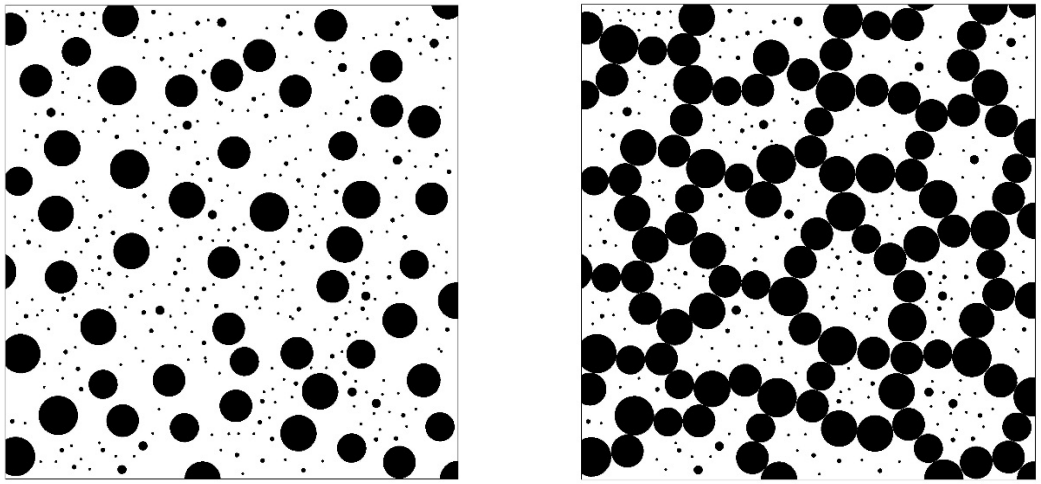

(a) (b)

Figure 5. Schematic representation of (a) sol, and (b) gel (modified from [37]).

SAS can provide structural information about ASR agglomerates [55]. Depending on the scattering vector, *q*, SAS techniques can detect agglomerates within a wide range of 10-10000 Å [55], which is useful for examining the structural differences between water glasses varying in the type of alkali cations [56,57] and monitoring agglomeration process in alkaline-calcium-silicate systems [18]. The nondestructive nature of these techniques and their ability to examine liquid and gel samples minimizes the potential for artifacts due to sample preparation [58].

Nuclear Magnetic Resonance (NMR) techniques can characterize materials at the atomic scales, and they have been used to investigate the structure of lab-produced and field ASR gels. While most studies have focused on investigating the silicon sites in the ASR gels [31,32,59,60], others also used ^{1}H-^{29}Si cross-polarization MAS (CPMAS) [59], and ^{2}H NMR to explore the state of water in alkali-silicate systems [61,62]. Recently, ^{1}H NMR relaxometry is used to monitor the structural evolution during geopolymerization [63], which involves the reaction of aluminosilicates with alkali ions, and it can be viewed as related to ASR. Thus, the combined application of SAS and ^{1}H NMR can provide information about the polymerization of ASR sol and gel and their water-binding ability.

When dried, Na- and K-based gels show similarities such as the domination by Q^3 silicon sites in their NMR results and depolymerization with decrease in Si/(Na or K) [31,32]. However, a similar state of polymerization does not necessarily imply similar behavior of ASR gel. For instance, if alkali cations bridge between silicate structures [37], they will increase the viscosity of alkali-silicate mixes by forming agglomerates, while they may not have a significant effect on the polymerization states of silica. Furthermore, the dried gels do not provide information about the interparticle interactions, which can affect the expansivity of the gel through the electrical double layer [20]. Given the viscosity of potassium silicate sols is significantly lower than sodium silicate ones (at the same silica-to-alkali molar mass ratio) [64], the studying of ASR sol and gel without drying is of great importance.

Previous studies on the role of the alkali cation in the structure of ASR gel (without drying) either focused on water glasses prepared at low or neutral pH, or ASR sols produced with silica-to-alkali molar mass ratio (S/A= SiO_2/(Na, K)$_2$O) up to three

[18,56,57]. Given the wide range of ASR gel composition found in field concrete [31], further studies on the effect of the cation type (Na^+ versus K^+) in lab-produced ASR sols and gels prepared with various S/A and the alkaline solution with pH > 13 is needed. Chapter 5 is intended to fill this gap in the literature, and improve the understanding on the relationship between ASR gel composition, structure, water-binding ability, rheological properties, and the potential to induce damage, using small angle neutron scattering (SANS), ^{1}H NMR, and rheology measurements.

2.3 Delayed Ettringite Formation (DEF)

DEF has been identified as a deleterious expansive chemical reaction associated with crystallization and growth of late-formed ettringite. While the underlying mechanism of expansion remains a subject of ongoing examination, it is generally accepted that i) an early-age curing temperature above 65 °C is necessary for the occurrence of DEF, ii) cement or binder chemistry determines the amount of ettringite formed, and iii) developed stress depends on the microstructure of mortar or concrete [65], as described below.

Early-age high-temperature curing and the availability of moisture play key roles in the development of DEF. In portland cement systems, it is believed that ettringite formed at early-ages decomposes at high temperatures and, as a result, available sulfate and aluminum ions interact with the C-S-H structure [66]. Interaction of aluminum ions with C-S-H depends on the concentration. At low Al/Si ratios in solution (≤ 0.1), aluminum can be incorporated by C-S-H to form C-A-S-H products, while at higher Al/Si precipitation of aluminate hydrates is also expected [67]. Sulfate ions are bound to the C-S-H structure by adsorption and a significant fraction is then released after cooling [65,68]. Subsequently,

in presence of moisture, released sulfate ions combine with alumina sources to form late ettringite in confined spaces, the process that may cause expansion and cracking.

The role of the chemical composition of cement on DEF potential and expansion is not completely clear. However, it is believed that cements with the sulfate-to-alumina ratio (SO_3/Al_2O_3) of lower than 0.45 are not vulnerable to DEF [69], while higher SO_3/Al_2O_3 ratios increase the potential for DEF expansion [70]. Furthermore, fineness, C_3A content, and alkali and sulfate contents of cement play important roles in the potential and extent of the reaction [71–73].

DEF expansion is most commonly attributed to the formation of nanoscopic ettringite crystals under supersaturation in confined nanopores within cement paste. The crystallization can exert expansive pressures over the paste matrix [68,74]. It is generally accepted that the larger crystals of secondary ettringite found in voids, cracks, interfacial transition zone (ITZ) gaps, and deposits in the cement paste do not contribute to the DEF-related expansion. Precipitation of secondary ettringite can be present in samples that do not undergo expansion [65,71,73]. As a consequence of the cement paste expansion, damage observed in DEF-affected samples at later ages of expansion typically includes debonding of the paste-aggregate interface, microcracks around aggregates and within cement paste, deposits of ettringite in the cement paste and inside air voids, and partial or complete filling of cracks and gaps in the ITZ regions with large crystals of ettringite due to Ostwald ripening effect [75,76]. It should be noted that, while the studies on DEF are mainly focused on the effect of cement chemistry, early-age high-temperature curing condition, microcracking due to the crystallization pressure, and the relative humidity of exposure condition, the potential role of ions released from aggregates is not quite

understood. For instance, the sulfate-containing aggregates, which are common in the Middle East [77–79] and can cause internal sulfate attack [78] , and the sulfide-containing ones found in Quebec [80], Kentucky [81], and Connecticut [82] damaging foundation of structures, may act as additional source of sulfate in cement-based materials, and exacerbate the degradation due to DEF. In Chapter 7, the role of sulfate- and sulfide-bearing sand on the DEF-associated expansion is studied.

2.4 Laboratory Test Methods

Susceptibility of aggregates to ASR is typically evaluated in laboratory using ASTM C1260 [48], also known as accelerated mortar bar test (AMBT), and ASTM C1293 [47], also known as concrete prism test (CPT). In AMBT, aggregates are crushed and graded such that 10 percent of the mass is retained on a number 8 (2.36 mm) sieve, 25 percent on a number 16 (1.18 mm) sieve, 25 percent on a number 30 (600 µm) sieve, 25 percent on a number 50 (300 µm) sieve, and 15 percent on a number 100 (150 µm) sieve. Then, 25×25×285 mm mortar bars are prepared at the water-to-cement mass ratio (w/c) of 0.47, and the aggregate-to-cement ratio of 2.25. Mortar bars are cured in moist condition for 24 hours, then demolded and kept in 80 °C deionized water for 24 hours. Afterwards, they are submerged in a 1 M NaOH solution and kept at 80 °C for 14 days. The length of mortar bars is recorded, and if their expansion remains below 0.1% at the end of the test, the aggregate is considered as potentially innocuous. However, if the 14-day expansion of mortar samples exceed 0.1%, ASTM C1293 should be followed to ensure the potential reactivity of an aggregate.

In ASTM C1293, concrete prisms are cast without crushing aggregates, which follow a specific gradation. Furthermore, NaOH pallets are added to the mixing water to increase the alkali equivalent of cement to 1.25% by the weight of cement. Concrete may be prepared at the w/c of 0.42-0.45, demolded after 24 hours from casting, and kept in sealed containers above water at 38 ± 2 °C. Samples are removed after 7 days from casting for the first length measurement and returned to the containers. Aggregates are classified as potentially innocuous if the length change of their corresponding concrete samples does not exceed 0.04% at the end the exposure period (one year). If concrete mixes contain SCMs, the duration of test extends to two years.

In contrast to ASR, there are no standard test methods for investigating the potential for expansion due to DEF. However, the study of DEF-associated expansion commonly includes the exposure of mortar bars to an early-age high-temperature curing cycle, storage in water or limewater, and measurement of length change over time. While no expansion limit or test period has been defined for DEF testing, 0.1% expansion limit (similar to the expansion limit used in ASTM C1260) is typically used to differentiate between deleterious versus non-deleterious DEF-associated expansion in mortars [71,83,84].

2.5 Nonlinear Acoustic Techniques

ASR and DEF can be recognized by expansion, map cracking, and characteristic damage patterns include the presence of reaction products (i.e., ettringite, ASR gel or both) within cracks and around aggregate. In the advanced stages of ASR, even gel exudation at the concrete surface can be apparent [85,86]. Once these features are observed, however, extensive expansion and damage limit repair options and potentially deleterious materials

may have been used in subsequent construction projects. Therefore, early detection of ASR and DEF occurring within concrete would be a significant contribution to the sustainability of concrete infrastructure.

The significant sensitivity of nonlinear acoustic techniques to the microstructural damage makes them advantageous for detecting the degradation of materials at the early stages of the reaction [14,87,88]. These techniques evaluate the state of damage in materials by capturing their nonlinear response under the low amplitude of excitation. In contrast to the undamaged materials, where the stress-strain relationship follows a linear trend, the stress-strain relationship of damaged materials contains nonlinear terms and it can be expressed according to Eq. (4) as [89],

$$\sigma = E_0\left[\varepsilon + \beta\varepsilon^2 + \delta\varepsilon^3 + \alpha\left\{\varepsilon\left(\Delta\varepsilon\right) + \frac{1}{2}\mathrm{sgn}\left(\dot{\varepsilon}\right)\left(\varepsilon^2 - \left(\Delta\varepsilon\right)^2\right)\right\}\right] \tag{4}$$

where σ is stress, E_0 linear elastic modulus, ε strain, β the quadratic nonlinearity parameter, δ the cubic nonlinearity parameter, α the parameter representing the material hysteresis nonlinearity, $\Delta\varepsilon$ the strain amplitude, $\dot{\varepsilon}$ the strain rate, and $\mathrm{sgn}\left(\dot{\varepsilon}\right)$ the signum function, where $\mathrm{sgn}\left(\dot{\varepsilon}\right)=1$ if $\dot{\varepsilon}>0$, $\mathrm{sgn}\left(\dot{\varepsilon}\right)=-1$ if $\dot{\varepsilon}<0$, and $\mathrm{sgn}\left(\dot{\varepsilon}\right)=0$ if $\dot{\varepsilon}=0$. In a microcracked medium, β and δ are mainly due to the nonlinear stiffness of microcracks during acoustic perturbation [90], while α is due to the energy dissipation during this process [89]. However, the measured α and δ parameters may not be independent. For instance, as a mono-harmonic wave with the frequency of ω propagates in a hysteresis media (such as concrete), it generates odd harmonic (ω, 3ω, 5ω, etc.) [91]. As a result, the

measured δ, which is calculated based on the amplitude of the signal at 3ω, is affected by both the stiffness of microcracks and the hysteresis nature of the medium. Since no data on the δ of ASR or DEF-affected cement-based materials has yet published, for the rest of this chapter, only β and α are discussed.

Although in crystalline materials the anharmonicity of lattice and the presence of microstructural features such as dislocations and precipitates increase the nonlinearity parameter β [92], such effects seem to be negligible in cement-based materials, where nonlinearity is mainly due to the high density of microcracks and the deposition of reaction products within them. The contribution of β to the nonlinear response of material can be evaluated by measuring the amplitude of generated second harmonic. In other words, if a damaged material is excited by a harmonic plane wave with the frequency of ω, waves with frequencies of ω, 2ω, 3ω, 4ω, etc. will be generated. The relationship between the amplitude of second harmonic and β can be expressed according to Eq. (5) as [93],

$$\beta = \frac{8A_2}{\kappa^2 A_1^2 x} \tag{5}$$

where A_2 is the amplitude of the second harmonic wave, A_1 the amplitude of the first harmonic wave, κ wavenumber, and x the propagation distance. Due to the high damping ratios of cement-based materials, the amplitudes of high harmonics (4ω, 5ω, etc.) significantly decrease, and they are of less interest. One mechanism that can contribute to the second harmonic generation is the differences in the stiffness of closed versus opened microcracks. This phenomenon is known as the “clapping” effect [94].

The contribution of α, hysteresis nonlinearity parameter, to the nonlinear response of a material can be assessed by measuring the slope of a downward shift in the resonance frequency of a sample versus strain amplitude [89]. In damaged materials, in contrast to undamaged ones, resonance frequency shifts to the lower values with increase in the strain amplitude, and as damage progresses, the increase in the strain amplitude causes a greater downward shift in the resonance frequency. According to Eq. (6), the relationship between the relative change in resonance frequency versus strain amplitude can be represented as [89],

$$\frac{f_0 - f}{f_0} = \alpha \Delta\varepsilon \tag{6}$$

where f_0 is the linear resonant frequency of a sample and f the resonant frequency of the sample at the strain amplitude. Furthermore, since $\Delta\varepsilon$ is directly proportional to the acceleration amplitude, Eq. (6) can be further simplified to Eq. (7) as [14,88,95],

$$\frac{f_0 - f}{f_0} = \alpha' A \tag{7}$$

α' is directly proportional to the hysteresis nonlinearity parameter (α) and A the acceleration amplitude. α' can be evaluated using the NIRAS technique. NIRAS measurements can be performed by the application of several impacts of increasing in amplitude to the midpoint of a sample, and capturing the transient vibration response of the sample in the time domain using an accelerometer located at the end of the sample. Later, the time domain signal is transformed to the frequency domain using fast Fourier transform (FFT), and the slope of a downward shift in the resonance frequency of sample

is calculated. Prior to the first nonlinear acoustic measurement, NIRAS measurements on a linear elastic specimen (i.e., an aluminum bar) matching the geometry of the mortar samples can be used to confirm the linearity of the experimental setup. A typical experimental setup and the nonlinear response of a damaged mortar sample are shown in Figure 6 [13].

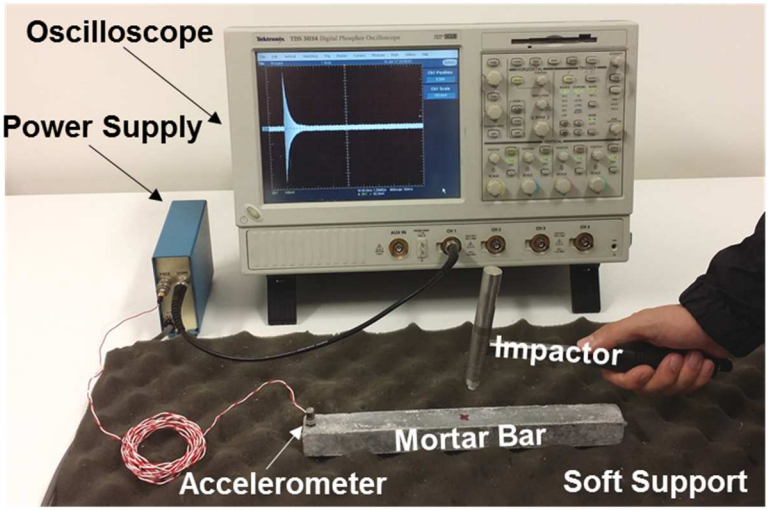

(a)

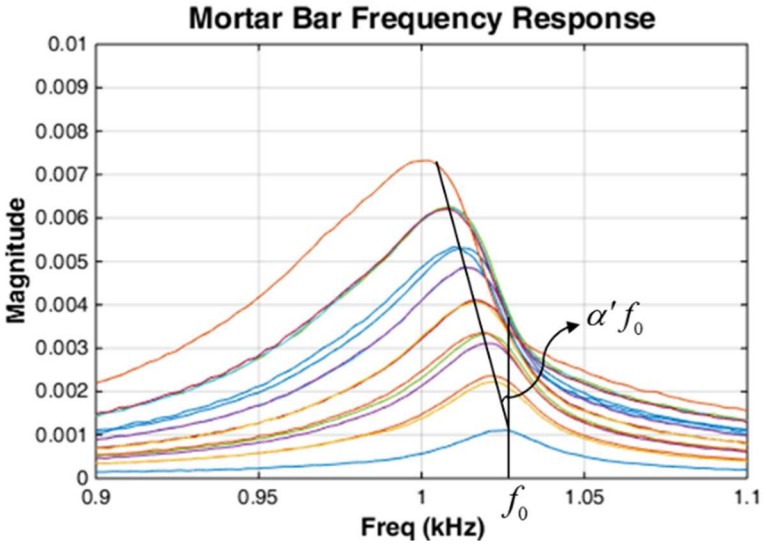

(b)

Figure 6. (a) NIRAS experimental setup, and (b) nonlinear response of an ASR-affected mortar bar.

Characterization of cement-based materials using NIRAS is increasing due to the simple experimental setup, short time of the experiment, and the minimal effect of conditioning [96]. While NIRAS was originally developed to excite the first bending vibration mode of a sample, it was later extended to evaluate the nonlinearity of a material by exciting the longitudinal vibration modes of a sample [14,97,98]. The experimental setup, which involves placing a sample on a soft support and exciting its vibration modes, avoids support-induced vibrations, and the potential nonlinearity at the connection of sample and a hard support. The setup has been mainly used for measuring the acoustic nonlinearity of mortar bars [13,95,97,98] and concrete prisms [14,99–103]. These samples are relatively large, and they remain stable after receiving impacts.

If samples are small and subsequently light, they may bounce off the soft support after receiving an impact (especially during the excitation of bending modes) and distort the received signal. Depending on the sample size, this issue can be resolved by reducing the size of the impactor and impact energy [104,105].

The hysteresis nonlinearity originates from the energy dissipation at the surface of microcracks during acoustic loading and unloading [15,106,107]. Although several mechanisms contribute to the energy dissipation including adhesion and friction hysteresis [108], and the local plasticity of contacts [109], those mechanisms require the relative movement of microcrack asperities. In other words, if reaction products restrain the relative movement of microcrack asperities, hysteresis nonlinearity decreases. Therefore, in the ASR- and DEF-affected cement-based materials, the presence and the physical properties of gel and ettringite within microcracks play a significant role in the nonlinear response of a material.

Slow dynamics is another property that a hysteresis media exhibits. That is if a damaged material is subjected to a high amplitude wave for a long duration (several minutes), its resonance frequency drops, and after removing the excitation, the recovery of resonance frequency versus time follows a logarithmic trend [110]. The slow dynamic behavior of ASR-affected concrete seems to be different from that of a mechanically damaged concrete, presumably due to the presence of ASR gel within microcracks [110].

The nonlinear nature of a damaged material also allows for the nonlinear wave mixing [111] and nonlinear wave modulation spectroscopy (NWMS) techniques [112] to assess the damage level. Due to the presence of β, as two waves with the frequency of ω_1 and ω_2 interact in the medium, the received signal will contain harmonics with the frequencies of $\omega_1, \omega_2,$ and $\omega_1 \pm \omega_2$. The amplitude of the signals with mixed frequencies is directly proportional to the amplitudes and frequencies of the input signals and β [111]. Similarly, in the NWMS techniques, a high-amplitude low-frequency signal (i.e., the response of a material to an impact) interacts with a low-amplitude high-frequency signal and creates signals with mixed frequencies ($\omega_1 \pm \omega_2$). Furthermore, the perturbation of a medium with an impact while the low-amplitude high-frequency signal propagates through it, results in the delay of the received signal as microcracks open [113]. The time shift (TS) technique relates the normalized delay of the received signal to β and strain amplitude.

2.6 Literature Review on the Acoustic Nonlinearity of ASR-Affected Cement-Based Materials

Overall, in the literature, the hysteresis acoustic nonlinearity is assessed by measuring the slope of downward shift in the resonance frequency of a sample with increase in the excitation amplitude [14,87,88,114–118], while the quadratic acoustic nonlinearity is evaluated using a variety of techniques such as wave mixing [111,119], NWMS [112], TS [113], and nonlinear longitudinal and Rayleigh surface waves [120]. Although in all studies acoustic nonlinearity parameters successfully differentiate between the specimens prepared with potentially reactive aggregates versus the ones made with potentially innocuous ones, the trend between temporal β and expansion is substantially different from that of α (or α') and expansion. β tends to increase with expansion (although a slight decrease in β at later ages may be observed [112]), while the hysteresis acoustic nonlinearity has an ascending behavior at early stages of the reaction, and it has a noticeable descending behavior at later ages [88,95,117]. Although cumulative temporal α' shows a strong correlation with expansion [88,95]. The significant differences between the trend in temporal β and α with expansion require an interpretation of data based on the reaction chemistry. In Chapter 6, a hypothesis is presented to explain these different trends.

Overall, due to the increasing trend in the concrete consumption and the depletion innocuous aggregates, the durability concern of cement-based materials will most likely continue to be an important issue in the future, and requires improved understanding of the

reactions, and developing advanced techniques for monitoring current and future infrastructure.

2.7 Summary

This chapter reviewed the current understanding of chemistry and the mechanism of damage in ASR and DEF. The main points of this chapter are as follows:

- Although ASR and DEF have been studied for decades and a general understanding of these reactions exists, several aspects of these reactions at the micro, molecular, and atomic scales need to be further studied. For instance, the relationship between the ASR gel composition, water-binding ability, and expansivity is not well understood.
- Nonlinear acoustic techniques show a significant sensitivity to the presence of microcracks caused by ASR. However, the current state of knowledge remains at the observation level, and the relationship between the nonlinear acoustic results and the chemistry of the reaction is not clear.
- Compared to ASR, DEF is a less studied area, which requires further research to shed light on the role of the cement composition, aggregate types, and exposure condition on the progression of damage.

CHAPTER 3. MATERIALS AND METHODS

3.1 Overview

This chapter describes the materials, sample preparation and exposure, and experimental methods used in this study. Similar to the three Objectives of this dissertation, the materials, and sample preparation and exposure are categorized into three groups including those for the characterization of (a) lab-produced ASR samples, (b) ASR-affected mortars, and (c) DEF-affected mortars. On the other hand, the methods can be common among Objectives. For instance, same experimental setup was used for measuring the expansion and acoustic nonlinearity of ASR- and DEF-affected mortars.

3.2 Materials, Sample Preparation, and Exposure

3.2.1 Lab-produced ASR samples

Lab-produced ASR samples were prepared by combining amorphous fumed silicon (IV) oxide (300–350 m^2/g surface area, Alfa Aesar) with 1.85M NaOH or 1.82M KOH, made with deionized water and ACS-grade reagents. The concentration of alkali cations was slightly different to keep the water-to-alkali molar ratio (W/A) at 58.00, which was selected based on the workability during the preparation of Na-based gels.

Na- and K-based samples were prepared at the S/A of zero to ten. At high S/A (i.e., nine and ten), Na-based mixes formed large precipitates rather than a continuous gel network. Overall, eleven Na-based and eleven K-based mixtures were prepared in sealed polypropylene containers, which were agitated for ten minutes after the addition of fumed

silicon (IV) oxide. This approach follows that of Zhang et al. [121] to synthesize geopolymer samples. Experiments were performed approximately 24 hours after sample preparation.

3.2.2 ASR-affected mortars

3.2.2.1 Materials

3.2.2.1.1 Fine aggregates

Based on the potential reactivity level as defined in ASTM C1260 [48] and field performance history, three sources of natural aggregate (Table 1) from the United States were selected, and graded according to ASTM C1260 [48]. Aggregate used in this study were not washed.

Table 1. Aggregates used in the studying of the ASR-affected mortars.

Aggregate Symbol	**Reactivity***	**Mineralogy**	**Source**
Reactive-1	Potentially Deleterious	Quartzite with smaller amounts of chert	Northeastern Nebraska
Reactive-2	Potentially Deleterious	Quartzite with smaller amounts of chert	South Central Nebraska
Non-Reactive	Innocuous	Mainly quartz	Georgia

* Assessment of reactivity based on field performance and prior ASTM C1260 results.

3.2.2.1.2 Portland cement

A commercially available ASTM C150 Type I cement (Lehigh Cement Company, LLC) with the Bogue potential composition of 42.72% C_3S, 24.77% C_2S, 6.29% C_3A,

12.23% C_4AF, and the equivalent alkali content $(Na_2O)_e$ of 0.80% was used to prepare mortar samples.

3.2.2.2 Sample preparation and exposure

For each aggregate source, four prismatic standard (25×25×285-mm) mortar bars were prepared by mixing aggregate, cement, and deionized water following the proportioning provided by ASTM C1260 [48], and the mixing procedure given in ASTM C305. Mortar bars were cured and exposed to the ASTM C1260 [48] condition.

3.2.3 DEF-affected mortars

3.2.3.1 Materials

3.2.3.1.1 Fine aggregates

Two sources of natural siliceous sand from Georgia were selected in the preparation of mortar bars (Table 2).

Table 2. Aggregates used in the studying of the DEF-affected mortars.

Aggregate Symbol	Mineralogy	Specific Gravity	Fineness Modulus
Control Sand (CS)	Mainly quartz	2.66	2.43
Sulfate- and sulfide-bearing sand (referred to as acidic sand) (AS)	Quartz with a significant portion of alkali feldspars	2.61	2.31

According to the producer, acidic sand contains 0.037% of water-soluble sulfate (SO_4^{2-}) and 0.02% pyritic sulfate. The water-soluble sulfate content was also measured to be 0.031% by mass using an ultraviolet-visible spectrophotometer (UV-Vis) [122].

3.2.3.1.2 Portland cement

Five commercially available cements with a range of compositions were examined to assess varying degrees and rates of the DEF-associated damage. Mortars were prepared from three ASTM C150 Type I cements (labeled as Type I-A, Type I-B, and Type I-C cement), one ASTM C150 Type V cement, and one ASTM C150 Type III cement. The Type V and Type III cements were selected to represent cases of relatively low and high susceptibility to DEF [123], while three compositions of Type I cement provide a range of sulfate, alumina, and C_3A contents (Table 3). Furthermore, all cements are classified as low-alkali cements according to ASTM C150.

Table 3. Oxide analysis and Bogue potential composition of cements used in the studying of the DEF-affected mortars.

Cement Type	**Oxide Analysis (%)**								**SO_3/Al_2O_3**
	SiO_2	Al_2O_3	Fe_2O_3	CaO	MgO	$(Na_2O)_e$	SO_3	LOI	
Type I - A	19.78	4.61	3.37	62.75	3.07	0.49	2.55	2.57	0.70
Type I - B	19.58	4.79	3.38	64.20	1.06	0.49	3.26	2.61	0.87
Type I - C	19.40	5.48	3.33	63.83	0.79	0.53	3.18	1.64	0.74
Type III	19.81	5.52	3.31	63.99	0.79	0.47	4.14	1.67	0.96
Type V	21.10	3.95	4.42	62.49	3.05	0.44	2.35	1.33	0.76

Cement Type	**Bogue Potential Composition (%)**				**Blaine Fineness (m^2/kg)**
	C_3S	C_2S	C_3A	C_4AF	
Type I - A	62.08	9.89	6.50	10.26	393
Type I - B	66.26	6.15	6.97	10.28	413
Type I - C	61.76	9.03	8.88	10.14	401
Type III	56.34	14.29	9.03	10.06	498
Type V	54.50	19.38	2.97	13.45	376

3.2.3.2 Sample preparation and exposure

For each cement and type of sand, ten standard prismatic mortar bars were prepared following the proportions of water, cement, and natural siliceous sand given in ASTM C1038, and the mixing procedure provided in ASTM C305. The w/c was 0.50 and sand-to-cement mass ratio (s/c) was 2.75. Deionized water was used in the preparation of mortars.

Two curing conditions were used in the first 24 hours: half of the specimens were kept in sealed containers at 23 ± 1.5 °C (normally-cured samples), and the other half were exposed to the Kelham high-temperature curing cycle (Figure 7), which is commonly used for examining the potential for DEF (heat-cured samples) [123–125]. Subsequently, all mortars were cured in limewater baths at 23 ± 1.5 °C, with samples prepared from each cement cured separately.

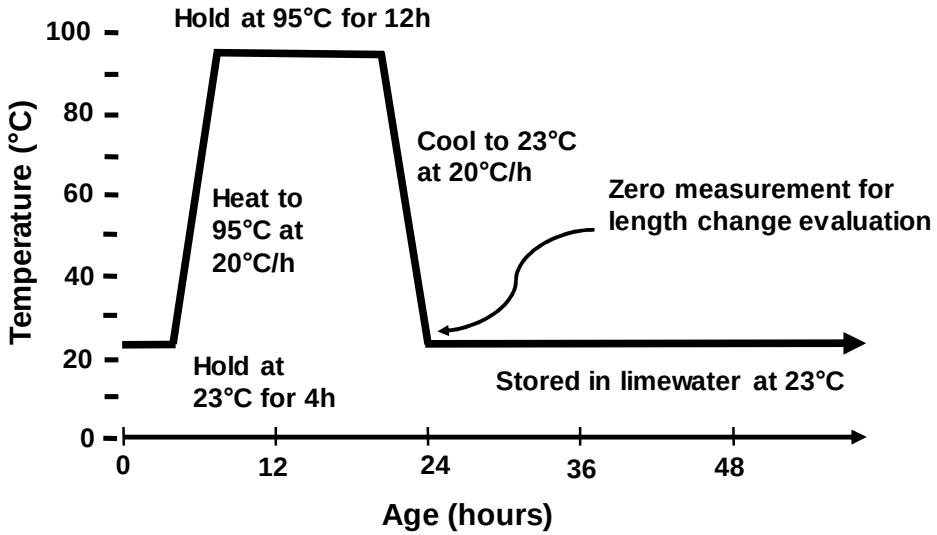

Figure 7. Kelham high-temperature curing cycle (modified from [126]) used in the studying of the DEF-affected mortars.

3.3 Methods

SANS, ^{1}H NMR relaxometry, and dynamic viscosity measurements were applied to the lab-produced ASR samples, while expansion and nonlinear acoustic measurements were performed on mortars. In all measurement results, the length of error bars was equal to one standard deviation.

3.3.1 Small Angle Neutron Scattering (*SANS*)

SANS measurements were performed on the Extended Q-range Small Angle Neutron Scattering Diffractometer (EQ-SANS), beamline 6, at the Spallation Neutron Source at the Oak Ridge National Laboratory. To study the structure of ASR sols over a range of neutron wavelengths, each sample was analyzed at 1.3 m (q-range of 0.06 to 1.5 $Å^{-1}$ and neutron wavelength band λ = 1.0 to 5.1 Å) and 4 m (q-range of 0.01 to 0.4 $Å^{-1}$ and λ = 2.5 to 6.1 Å) sample-to-detector distances. SANS was also performed on a blank sample (containing only deionized water) to ensure constant intensity over a wide range of q.

Data were analyzed according to the process described by Zhao [127], with corrections for inelastic incoherent scattering. Background scattering was determined based on the minimum of scattering intensity, $I(q)$, at large qs, and it was subtracted from the total scattering intensity. Afterward, $I(q)$ of the ASR sols was obtained for the q-range of 0.007 to 0.5 $Å^{-1}$. SANS results were further modeled to extract structural information about the nature and the size of silicate species. Chapter 4 provides background information on the theory of small-angle scattering (SAS), while chapter 5 includes the modeling results.

3.3.2 Proton nuclear magnetic resonance (^{1}H NMR) relaxometry

The spin-spin relaxation time (T_2) of protons present in the samples was monitored using a Maran 23 Ultra, a low-resolution spectrometer operating at a ^{1}H frequency of 23 MHz [128]. The instrument contains a 0.5T permanent magnet and a 25 mm ^{1}H radiofrequency probe operating at a temperature of 30 ± 1 °C. For each test, a 10-mm diameter glass NMR-tube was filled up to the height of 25-30 mm, sealed to prevent water loss during the experiment, and placed in the sample coil. Each experiment took approximately 20 minutes and required no additional sample preparation. The Carr-Purcell-Meiboom-Gill (CPMG) method [129] was used to evaluate T_2. The results of at least two time intervals for CPMG echoes were compared to investigate the potential diffusion effect on the relaxation time, and 32 scans were used for signal averaging. Furthermore, T_2 was calculated by curve fitting using NMRFIT software.

3.3.3 Capillary viscometry

A capillary viscometry technique was used to measure the dynamic viscosity of samples. In this technique, an Ubbelohde viscometer was first thoroughly cleaned using an acid-based glass cleaner and deionized water. Then, using a rubber pump, the sample was pumped into the viscometer up to the demarcation located on the viscometer, and it was then released. The flow time of the fluid between two demarcations was measured. Afterwards, using a calibration table provided by the manufacturer the kinematic viscosity was calculated. The density of the samples was then used to convert the kinematic viscosity into dynamic viscosity. Measurements were repeated five times for each sample at the lab temperature (23±1.5 °C).

3.3.4 Expansion measurements

The length of mortar bars was measured periodically using a comparator conforming ASTM C490 standard. For ASR-affected mortars, the measurements were performed daily during fifteen days (day zero to fourteen) exposure to the ASTM C1260 condition. On the other hand, the expansion of DEF-affected mortars was monitored over more than a year and measurements were performed less frequently (i.e., once per week). Each expansion data point represents the average of at least three identical mortar bars.

3.3.5 Nonlinear acoustic measurements

Nonlinear acoustic measurements were performed by exciting the first bending vibration mode of a sample using the NIRAS experimental setup explained in chapter 2. Samples were tested immediately after removing from the exposure solution. Each measurement took approximately 20-25 minutes, and samples were returned into containers for the continued exposure. Similar to the expansion measurements, the nonlinear acoustic measurements were performed daily on the ASR-affected mortar bars, while less frequently on the DEF-affected ones.

To capture the signal, a high-frequency accelerometer (PCB 353B13) was attached near the end of a mortar bar using an adhesive wax. The accelerometer was connected to a power supply (PCB Piezotronics ICP Power Supply Model 482A06), which was in turn connected to an oscilloscope. A sample's time domain signal was captured at the sampling rate of 1.25 MS/s (mega samples per second) with a 0.4 seconds window, and it was zero padded prior to performing fast Fourier transform. For each sample, at least ten impacts of increasing in amplitude were applied, and the normalized change in the resonance

frequency was calculated. Then, the data of three replicas for each sample set were combined to calculate the acoustic nonlinearity (α'). The standard deviation of α' was determined based on the standard deviation of slope for n data points with (x_i , y_i) coordinates,

$$S_s = \sqrt{\frac{\frac{1}{n-2}\sum_{i=1}^{n}(y_i - \bar{y})^2}{\sum_{i=1}^{n}(x_i - \bar{x})^2}} \tag{8}$$

where S_s is the standard deviation of the slope.

3.3.6 Quantitative petrography analysis using damage-rating index (DRI)

While DRI is generally performed on concrete experiencing ASR in the field [130] or under ASTM C1293 [47] exposure condition, an extension of this quantitative image assessment approach was attempted to evaluate the extent of damage in mortars exposed to the ASTM C1260 condition. DRI evaluates damage through counting the microstructural defects and assigning weights to them, as shown in Table 4**.**

To perform DRI on concrete, a section with the thickness of about 20-30 mm is cut from a cylinder or prism sample. The section is polished, and grid sizes of 15×15 mm^2 are drawn on the sample surface. In each grid, the number of each defect type is counted at the magnification of 16x, multiplied by its weighting factor, and added to each other. The final value is reported per 100 cm^2 [132].

Table 4. Defect scaling factors used for DRI [130,131].

Defect Type	Scaling Factor
Crack in coarse aggregate filled with gel	2
Crack in coarse aggregate without gel	0.25
Crack in cement paste filled with gel	4
Crack in cement paste without gel	2
Reaction rim	0.5
Air void with gel	0.5

To apply DRI technique on mortars, those defect types that related to the coarse aggregate—crack in the coarse aggregate with and without gel—were assigned to the fine aggregate—crack in the fine aggregate with and without gel—while their scaling factors maintained the same. Furthermore, the grid size and magnifications were modified to maintain proportionality to the aggregate size and ASR-induced defects. In concrete, since coarse aggregate contributes to a significant portion of the microstructure, a large grid size of 15×15 mm^2 is needed. However, in mortar, because the microstructure is quite fine, the grid size is decreased to 2×2 mm^2. Furthermore, the magnification is increased from 16x in concrete to 25x in mortar for the better observation of microstructural defects.

For the mortar bars exposed to the ASTM C1260 condition, DRI values at days six, ten, and fourteen of exposure were calculated. At each age, the same sample of each sample set was used for the petrographic examination. To preserve and quantify regions containing gel, highlight cracks, and allow discrimination between defects containing gel and those without gel, sample preparation and imaging were performed in two stages [130,131]. In the first stage, samples were cut from the mortar bars with a low speed, ethanol-cooled

saw. Then, they were polished to 320 grit with ethanol as a lubricant. Polishing samples was limited to minimize the removal of gel, while still allowing high-quality images to be obtained. Afterwards, samples were stained with uranyl acetate to increase the visibility of the ASR gel [133] following the procedure described in [134]. The gel was observed using optical microscopy (Leica DMRE) under a mercury lamp light source. At each age, four sections were cut from each sample type and four images per section were obtained. Overall, sixteen images per sample type per age were taken. Subsequently, grids were overlain on the images and defect counting on two grids per field of view was performed to determine the number of the gel-associated defects. Gel-associated defect categories included cracks in aggregate filled with gel, cracks in cement paste filled with gel, the reaction rim, and air void filled with gel. In the second stage, after washing to remove the stain, samples were vacuum-impregnated with epoxy and polished to 600 grit with water as a lubricant. Images were again acquired under a mercury lamp light source, identical grids to those used in the first stage were overlain on images, and the defects were counted on two grids per field of view. Counting of defect types in the stage one and two was performed on the identical field of view. Defects without gel—cracks in aggregate without gel and cracks in cement paste without gel— were those observed in stage two but not in stage one. Then, the total number of each defect type per grid area was calculated for each sample type. Subsequently, an appropriate scaling factor (as shown in Table 4) was applied to each defect type. DRI values were reported as the average number of defects per 100 cm^2 of grid area [130].

3.4 Summary

This chapter provided details about the materials, mixing procedure and sample preparation, exposure condition, experimental techniques, and the process to obtain measurement parameters.

CHAPTER 4. SMALL ANGLE NEUTRON SCATTERING

4.1 Overview

This chapter provides basic information about the theory of small angle neutron scattering (SANS) and the knowledge required for the modeling of SANS experimental results. In the SANS experiments generally scattering intensity, I (q), versus scattering vector, q, is plotted. These parameters are explained.

4.2 Scattering Vector and Scattering Length Density

In elastic scattering, when a monoharmonic plane incident wave of neutrons with the wave vector K_0 interacts with the nucleus of atom i, it creates a spherically propagating scattered wave. The amplitude of the received scattered wave is proportional to the amplitude of the incident wave, the coherent scattering length of atom i denoted by b_i, and the inverse of the distance ($1/r$) from the atom i to the receiver.

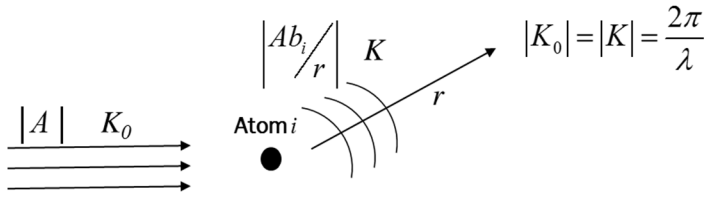

Figure 8. Interaction of an incident wave with atom i, reproduced from [55].

In Figure 8, λ is the wavelength. The differences between the incident and scattered wave vectors (K-K_0) is expressed as scattering vector, q, whose amplitude is proportional to the scattering angle, 2θ .

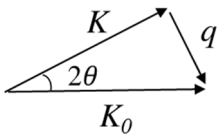

$$|q| = |K - K_0| = \frac{4\pi \sin\theta}{\lambda}$$

Figure 9. Scattering vector.

In practice, since structures consist of a large number of atoms and the scattering length of each atom is small (in the order of 10^{-12} cm), the scattering length density, $\rho(\mathbf{r})$, is defined according to Eq. (9) as,

$$\rho(\mathbf{r}) = \sum_i b_i \delta(\mathbf{r} - \mathbf{r}_i) \tag{9}$$

where $\delta(\mathbf{r} - \mathbf{r}_i) = 0$ at $\mathbf{r} \neq \mathbf{r}_i$, and $\int_V \delta(\mathbf{r} - \mathbf{r}_i)\, d\mathbf{r} = 1$, where V is the volume. For a scatterer made of n identical atoms with scattering length of b (monodisperse system), Eq. (9) simplifies to Eq. (10) as,

$$\rho = \frac{nb}{V} \tag{10}$$

The scattering length density is required to calculate the scattering intensity, which will be explained in the next section.

4.3 Scattering Intensity

Scattering intensity is the flow of scattered energy through a unit area in the direction of q (i.e., the number of scattered neutrons at a scattering vector), and for a monodisperse system, it can be expressed in Eq. (11) [135], as

$$I(q) = \langle N \rangle \langle F(q)^2 \rangle S(q) \tag{11}$$

where $I(q)$ is the scattering intensity, $\langle N \rangle$ the number of scattering structures per unit volume, $F(q)$ the form factor, and $S(q)$ the structure factor. $\langle F(q)^2 \rangle$ depends on the geometry of scatterers, and for structures dispersed in a solvent with scattering length density of ρ_0 can be evaluated according to Eq. (12) as,

$$\langle F(q)^2 \rangle = \left\langle \int_{V_S} \left| [\rho(\mathbf{r}) - \rho_0] e^{i\mathbf{qr}} d\mathbf{r} \right|^2 \right\rangle \tag{12}$$

where V_s is the volume of a structure. For simple geometric structures, Eq. (12) has a closed-form solution. For instance, for spheres, with radius R and scattering length density of ρ, dispersed in a solvent with scattering length density of ρ_0, $\langle F(q)^2 \rangle$ can be expressed in Eq. (13) [135] as,

$$\langle F(q)^2 \rangle = \left\{ \tfrac{4}{3} \pi R^3 (\rho - \rho_0) \left(3 \frac{\sin(qR) - qR\cos(qR)}{(qR)^3} \right) \right\}^2 \tag{13}$$

On the other hand, $S(q)$ depends on the spatial distribution of scatterers, and for isotropic systems, it can be expressed according to Eq. (14) as,

$$S(q) = 1 + 4\pi \langle N \rangle \int_0^\infty (g(r) - 1) r^2 \frac{\sin(qr)}{qr} dr \tag{14}$$

where $\langle N \rangle g(r)$ represents the average number density of scatterers at a distance r from a scatterer located at the origin and $g(r)$ is the radial distribution function [135]. For the simple case of non-penetrating spheres with radius R, $S(q)$ can be evaluated according to Eq. (15) [55] as,

$$S(q) = 1 - 8\frac{V}{\nu_1}\left[3\frac{\sin(2qR) - 2qR\cos(2qR)}{(2qR)^3}\right] \tag{15}$$

where V is the volume of the sphere, and $\nu_1 = \frac{V_0}{N}$, where V_0 is the volume of sample and N the number of spheres. In other words, ν_1 is the average sample volume per sphere. Clearly, in a diluted system, where $\nu_1 \gg V$, $S(q) \simeq 1$.

4.3.1 Scattering from mass fractals

ASR sol and gel have a polymeric structure, and their scattering behavior can be studied using mass fractal structures. In these structures, the relationship between mass distribution, *M*, and distance, *r*, can be represented according to Eq. (16) as,

$$M(r) \sim r^D \tag{16}$$

where *D* is the fractal dimension and it is equal or less than the dimension of space (≤ 3). For individual scatterers connecting to form mass fractal agglomerates, $S(q)$ can be evaluated according to Eq. (17) [135], as

$$S(q) = 1 + \frac{1}{(qR)^D}\frac{D\Gamma(D-1)}{(1+\frac{1}{q^2\xi^2})^{\frac{(D-1)}{2}}}\sin\left[(D-1)\tan^{-1}(q\xi)\right] \tag{17}$$

where *R* is the characteristic dimension of an individual scatterer (i.e., the radius in the case of spheres), Γ the gamma function, and ξ the correlation length representing the pore size within solid mass fractals [136] or the size of an agglomerate [135] (Figure 10). In the range of $1/\xi < q < 1/R$, Eq. (17) simplifies to $S(q) \sim q^{-D}$, and thus the fractal dimension is

equal to the slope of $I(q)$ versus q in the log-log plot [135]. The mass fractal dimension can be considered the generalization of mass distribution in various dimensions. For instance, a fractal dimension of one represents the mass distribution in a dense one-dimensional system. Similarly, in three-dimensional agglomeration regime, the fractal dimension of dense agglomerates can be as large as three, but it decreases for open-structured agglomerates.

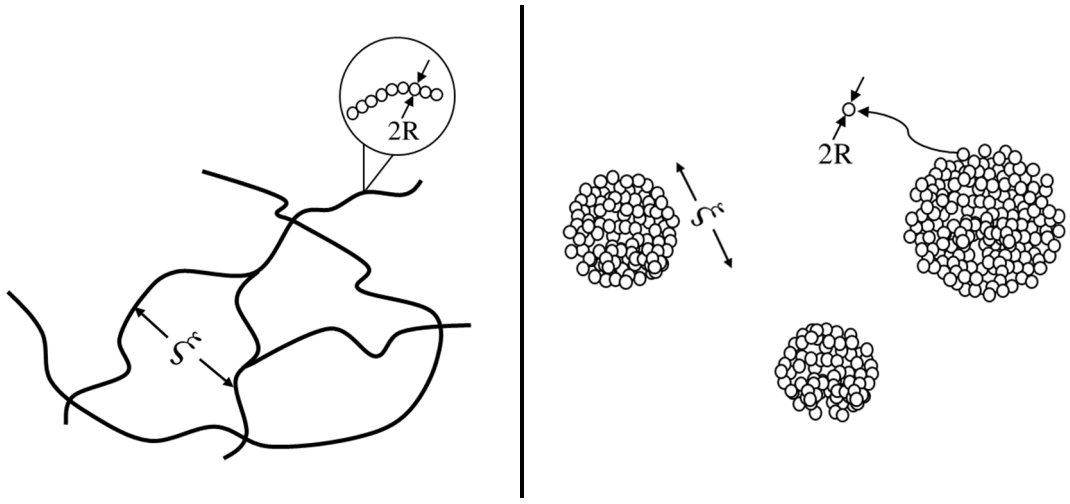

(a) (b)

Figure 10. Correlation length (ξ) representing (a) pore size within a solid mass fractal, based on [137], and (b) the size of an agglomerate.

4.3.2 Scattering intensity at large q

The scattering intensity at large q is independent of the shape of a scatterer, and it is mainly due to the surface scattering [135]. In this domain, $\langle F(q)^2 \rangle$ is given by the Porod law expressed in Eq. (18) as,

$$\left\langle F(q)^2 \right\rangle = \frac{2\pi \left(\rho - \rho_0\right)^2 S}{q^4} \tag{18}$$

where S is the total surface area. Porod law applies to the smooth surfaces, or in the presence of a sharp interface between two media (i.e., scatterer and solvent). Furthermore, according to Eq. (14), structure factor is equal to unity at large q. Porod law can be generalized to include the surface fractals. In this case, $\left\langle F(q)^2 \right\rangle$ can be expressed according to Eq. (19) as,

$$\left\langle F(q)^2 \right\rangle = \frac{\pi \left(\rho - \rho_0\right)^2 S \Gamma(5 - D_s) \sin\left[\pi (D_s - 1)/2\right]}{q^{(6 - D_s)}} \tag{19}$$

for $D_s = 2$, Eq. (19) simplifies to Eq. (18). Overall, at large q, $3 < \left(6 - D_s\right) < 4$ represents surface fractals, while $\left(6 - D_s\right) = 4$ is the indication of smooth surfaces [135].

4.3.2.1 Estimating the size of smallest structure in a system

The radius of smallest structure in a system can be achieved by calculating the initiation of the Porod region [136], according to Eq. (20), as

$$R_s = 1 \diagup q_{ip} \tag{20}$$

where R_s is the radius of smallest structure and q_{ip} the scattering vector at the initiation of Porod region. For instance, in the case of polymers, R_s represents the radius of a monomer. In this region and for smooth surfaces, $q^4 I(q)$ versus q exhibits an oscillating behavior, and the slope of the line between those variables is negligible.

4.4 Agglomeration Mechanism

The value of fractal dimension can provide information about the mechanism of agglomeration, which is generally divided into the two categories of particle-cluster and cluster-cluster agglomerations. For ASR, the fractal dimension provides information about the growth of agglomerates either by the integration of silicate monomers (as in particle-cluster agglomeration) or the combination of silicate monomers to form oligomers (also referred to as clusters), which in turn link to create agglomerates (as in cluster-cluster agglomeration). Furthermore, it can inform about the size distribution of clusters within an agglomerate. In the diffusion limited cluster agglomeration, clusters are monodisperse, while in the reaction limited cluster agglomeration, a polydisperse distribution of clusters is expected [138]. These mechanisms are explained below.

In the Diffusion Limited Aggregation (DLA) [139,140], which is a particle-cluster agglomeration mechanism, agglomerates grow by the integration of particles with “random walk” movement to form dense agglomerates. On the other hand, in the cluster-cluster agglomeration, clusters attach to each other via Diffusion Limited Cluster Aggregation (DLCA) or Reaction Limited Cluster Aggregation (RLCA) to form larger agglomerates. In DLCA, clusters are envisioned to attach to each other via permanent bonding, and the outer cluster acts as a constraint for the penetration of clusters beyond a certain length [141]. In contrast, in RLCA, clusters contact with each other many times before they form a bond, so they can penetrate further and form denser agglomerates than those formed through DLCA. Overall, the fractal dimensions of structures formed via DLA, DLCA, and RLCA are 2.5, 1.7, and 2.11 respectively [35,142].

In practice, the three values of fractal dimensions calculated based on DLA, RLCA, and DLCA are not enough to interpret experimental results, which may exhibit a continuous change of fractal dimensions. Kallala et al. [142] developed a model that allows for switching between types of growth regimes until the formation of final products. The first growth regime is associated with the pairing of monomers and the combination of linear polymers from their ends. However, as the population of linear polymer ends decreases, branched polymers form. Similar to fractal dimension obtained through DLCA mechanism, the fractal dimension of this regime is 1.7. In the second regime, the first regime is followed by linking branched polymers, which results in the fractal dimension of 2.1 similar to that of RLCA mechanism. In the third regime, when all polymers are combined and they are more reactive than monomers, the fractal dimension of agglomerates increases as monomers further densify the polymers. Depending on the relative reactivity of monomers and polymers, densified agglomerates may precipitate. Furthermore, the short-range attractive forces between monomers and binding sites facilitate the formation of dense agglomerates, while the short-range repulsive forces between those favors growth of branches [142].

For ASR samples, understanding the fractal dimension gives structural information about the mechanism of agglomeration, number density of clusters within agglomerates, and structural modification during aging and redistribution of silica [143].

4.5 Summary

This chapter provided the concepts and theoretical derivations in small angle scattering. This information is required for the further analysis of SANS results in chapter 5.

CHAPTER 5. THE ROLE OF COMPOSITION IN ALKALI-SILICA REACTION (ASR) SOL AND GEL

5.1 Overview

This chapter aims to address the first Objective of this dissertation: the role of composition in the structure of ASR sol and gel, and damage. While the majority of this chapter deals with SANS, the results of ^{1}H NMR relaxometry, and dynamic viscosity measurements, as well as the role of aging are also discussed.

5.2 Small Angle Neutron Scattering

SANS results of sols prepared at S/A of three, four and five are shown in Figure 11. For mixes prepared at S/A of zero, one, and two, the incoherent scattering intensity of hydrogen dominated the scattering curve. Thus, no significant differences between the scattering intensity of the blank sample and those samples were observed. Furthermore, for samples prepared at S/A of larger than five, percolated gel networks (Figure 12) or large precipitates were formed, which were too large to be fully characterized over the q range used in this study. For samples prepared at S/A of three, scattering curve indicates a nearly constant scattering intensity for a wide range of q. This behavior is attributed to the scattering from isolated structures. In contrast, in sols prepared at S/A of four and five, mass fractal agglomerates are formed, which show a fractal behavior in the range of $q<0.1$ (Figure 11). It should be noted that samples prepared at the S/A of three also show a slight fractal behavior at low qs ($q<0.015$). However, given the low level of scattering intensity and the small range of the fractal domain, it is challenging to reliably extract structural

information about those agglomerates. Furthermore, the presence of the Porod region at large *q*s, where $I(q) \sim q^{-4}$, indicates that the surface of small silicate structures is smooth, which is in agreement with previous studies on silica aerogels and aqueous silica gels [56,136,143–145].

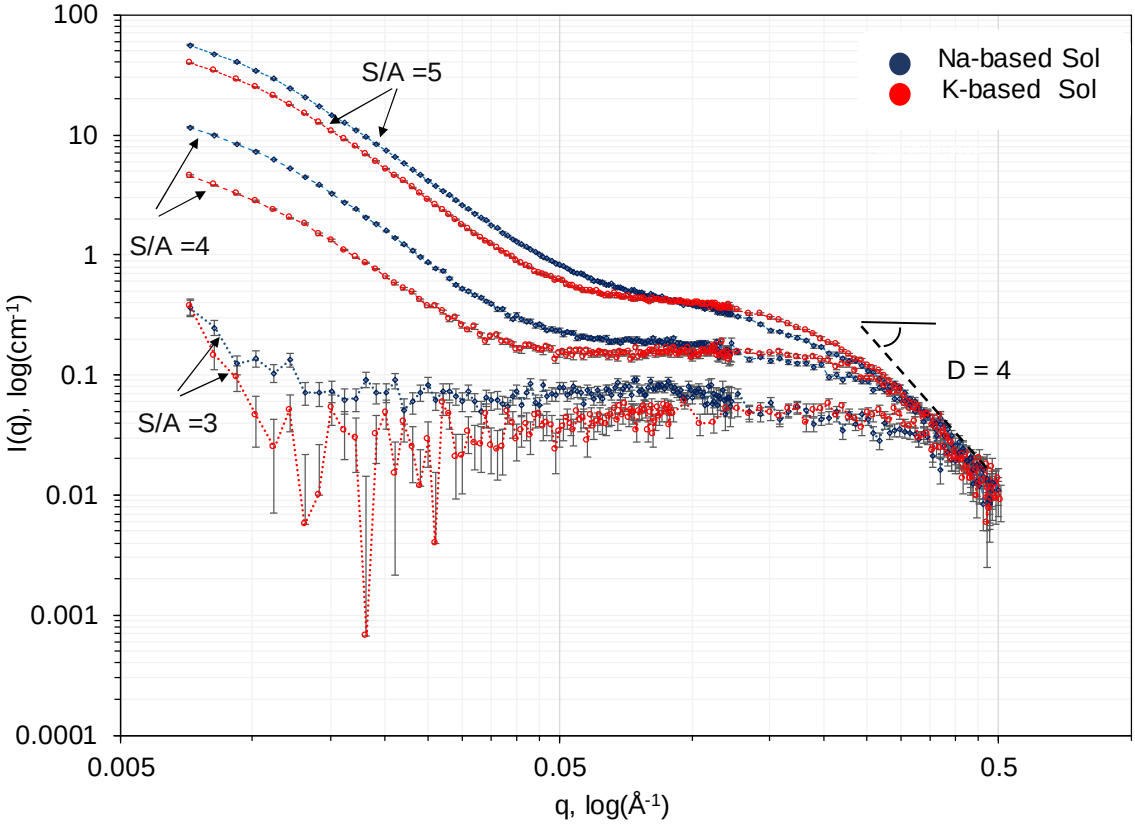

Figure 11. Scattering intensity, *I*(*q*), versus scattering vector, *q*, for Na- and K-based sols.

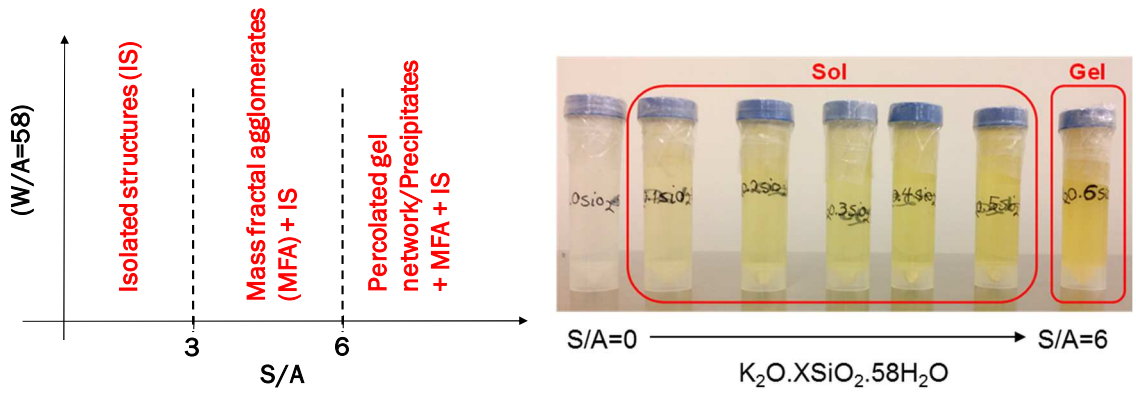

(a) (b)

Figure 12. (a) Structural evolution of ASR samples with increase in the silica-to-alkali molar mass ratio (S/A) and (b) K-based samples prepared at various S/A.

The radius of smallest structure in the alkali-silicate systems is determined by identifying the initiation of Porod region through $q^4I(q)$ versus q plots (Figure 13), and using Eq. (20). The radius grows from 2.5 Å to 3.3 Å as S/A increases from three to five, most likely as a result of growth and increased polydispersity of structures [146] and the decrease in the proportion of ionic silica [37]. The value of 2.5 Å is very close to the radius of the equivalent sphere of SiO_3^{2-} (2.37 Å) and $HSiO_3^-$ (2.44 Å) as expected (Figure 14). These ions are the prevalent ionic species in the concentrated Na- and K-based sols prepared at S/A of one and two [37]. At higher S/A, the excessive silica forms very small equiaxed or spheroidal internally condensed silicate polymer ions [37]. No significant difference between Na- and K-based sols is observed.

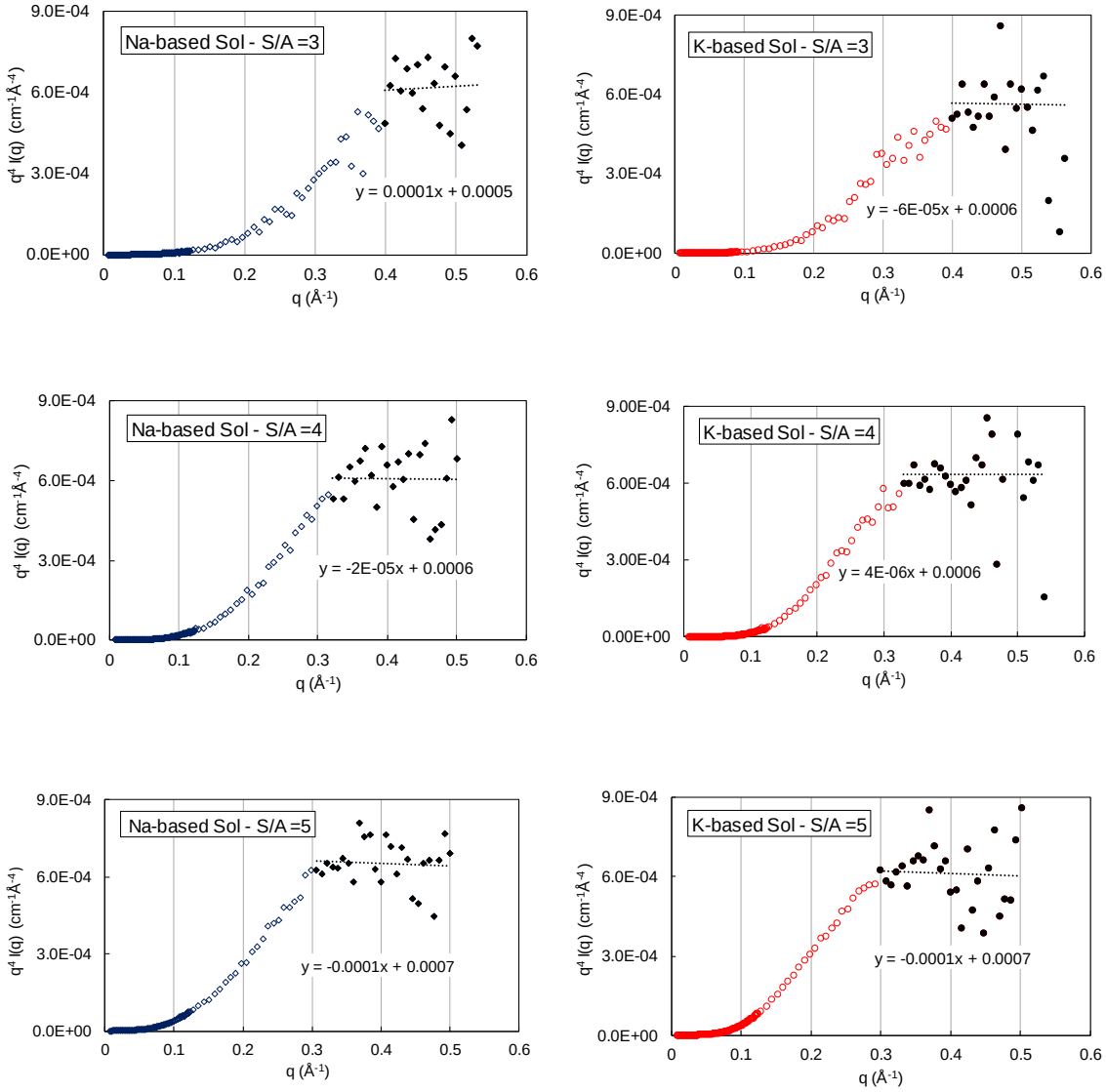

Figure 13. $q^4I(q)$ versus q for Na- and K- based sols.

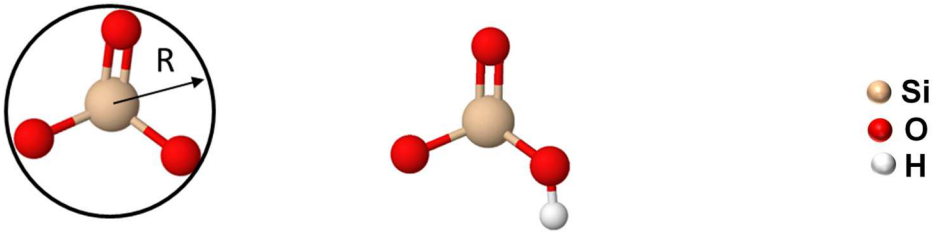

Figure 14. Molecular structure of SiO_3^{2-} and $HSiO_3^-$, and the radius of the equivalent sphere.

5.2.1 Extracting structural information by modeling

Given the diverse nature of silicate species, an appropriate model to provide structural information about the sols should consider the effect of polydispersity and type of structures (i.e., isolated structures versus agglomerates). Since isolated structures have an equiaxed (i.e., spherical) or spheroidal form [37], their scattering intensity can be expressed as the sum of scattering from the mixture of spheres [57] according to Eq. (21), as

$$I_{IS}(q) = K \times \sum_i C_i \times \left\langle F(q)^2 \right\rangle_i \times S(q)_i \tag{21}$$

where I_{IS} is the scattering intensity of isolated structures, K a constant, and C_i the number fraction of i^{th} specie present in sols. $\left\langle F(q)^2 \right\rangle_i$ and $S(q)_i$, which are the $\left\langle F(q)^2 \right\rangle$ and $S(q)$ of i^{th} specie, can be calculated according to Eqs. (13) and (15), respectively. In addition, $(\rho - \rho_0)$ in $\left\langle F(q)^2 \right\rangle_i$ is assumed constant and equal for all structures. Since K^+ and Na^+ exhibit comparable scattering length [55], similar scattering length densities are assumed for the Na- and K-based sols. Details of assumptions in using Eq. (21) can be found in [57].

For mass fractal agglomerates consist of spheres, scattering intensity can be calculated by combining Eqs. (11), (13), and (17), as shown in Eq. (22)

$$I_{MFA} = \langle N \rangle \left\{ {}^{4}\!/\!_{3}\,\pi R^3 (\rho - \rho_0) \left(3 \frac{\sin(qR) - qR\cos(qR)}{(qR)^3} \right) \right\}^2 \times \left(1 + \frac{1}{(qR)^D} \frac{D\Gamma(D-1)}{(1+\frac{1}{q^2\xi^2})^{\frac{(D-1)}{2}}} \sin\left[(D-1)\tan^{-1}(q\xi) \right] \right) \quad (22)$$

where I_{MFA} is the scattering intensity of mass fractal agglomerates, and R is set to 3 Å, slightly larger than the size of monomeric ionic species to include the contribution of larger isolated structures. Furthermore, in mixes prepared at S/A of four and five, the scattering intensity is due to the presence of both mass fractal agglomerates and isolated structures. If the spatial correlation between isolated structures and agglomerates is neglected, the scattering intensity can be expressed according to Eq. (23) [18] as,

$$I(q) = I_{MFA} + I_{IS} \quad (23)$$

To investigate the size and number fraction of isolated structures, Eq. (21) is fit to the experimental data up to the initiation of Porod region (since Porod's law is independent of geometry and topology of scatterers [147].) using a stepwise linear regression algorithm with Akaike information criterion (AIC) [148] for model selection to avoid overfitting. Based on the shape of scattering curves, an equal value of V/v_1 is considered for all isolated silicate species (Figure 15). Furthermore, the equivalent sphere radius of monomeric ions is selected as 2.5 Å and radiuses between 4-30 Å with an increment of 1 Å, are set as the model input. The size of structures may be slightly changed for a better fit. In addition, to evaluate the fractal dimension and correlation length of agglomerates, Eq. (22) is fit to the

experimental data using a least squares approach. The experimental data and fitted model (Eq. (23)) are shifted vertically for better illustrations (Figure 16), and modeling results are shown in Tables 5 and 6.

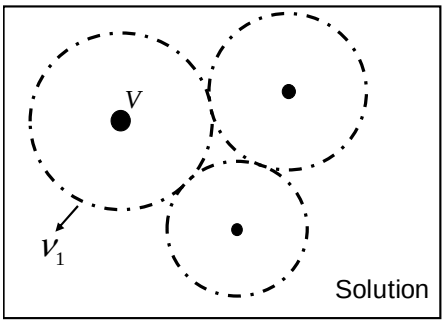

Figure 15. Scatterer volume (V) and average sample volume per scatterer (V_1)

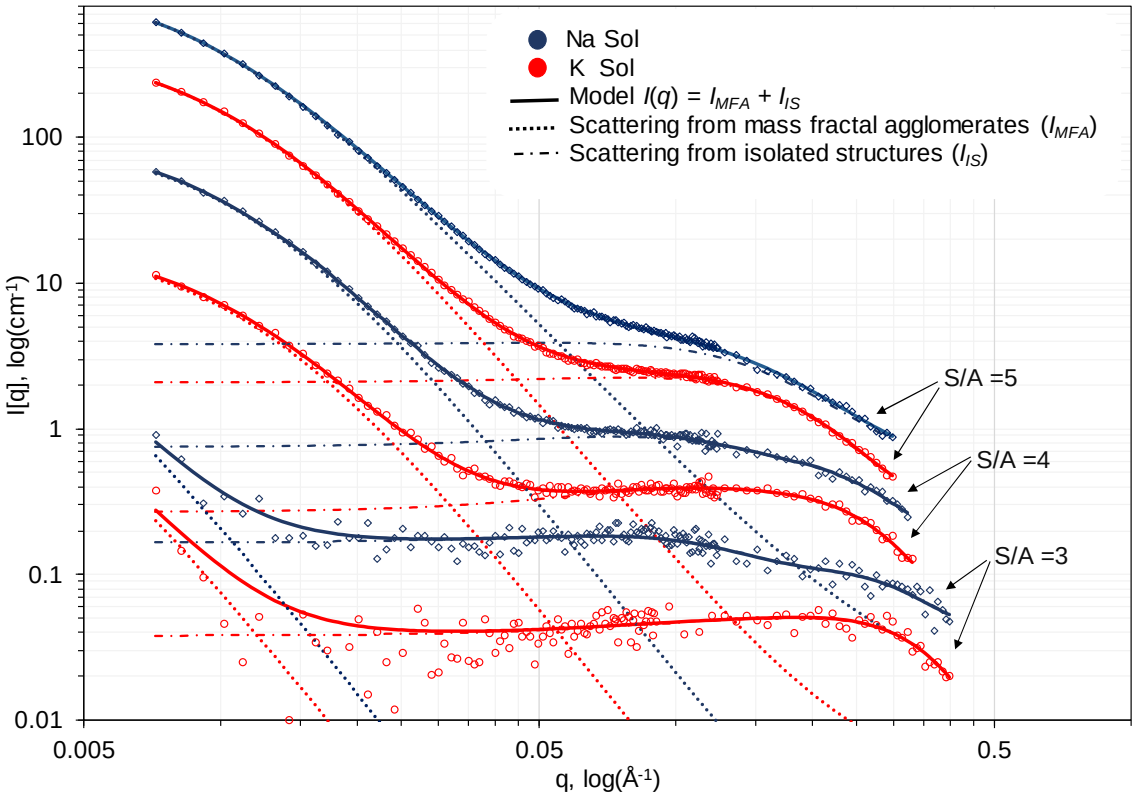

Figure 16. Experimental data and fitted model of small-angle neutron scattering measurements (data and fitted model are moved vertically for better illustrations).

Table 5. Modeling results for isolated structures present in sols: radius, number fraction, and the volume ratio of scatterer to the average sample volume per scatterer (V/v_1) (excluding the contribution of agglomerates).

	Na-based Sol			**K-based Sol**		
			S/A =3			
Radius (Å)	2.5	8	20	2.5	7	19
Number Fraction (%)	99.822	0.177	0.0008	95.757	4.241	0.0011
V/v1		1/14			1/12	
			S/A =4			
Radius (Å)	2.5	10	21	2.5	9.5	19
Number Fraction (%)	99.942	0.057	0.0004	99.842	0.158	0.0005
V/v1		1/13			1/11	
			S/A =5			
Radius (Å)	2.5	11	18	2.5	11	16
Number Fraction (%)	99.961	0.037	0.0019	99.946	0.050	0.0037
V/v1		1/19			1/16	

Table 6. Modeling results for agglomerates present in sols: correlation length, fractal dimension, and the relative number* of agglomerated species**.

	S/A= 4		**S/A= 5**	
	Na-based Sol	**K-based Sol**	**Na-based Sol**	**K-based Sol**
Correlation length of agglomerates (ξ)	84.4 Å	84.4 Å	100 Å	89 Å
Fractal dimension (D)	3.0	3.0	2.77	2.93

	S/A= 5 to 4		Na- to K-based Sol	
	Na-based Sol	**K-based Sol**	**S/A= 5**	**S/A= 4**
Relative number of agglomerated species	9.54	11.1	2.64	2.27

* Assuming comparable scattering length density for Na- and K-based sols and similar size distribution of silicate species within agglomerates.

** For Na- and K-based sols prepared at the S/A of three, ξ=300 Å, and D =3.0 was used for modeling. However, given the small number of data points present in the fractal domain, these values may not be exact. Overall, these samples are mainly made of isolated structures, and the contribution of such agglomerates in the sol behavior is minimal, as evidenced by their very low scattering intensity.

The analysis of isolated structures indicates the domination of monomeric silicate ions over other species. Since the size of silicate monomer, 2.82 Å, is close to that of monomeric ionic species, the number fraction of R=2.5 Å most likely represents all monomeric species including $HSiO_3^-$, $SiO3^{2-}$, and $Si(OH)_4$. In addition, prior to the initiation of Porod region, the tails of scattering curves are distinct for Na- and K-based sols (Figure 16). Compared to K-based sols, the decrease in scattering intensity occurs at smaller *q*s for the Na-based sols (i.e., Figure 16, S/A = 3) indicating the contribution of larger isolated structures (Table 5). Considering the intermediate *q*s (around 0.05), where the deviation from fractal behavior occurs due to the presence of isolated structures, a sharper deviation is observed for the K-based sols (Figure 11 and Figure 16). This behavior reflects in the larger V/v_1 (Table 5), which suppresses the value of scattering intensity in the range of low and intermediate *q*s, and indicates the larger extent of interaction among structures [135] in K-based sols than Na-based ones. To illustrate the effect of V/v_1 on the

scattering curve, $I(q)$ versus q for spheres with the radius of 10 Å when V/v_1 is equal to 1/11 and 1/13 (as in K- and Na- based sols at S/A = 4) is plotted (Figure 17).

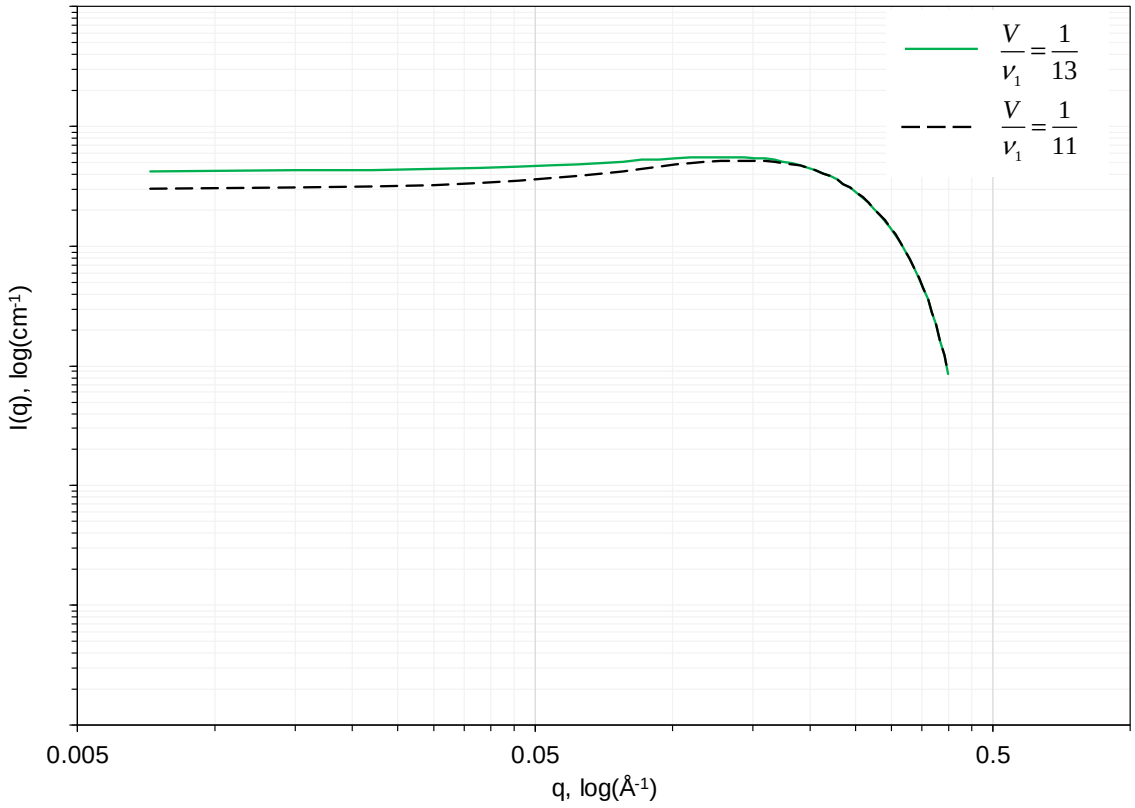

Figure 17. Scattering intensity versus scattering vector for R = 10 Å spheres with different values of V/v_1.

The large values of mass fractal dimensions indicate the formation of densified agglomerates. Determination of mechanism of agglomeration requires evaluating fractal dimension soon after sample preparation. Most likely, agglomerates are formed through DLCA [149], followed by further densification by the addition of isolated structures in the solution, similar to the agglomeration mechanism in alkali-silicate sols when calcium is added [35]. The fractal dimension of three for both Na- and K-based sols prepared at the S/A of four is attributed to the small number of agglomerates and presence of excessive

silicate species for densification. However, as S/A increases from four to five, the number of agglomerated species may increase approximately by an order of magnitude (Table 6), while based on the modeling results, the number of monomers increases around 75% in the K-based sol and 20% in the Na-based ones (comparing other isolated structures is not feasible due to the differences in size). This result suggests the formation of agglomerates at the expense of decreasing isolated structures in the sol. Thus, less isolated structures are available for the densification of agglomerates and their fractal dimension decreases. This effect is more pronounced in the Na-based sol, where more agglomeration occurred. A similar interpretation has been used to explain the decrease in the fractal dimension of agglomerates with an increase of the calcium content of alkali-silicate sols [35]. Therefore, as S/A increases from four to five, the correlation length of agglomerates in the Na-based sol grows from 84.4 to 100 Å, while the correlation length of those in the K-based sol increases from 84.4 to 89 Å, but they are denser than the agglomerates present in the Na-based sol.

SANS results agree with the theory of alkali-silicate mixes, which indicates an increment in the polymerization of silicate structures with an increase in S/A. According to theory, concentrated Na- and K-based sols prepared at the S/A of one and two contain mainly monomeric silicate anions ($HSiO_3^-$, $SiO3^{2-}$). However, at higher S/A, a small portion of different cyclic oligomers can form polycyclic oligomers; i.e., cyclic tetramer anions form cubic octamer anions (Figure 18), which act as the starting point for the formation structures with R around 5 Å, and further condensed to create very small three-dimensional equiaxed or spheroidal ionic structures. The interior part of these structures is made of Si-O-Si bonds to form a core of SiO_2, while on the exterior part, the silicon atoms

are connected to at least one hydroxyl group. The surface of these structures contains negative charge due to the partial ionization of hydroxyl groups [37] as described in Eq. (24).

$$\equiv Si-OH+OH \rightarrow \equiv Si-O^{-}+H_2O \tag{24}$$

These structures are in solubility equilibrium with silicate monomers, which are in equilibrium with monomeric silicate ions. Such structures further act as nuclei for larger colloidal species as S/A increases [37].

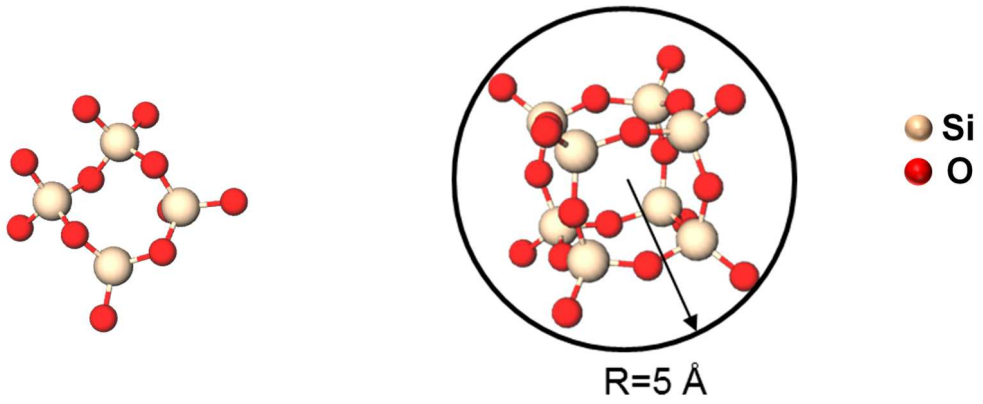

(a) (b)

Figure 18. (a) Cyclic tetramer anion $(Si_4O_{12})^{8-}$ and (b) cubic octamer anion $(Si_8O_{20})^{8-}$ or double-four ring.

In an alkaline environment and in the presence of cations, isolated structures can further grow through condensation of Si-OH to form Si-O-Si bonds in only a few minutes, and form agglomerates. The agglomeration is more pronounced as cations with concentrations equal or higher than the critical coagulation concentration (c.c.c), which is the limit between slow and fast coagulation regimes (i.e., 0.3 N), screen the negative charge of silicate structures and bring them together [37]. Later, the silicate structures decrease in

number and increase in size as smaller structures dissolve and deposit on larger ones through an Ostwald ripening process. The solubility of structures is more pronounced when their average size is lower than 30 Å, while the particles between 50-100 Å grow at a slow rate [37]. As mentioned before, SANS measurements were performed about 24 hours after mixing, which allows sufficient time for redistribution of silica. Ripening effect may have contributed to the high fractal dimension of agglomerates with the correlation length of 84.4 to 100 Å and low number fraction of small colloidal species in the sols.

5.2.1.1 Coagulation of silicate structures

Coagulation can occur through (a) attraction of silicate structures by van der Waals forces unless the hydration barrier or electrostatic repulsion of structures overcomes it and (b) cations as they bridge between silicate structures [37]. In the case of van der Waals forces, silicate structures can agglomerate as cations hold them at the points of contact [37]. For instance, in a hydrated kanemite crystal, the attraction force between silicate sheets is the hydrogen bonding between oxygen in the silicate layer and hydrogen of water molecules coordinated with sodium [34]. However, in the hydrated silicate structures of smaller than 250 Å, a monolayer of water is enough to overcome the van der Waals forces; these forces may be only effective when the size of structures are larger than 1000 Å [37]. Structures in sols are partially covered with OH, which creates hydrogen bonding with water molecules to form a hydration layer. Since coagulation requires the disturbance of the hydration layer, Allen and Matijevic [150] suggested that silicate structures coagulate as alkali cations exchange with the hydrogen of a hydroxyl group (Eq. (25)), and concluded that the nature of the alkali cation determines pH and the concentration of the electrolyte

at which ion exchange starts. Between pH 10 and 11.5, the c.c.c is lower for Na compared to K-based electrolyte [150].

$$\equiv Si - OH + A^{n+} \rightleftharpoons \equiv Si - OA^{(n-1)+} + H^{+} \quad (25)$$

where A^{n+} is the cation with charge n^{+}.

Other studies indicate the ability of alkali cations to coagulate silicate structures between pH 7-11, with lower coagulation concentration for Na compared to K-based salts. However, above pH 11, only smaller cations, Li^{+} and Na^{+}, coagulate silica, while larger cations such as K^{+}, Rb^{+}, Cs^{+} are not effective [151]. To explain this behavior, Iler [37] proposed that the monovalent cations bridge between silicate structures. In this process, a hydrated cation (Na^{+} in Figure 19) is adsorbed on the ionized surface of silica to neutralize surface charge. During adsorption, oxygen atom(s) of the hydrated cation can replace the oxygens in the silanol group, thus creating a direct link with silicate surface (Figure 19b). The remaining water molecules can be further replaced with silanol groups of a second silicate structure to bridge between them. However, above pH 11, the surface of silicate structures is covered with basic groups. Larger cations at high concentration presumably cover the surface and create a double layer of sufficient thickness, which hinders coagulation.

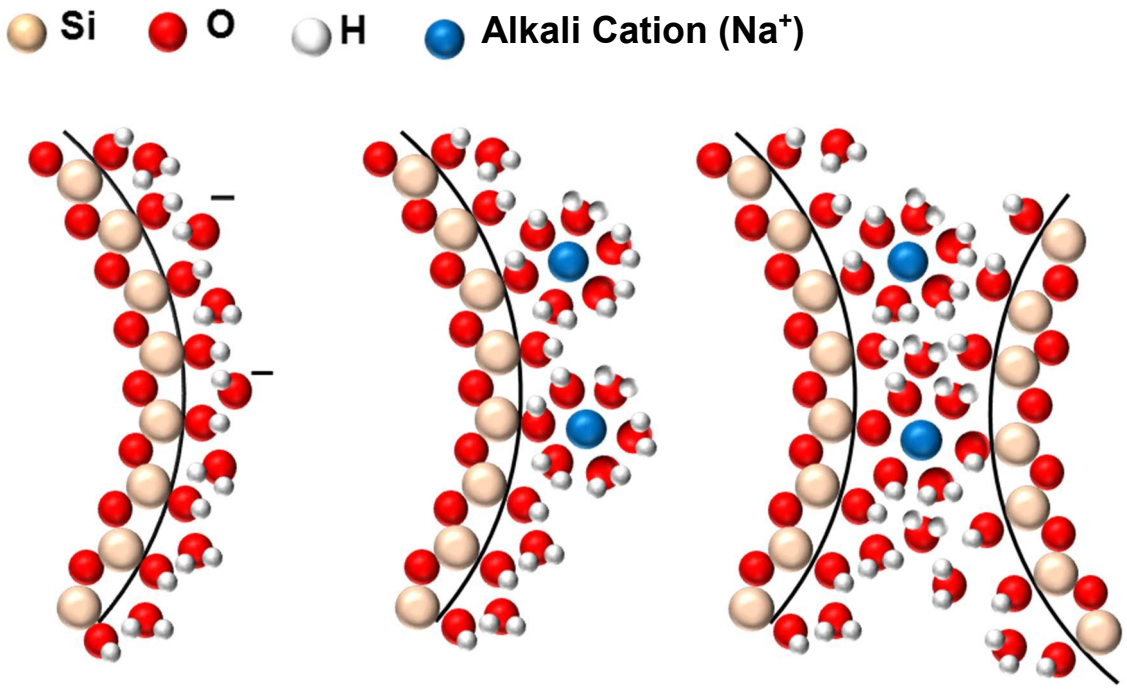

(a) (b) (c)

Figure 19. Agglomeration of silicate structures through alkali cation (Na^+) bridging. (a) Partial ionization of hydration layer, (b) absorption of alkali cation on silicate structures, and (c) attachment to the uncharged area of the second structure (based on [37]).

5.2.1.2 The effect of alkali cation on the agglomeration of silicate structures

While no general agreement about the mechanism of stability and coagulation of silicate hydrosols exists [152,153], several studies have shown the presence of short-range (< 100 Å) repulsive forces at high ionic concentrations [154]. These forces most likely originate from the overlap of the hydration layer of silicate structures and the steric effect from the hairy (poly)silicic acid stretched from silicate structures [155]. Although hydration forces are present in the dispersion of silica in deionized water, their strength and range are reduced in the presence of electrolyte as cations disturb the hydration layer. The reduction is more pronounced for strongly hydrated cation, $Li^+ > Na^+ > K^+ > Cs^+$ [156].

Similarly, it has been shown that the extent of short-range repulsive forces correlates with the size of bare (unhydrated) alkali cation [157]. Another factor that affects the coagulation behavior of silicate hydrosols is the surface charge density of silica, which is the sum of negative and positive charges due to the adsorption of OH and alkali cations per surface area, respectively. The surface charge density of silica increases with the size of cation (at high pH), $Cs^+ > K^+ > Na^+ > Li^+$ [158,159], and does not reach a saturation level at high ionic concentration [158]. Therefore, based on the SANS results, the higher tendency for agglomeration and the lower V/v_1 of Na-based sols, which indicates less interaction among silicate structures, can be attributed to a reduced surface charge density and a lower extent of repulsive forces as compared to K-based sols. A similar phenomenon may be responsible for the increase in the agglomeration behavior of silicate gels (as measured by the scattering intensity at low *q*s) prepared at pH= 7-8 with a decrease in the size of alkali cation [56]. Overall, K-based sols can likely cause less extent of damage than Na-based sols due to their lower tendency toward agglomeration. They may pass through concrete porosities without causing damage.

5.3 Percolated Gel Network and Aging

With an increase of the silicate content of sols, their pH decreases. For instance, while the pH value of sodium and potassium solutions, at the S/A of zero, is higher than 13, it drops to 10.6 and 10.9 for Na- and K-based gels prepared at the S/A of six, respectively, and it also favors further agglomeration in the sols.

As the volume fraction of agglomerates reaches 0.5, they can close pack randomly to form a percolated gel network [37]. Afterwards, the network becomes stronger due to

the thickening of silica at the joints between agglomerates. Silica dissolves at convex surfaces due to the higher solubility and deposits at the concave surfaces, where solubility is lower (Figure 20). Furthermore, larger structures grow at the expense of the dissolution of smaller structures. These structural modifications can result in the collapse of the gel structure and phase separation.

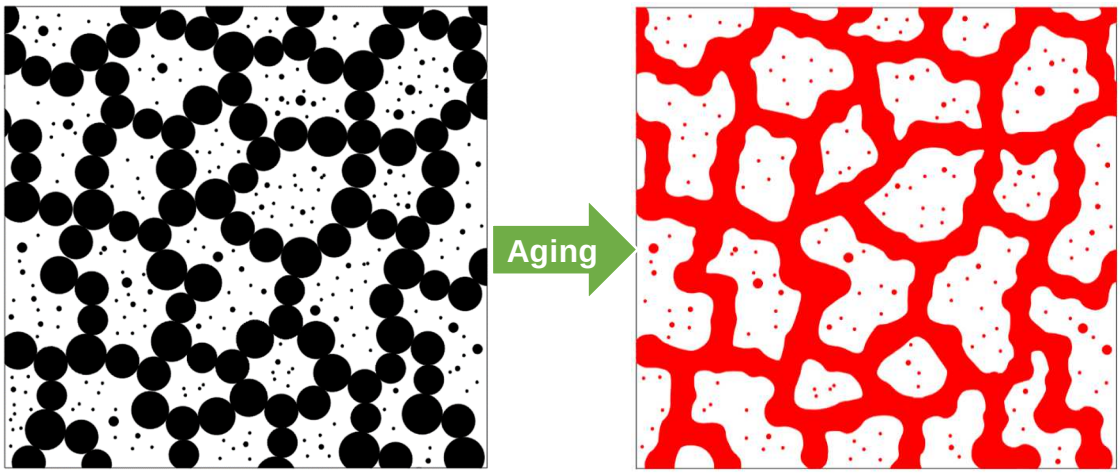

Figure 20. Structural modification of silica gel during aging (growth of structures is neglected, based on [37]).

The change in the appearance of silicate mixes can provide information about the size of growing silicate structures during aging. For instance, sols with silica content higher than 10-15% and structures smaller than 70 Å are transparent, between 100 and 300 Å they appear translucent, and when structures are larger than 500 Å they look milky and white (Figure 21). If the structures are larger than 1000 Å, they settle and release a transparent solution on the top layer [37]. The effect of aging was observed for gels/precipitates prepared at $S/A \geq 6$. In contrast to K-based gels, an alkaline solution leached from the Na-based gels/precipitates after few weeks from preparation. Furthermore, while both Na- and K-based gels prepared at the S/A of six looked similar after preparation (Figure 12b), they

developed a white color during aging, with a clear phase separation for Na-based gel (Figure 22). This observation indicates the presence of larger structures in the Na-based gel, which can be partially attributed to the less repulsion between silicate structures. Since the growth of structures occurs by deposition of smaller silicate structures on larger ones, the less repulsion can result in denser and larger structures during aging. Other factors, such as higher fluctuation in the number of non-bridging oxygen per silica atom in the Na-based gels versus K-based ones could have contributed to the phase separation in Na-based gels [39]. Overall, these results are consistent with the increase in phase separation as the size of alkali cation decreases [160]. The release of alkaline solution due to phase separation of ASR gels can provide alkali ions for further reaction and degradation of cement-based materials.

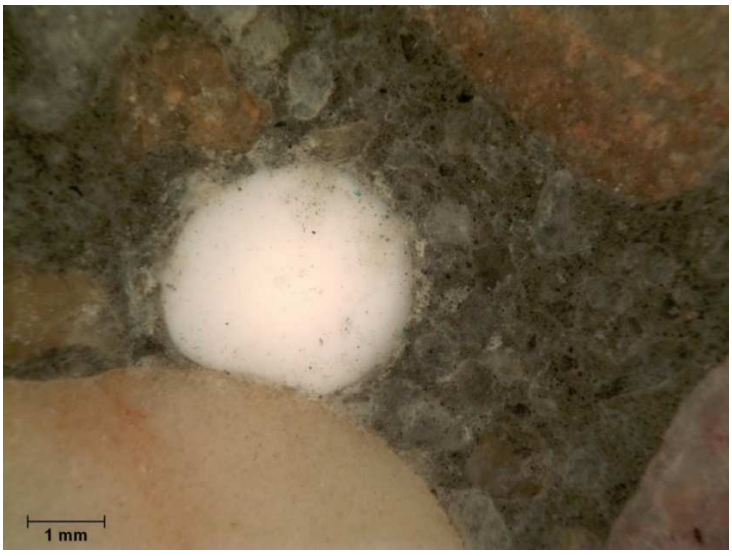

Figure 21. ASR gel in the freshly cut section of a concrete prism exposed to ASTM C1293 condition for more than one year.

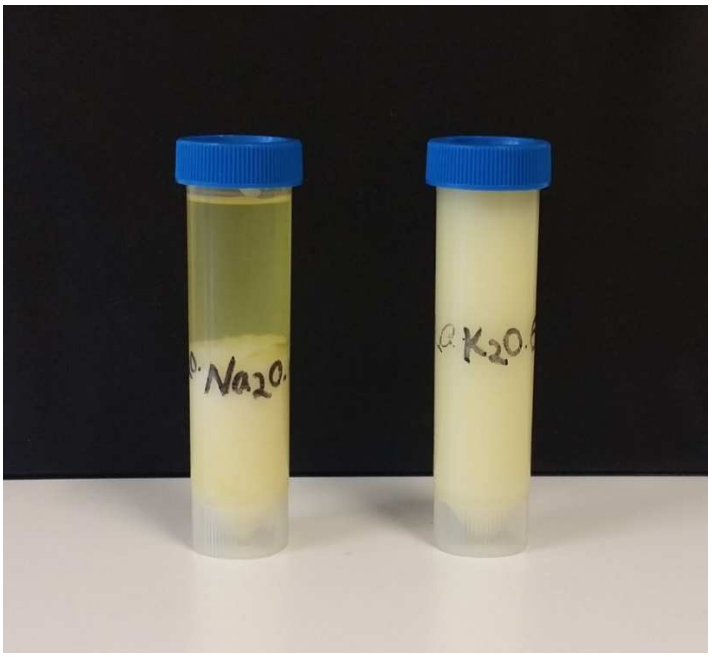

Figure 22. Na and K-based gels prepared at the S/A of six, after two years of aging at 23±1.5 °C.

5.4 ^{1}H NMR Relaxometry

The spin-spin relaxation time (T_2) results show a good fitting between a single exponential decay function and the magnetic decay of each sample, indicating a fast exchange of free and bound water in the timescale of the experiment [161]. In a fast exchange regime, since water molecules experience both bound and free states, the measured spin-spin relaxation rate ($1/T_2^*$) is the weighting average of those of bound and free water, which can be expressed according to Eq. (26) [162], as

$$\frac{1}{T_2^*} = \frac{W_1}{T_{2\,(\text{free water})}} + \frac{(1-W_1)}{T_{2\,(\text{bound water})}}, \quad \left(T_{2\,(\text{free water})} > T_{2\,(\text{bound water})}\right) \tag{26}$$

where W_1 is the fraction of free water. A larger $1/T_2^*$ indicates a higher fraction of bound water and/or more strongly bonded water in the samples. In the porous media, if the T_2 of

absorbed water on the pore surface is significantly shorter than T_2 of bulk water, as in cement-based materials, then $1/T_2^*$ is approximately proportional to the inverse of characteristic pore size [161]. Similarly, $1/T_2^*$ can be used for comparing the overall porosity in the Na- and K-based gels.

For similar S/A ≤ 6, $1/T_2^*$ shows larger values for Na-based samples than K-based ones (Figure 23). However, as S/A increases, $1/T_2^*$ of K-based gels are higher. At the S/A of zero, a larger $1/T_2^*$ indicates that water is more tightly bound in the hydration layer of the sodium cation, as expected. At higher S/A ratios, the linear increase of $1/T_2^*$ up to the S/A of 3—with a larger slope for Na-based sols—is consistent with the increase of the silica content of sols, which provides a larger surface area for water binding. As agglomerates form at the S/A of four and five, the deviation of $1/T_2^*$ increment from the linear trend is more significant for Na-based sols, which exhibit a greater extent of agglomeration. The overall agglomeration in the sols (measured by the scattering intensity of mass fractal agglomerates (I_{MFA}) at low qs) is proportional to the increased in the water-binding ability of sols in the presence of agglomerates (measured by the deviation from the linear trend between $1/T_2^*$ and S/A (i.e., B or C in Figure 23)), presumably as water is further bound in the structure of agglomerates (i.e., Figure 19c) (Table 7).

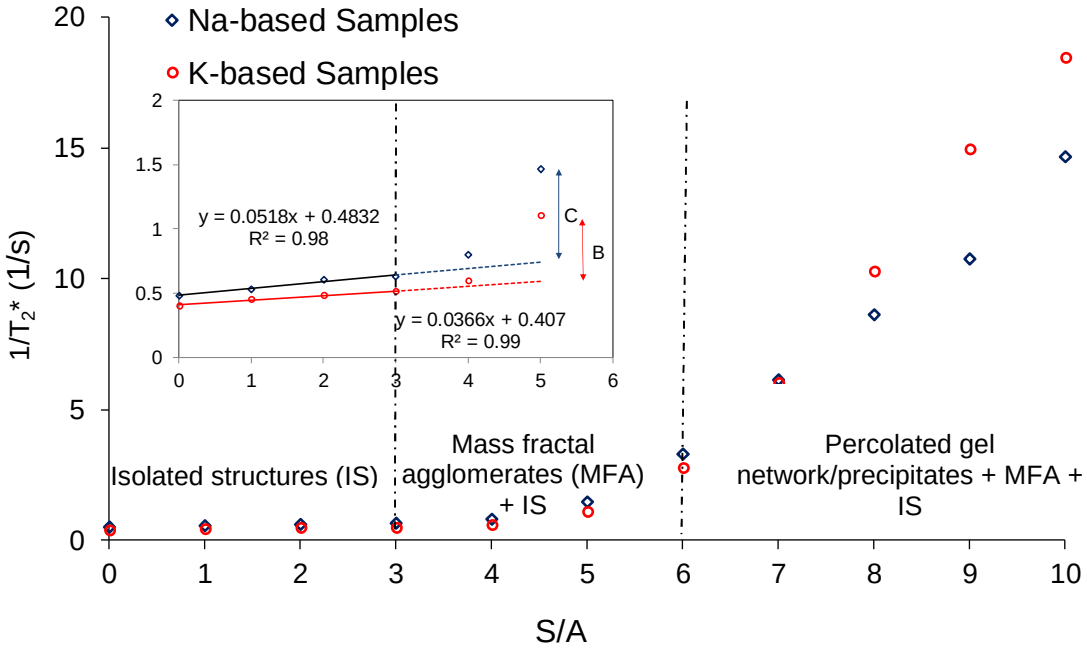

Figure 23. Spin-spin relaxation rate ($1/T_2^*$) versus silica-to-alkali molar ratio (S/A) for Na- and K-based samples.

Table 7. Extent of agglomeration in sols and the increase in their water-binding ability in the presence of agglomerates.

	S/A= 5 to 4		**Na- to K-based sol**	
	Na-based Sol	**K-based Sol**	**S/A= 5**	**S/A= 4**
Ratio of I_{MFA} ($q=10^{-5}$)	5.37	9.39	1.51	2.64
Ratio of deviation from linear trend	6.79	11.17	1.39	2.27

At S/A ≥ 6, the slope of $1/T_2^*$ versus S/A is larger for K-based gels than Na-based ones, and K-based gels show larger $1/T_2^*$ than Na-based ones for S/A ≥ 7. This observation can be attributed to the better dispersion and particle packing of silicate structures in the

K-based gels due to the larger repulsive forces, and the formation of finer porosities. A similar phenomenon could be responsible for the finer porosities of geopolymers when KOH is used as an activation solution compared to NaOH [163], and the more disordered structure of K-based ASR gels [31]. Overall, $1/T_2^*$ shows a linear relationship with an increase in S/A when the system is dominated by isolated structures or percolated gel network, and a nonlinear increase of $1/T_2^*$ when the dominating mechanism is the formation of mass fractal agglomerates.

5.5 Dynamic Viscosity

The higher dynamic viscosities of Na-based sols (Figure 24) are consistent with ref. [64]. Furthermore, for S/A ≤ 3, silicate species behave similarly to spherical particles [58] according to the Einstein relation as,

$$\eta_{sp}/\mathrm{C} = K/\rho \tag{27}$$

where η_{sp} is the specific viscosity, C the concentration of a specie, K a constant, and ρ the density of a specie.

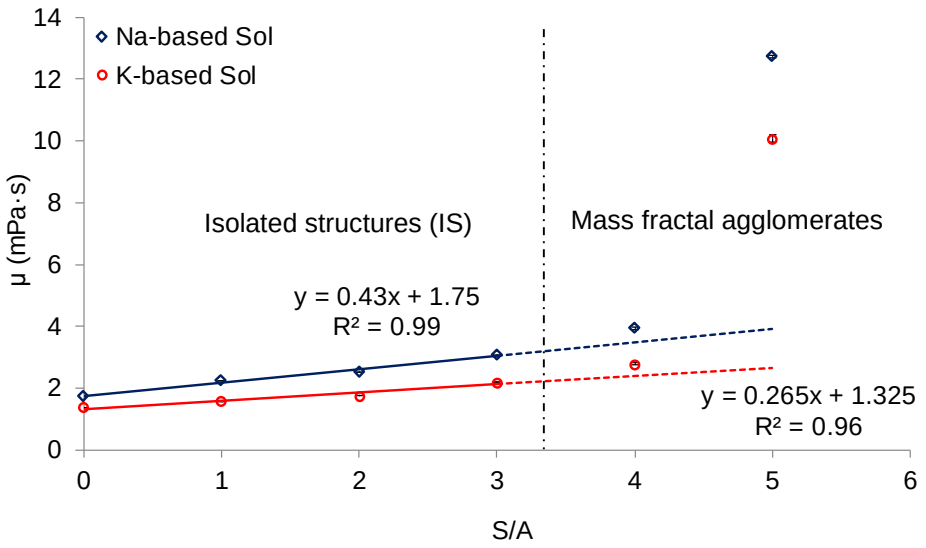

Figure 24. Dynamic viscosity versus silica-to-alkali molar ratio (S/A) of Na- and K-based sols.

Similar to spin-spin relaxation rate measurements, as agglomeration occurs at the S/A of four, a slight deviation from Eq. (27) occurs due to the low volume fraction of agglomerates. However, at the S/A of five, the significant increase in viscosity is attributed to the growth of agglomerates, and a substantial increase in the number of agglomerated species (Table 6). The lower viscosity of K-based sols compared to Na-based ones is attributed to larger repulsive forces among silicate structures, a lower number of agglomerated species, and loosely bound water in the hydration shell of potassium compared to the sodium cation.

5.6 Summary

Results from SANS, ^{1}H NMR relaxometry, and viscosity measurements indicate the significant role of the silicate content and the type of cation (Na^{+} versus K^{+}) in the structure, water-binding ability, and viscosity of ASR samples. SANS results show the

growth of nanoscale silicate structures with an increase in the silica-to alkali molar ratio (S/A). Sols prepared at the S/A of three are mainly composed of monomeric silicate species and a minor fraction of small silicate structures ($R \leq 20$ Å), which are slightly larger in the Na-based sols. At the S/A of four, densified mass fractal agglomerates with the correlation length of 84.4 Å are formed. Given the similarity of the fractal dimension of agglomerates, the type of cation does not seem to affect the mechanism of agglomeration, which most likely occurs through diffusion-limited cluster aggregation (DLCA) and further densification by isolated silicate species. However, the higher scattering intensity (at low *q*s) of Na-based sols reflects a higher level of agglomeration compared to K-based sols. This phenomenon may be attributed to the lower extent of short-range repulsive forces and reduced surface charge density of silicate structures in Na-based sols. SANS results also indicate the lower extent of interaction among structures in Na-based sols. At the S/A of five, the correlation length of agglomerates increases up to 100 Å, and the number fraction of agglomerated species may rise an order of magnitude compared to the sols prepared at the S/A of four. However, agglomerates develop porosity, which is higher in Na-based sols. This could be due to the shortage of isolated structures to densify agglomerates. Overall, K-based sols can likely cause less extent of damage than Na-based sols due to their lower tendency toward agglomeration. They may pass through concrete porosities without causing damage.

While spin-spin relaxation rate ($1/T_2^*$) of protons and dynamic viscosity measurements show a linear relationship for $S/A \leq 3$ (with higher values for Na-based sols), the water binding ability of sols clearly increases in the presence of agglomerates, presumably as water is increasingly bound in the structure of agglomerates. The increase

in the water-binding ability is more significant for Na-based sols, and it is proportional to the overall agglomeration in the alkali-silicate systems. At the S/A of six, as a percolated gel network forms, a significant increase in the water-binding ability of gels is observed. At higher S/A, the larger $1/T_2^*$ for K-based gels indicates their superior ability in binding water than Na-based ones, which can be attributed to the better particle packing and creation of finer porosities due to the larger extent of repulsive forces and surface charge density of silicate structures. A similar phenomenon could be responsible for the finer porosities of K-based geopolymers and more disordered structure of K-based ASR gels. Repulsion among silicate structures also contributes to their stability during aging. Na-based gels show a higher tendency toward phase separation.

Although the composition and behavior of ASR gel in the cement-based materials can be more complex due to the differences in the pH and concentration of alkali cations, and the presence of other cations such as calcium, the general trend in the behavior of sol and gel most likely follows the same trend. Similar to the sols prepared at low S/A, at the early stages of reaction ASR products have low viscosity and low water-binding ability. Thus, they are not expansive. However, as the reaction progresses, due to the further polymerization of silica, as in the sols prepared at S/A =4 and 5, their viscosity, water-binding ability, and potentially expansivity increases.

The knowledge developed in this chapter will help in the better understanding of the nonlinear acoustic results, which represent the coupled effect of microcracks and ASR products, in the next chapter.

CHAPTER 6. RELATIONSHIP BETWEEN EXPANSION AND DAMAGE IN THE ASR-AFFECTED MORTARS

6.1 Overview

This chapter aims to address the second Objective of this dissertation: the relationship between expansion and damage in the ASR-affected mortars. For this purpose, along with expansion, the ASR-induced damage in mortar bars is measured by the hysteresis acoustic nonlinearity, and damage-rating index (DRI) obtained from petrographic analysis. Results show a correlation between the expansion and DRI results. Also, a hypothesis is presented to interpret the temporal acoustic nonlinearity of ASR-affected samples.

6.2 Expansion Measurements

By ASTM C1260 [48], both Reactive-1 and Reactive-2 aggregates are deemed potentially deleterious, and the Non-Reactive aggregate as innocuous (Figure 25). Reactive-1 samples show the largest expansion, nearly 0.4%, at the end of the test period. Moreover, the expansion rate of those samples is almost constant from day three to day fourteen, which suggests the high availability of reactive silica. In contrast to the Reactive-1 samples, the expansion of the Reactive-2 samples starts at the day one of AMBT and exceeds the expansion of the Reactive-1 samples between day two and day nine. However, the rate of expansion observed for the Reactive-2 samples decreases from day seven, which suggests a decrease in the availability of reactive silica. In contrast to reactive samples, the expansion of Non-Reactive samples starts at day two of AMBT. By day five, the Non-

Reactive samples experience half of their fourteen-day expansion. Afterwards, samples expand at a low rate and their expansion reaches a plateau at day twelve.

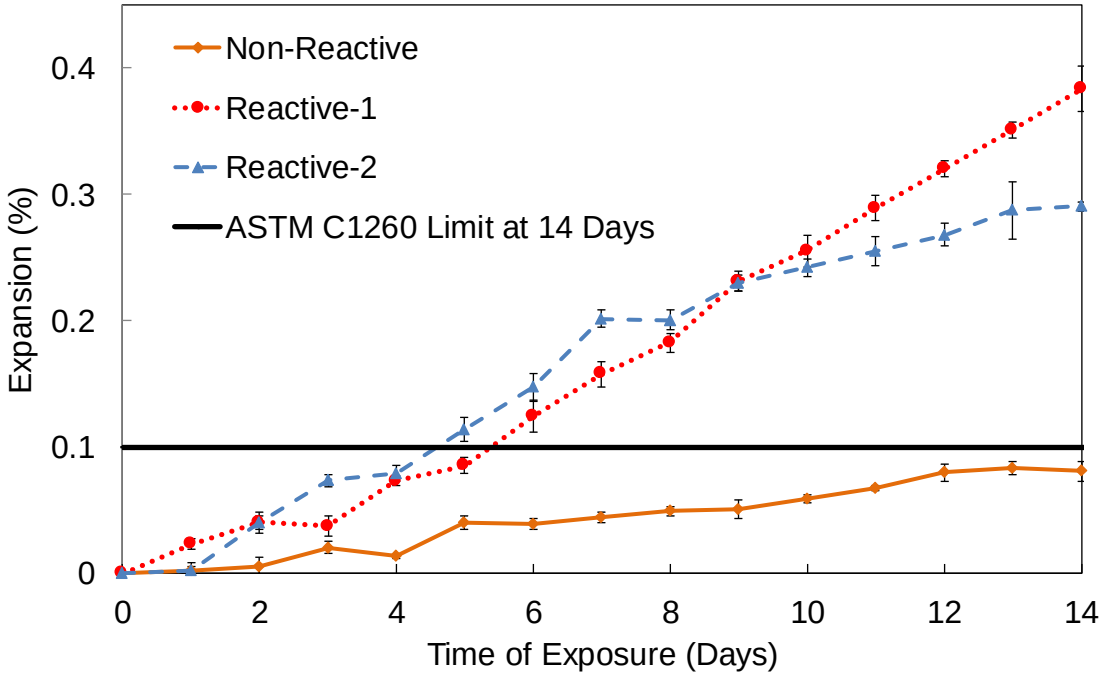

Figure 25. AMBT expansion results.

6.3 Petrography Analysis

Representative fluorescence microscopy images of each of the three mortar types after fourteen days of exposure are shown in Figure 26, while Figure 27 shows representative images of epoxy impregnated mortar samples at the same age. The fluorescence images show cracking around and through the aggregates and also in the paste for the potentially reactive samples; there is also a greater concentration of fluorescence, likely due to the presence of gel, around the aggregates and in some of the cracks. In addition, the fluorescence of some of the aggregates even without cracking is potentially

caused by the high pH of the NaOH soaking solution, which facilitates the ion exchange of sodium and uranyl at the silica surface [133].

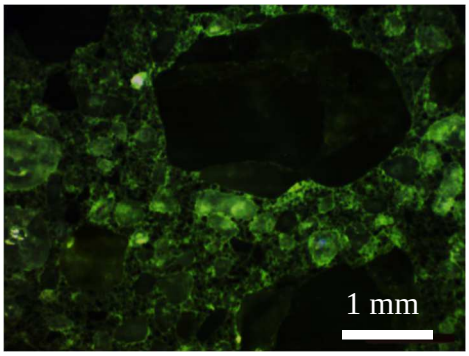

(a)

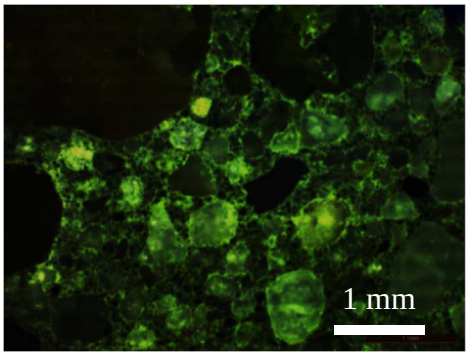

(b)

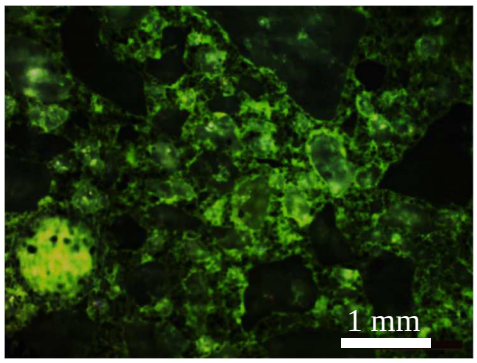

(C)

Figure 26. Fluorescence of gel in (a) Reactive-1, (b) Reactive-2, and (c) Non-Reactive samples, which were exposed to the AMBT condition for fourteen days (Mr. Knapp performed the microscopy).

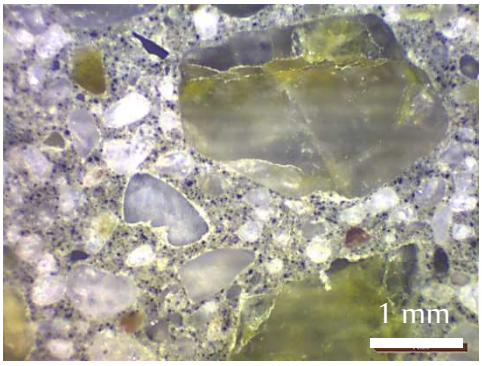

(a)

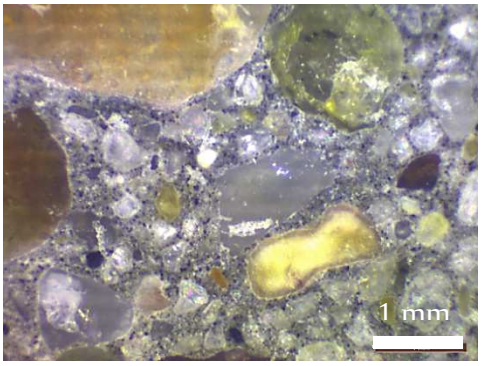

(b)

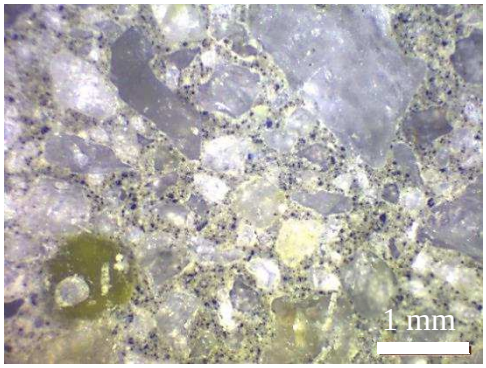

(C)

Figure 27. Epoxy impregnated (a) Reactive-1, (b) Reactive-2, and (c) Non-Reactive samples, which were exposed to the AMBT condition for fourteen days (Mr. Knapp performed the microscopy).

DRI values, obtained at six, ten, and fourteen days of exposure during AMBT, are significantly larger than those previously reported for concrete (Figure 28). This likely stems from the aggressive nature of the AMBT compared to field exposure and the smaller aggregate size in mortars compared to concrete. In other words, since in the calculation of DRI for mortar samples, defects associated with coarse aggregates in concrete were assigned to those with fine aggregate in the mortar, a larger number of defects per 100 cm^2

is observed in the mortar samples compared to concrete samples having the same geometry and exposure condition. However, if the number of defects per 100 cm^2 is scaled down to be proportional to the ratio of the size of the grids used in the mortar and concrete $\left(\frac{2\times 2\ mm^2}{15\times 15\ mm^2} = 0.0178\right)$, then the DRI values for the 1.78 cm^2 of mortar samples are in the range of 57 to 137, which is comparable to the DRI values reported for the 100 cm^2 of concrete [131,132].

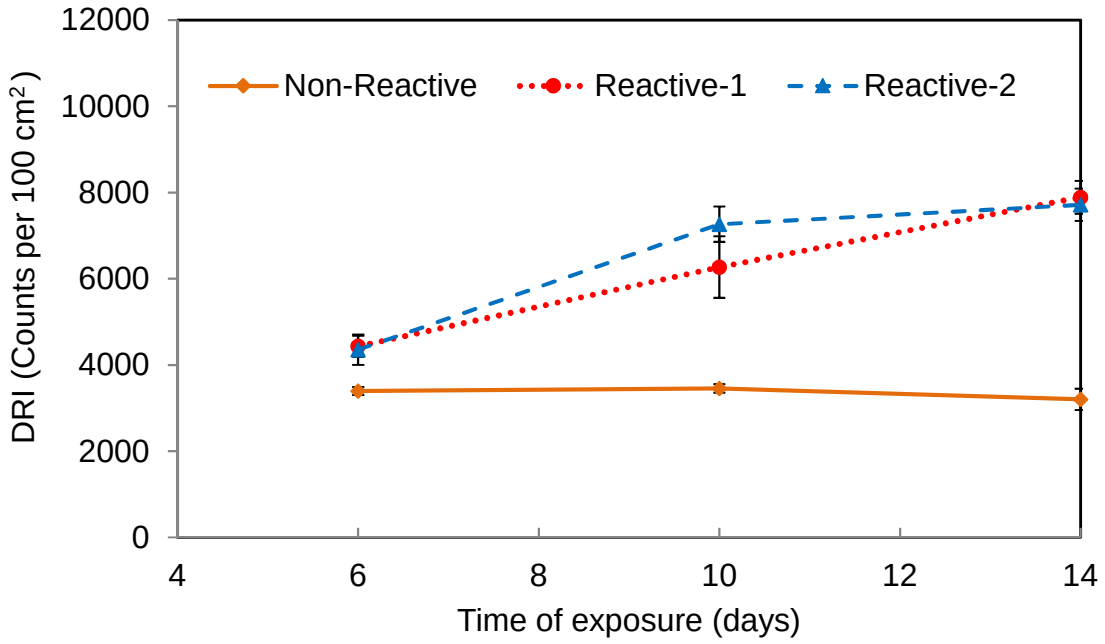

Figure 28. DRI values at different ages.

The DRI values do distinguish between potentially deleterious (i.e., Reactive-1 and Reactive-2) aggregates whose mortars show more damage and innocuous (i.e., Non-Reactive) samples. However, it is difficult to differentiate the level of damage between Reactive-1 and Reactive-2 samples; DRI values of Reactive-1 and Reactive-2 samples are

almost identical at day six and day fourteen. At day ten the average DRI value of Reactive-2 samples is larger than that of Reactive-1 samples, which has a large standard deviation.

To investigate the significance of the difference between the DRI values of the two potentially reactive aggregate at day ten, hypothesis testing is performed. The test statistically differentiates between those for the p-value of equal or bigger than 0.15 (a typical p-value is 0.01 or 0.05). Although the DRI values for the Reactive-1 and Reactive-2 samples may not be statistically different, their average DRI values follow different trends. The average DRI values and expansion increase linearly for the Reactive-1 samples, but for the Reactive-2 samples, the increase in the average DRI value from day ten to fourteen is less than the increase from day six to ten. This is similar to the trend also observed in the expansion data of the Reactive-2 samples. The DRI values of the Non-Reactive samples do not increase with the time of exposure, as would be expected.

6.4 Correlation between DRI and Expansion

The correlation between DRI values and the expansion data at days six, ten, and fourteen of the AMBT indicates a more consistent increase in the DRI and the expansion data for the potentially reactive samples than the Non-Reactive ones (Figure 29). In addition, the slope of the best linear fit to the data of each sample-type represents the increment of damage per unit expansion and it is different for the three sample types. The slope is larger for the Reactive-2 than the Reactive-1 samples suggesting more damage in the Reactive-2 samples than the Reactive-1, at the same expansion level. Moreover, the slope of the best fit for the Non-Reactive aggregate is slightly negative.

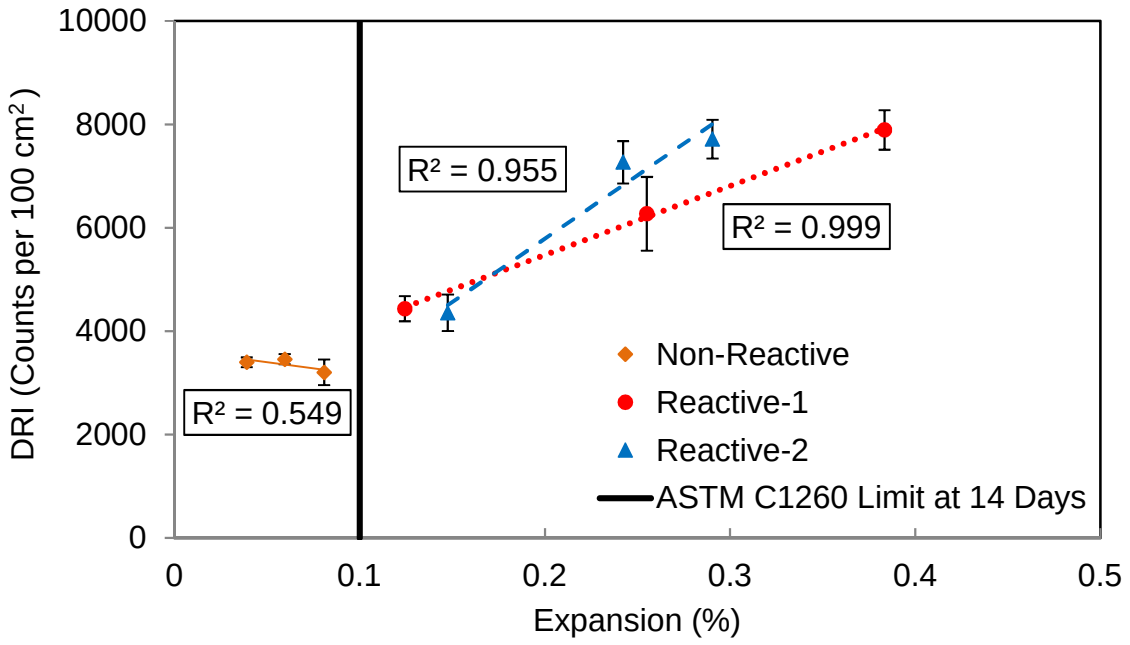

Figure 29. Correlation between DRI values and expansion data for the three types of aggregate. The expansion data and DRI values were measured at the days six, ten and fourteen of AMBT.

The DRI values may be used to screen ASR reactive aggregates. Considering the relationship between the DRI values and the fourteen-day expansion of sample types, potentially reactive samples experience greater DRI values and expansion than the Non-Reactive samples. While an increase in DRI is associated with increased fourteen-day expansion, the relationship between those two values is not linear. However, a limit could be established to screen the potentially reactive aggregates and nonreactive ones based on the damage estimated by the DRI.

6.5 NIRAS Measurements

The average nonlinearity parameter of the Non-Reactive mortar samples remains well below that of the potentially reactive samples for the duration of testing (Figure 30). Early in the exposure (i.e., at ~3 days exposure and earlier), the Reactive-2 samples exhibit the

highest nonlinear behavior among aggregate types. However, the nonlinearity parameter of the Reactive-1 samples surpasses that of the Reactive-2 mortars by day four, and at day six, the Reactive-1 samples exhibit the highest measured nonlinear behavior among aggregate types.

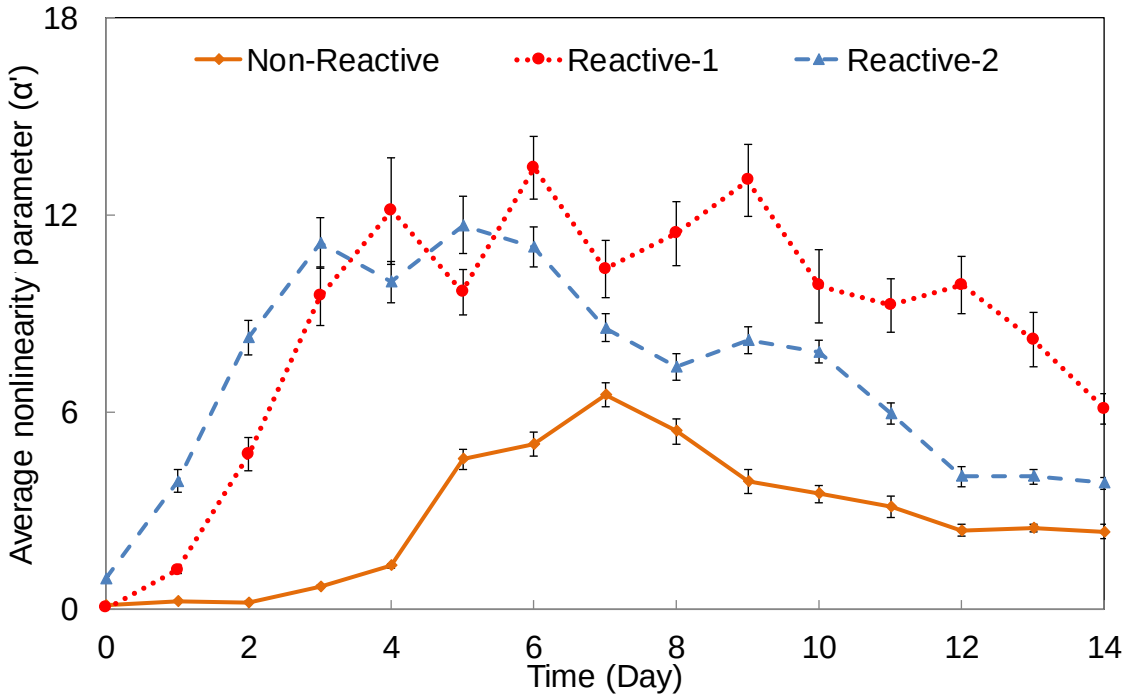

Figure 30. Temporal average nonlinearity parameter.

The average nonlinearity parameters of all three mortars types show an oscillatory or up/down behavior; this trend in behavior is consistent with prior NIRAS measurements on the ASR-affected mortar and concrete samples [14,88,117].

6.6 Relationship between Acoustic Nonlinearity and Expansion of ASR-Affected Cement-Based Materials

6.6.1 Acoustic nonlinearity measured by NIRAS, and expansion

To explain the relationship between the acoustic nonlinearity measured by NIRAS, and expansion of ASR-affected samples, along with linear acoustic measurements on these samples (Figure 31), the results of expansion, and linear and nonlinear acoustic measurements of studies by Chen et al. [88], and Lesnicki et al.[117] are shown in Figure 32 through Figure 34. The first study was performed on mortar bars exposed to the ASTM C1260 environment, while the second one represents the results for concrete prisms exposed to the ASTM C1293 condition.

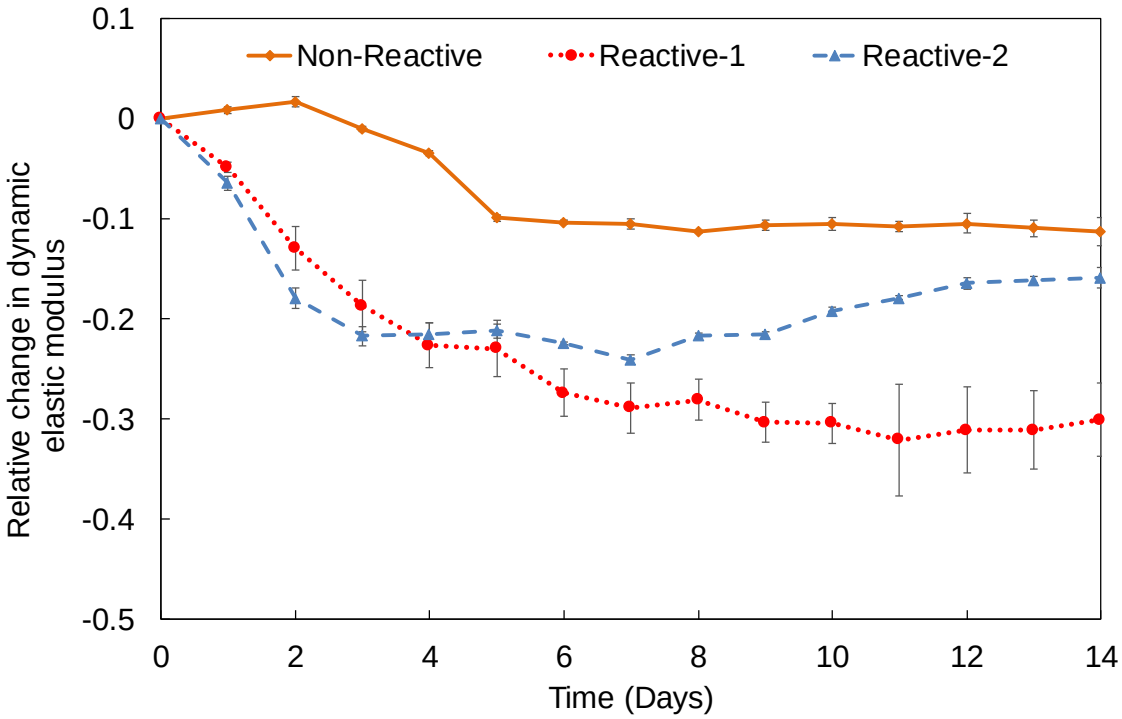

Figure 31. Relative change in the dynamic elastic modulus of mortar bars exposed to the ASTM C1260 environment.

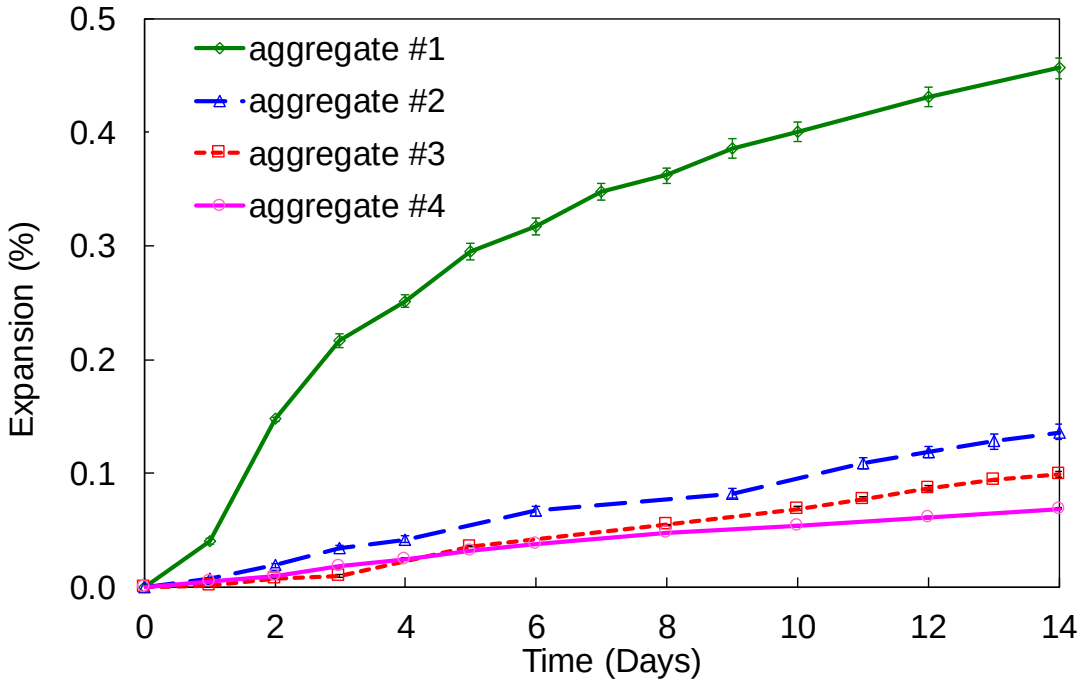
aggregate #1
aggregate #2
aggregate #3
aggregate #4
Expansion (%)
Time (Days)
0.0
0.1
0.2
0.3
0.4
0.5
0
2
4
6
8
10
12
14

(a)

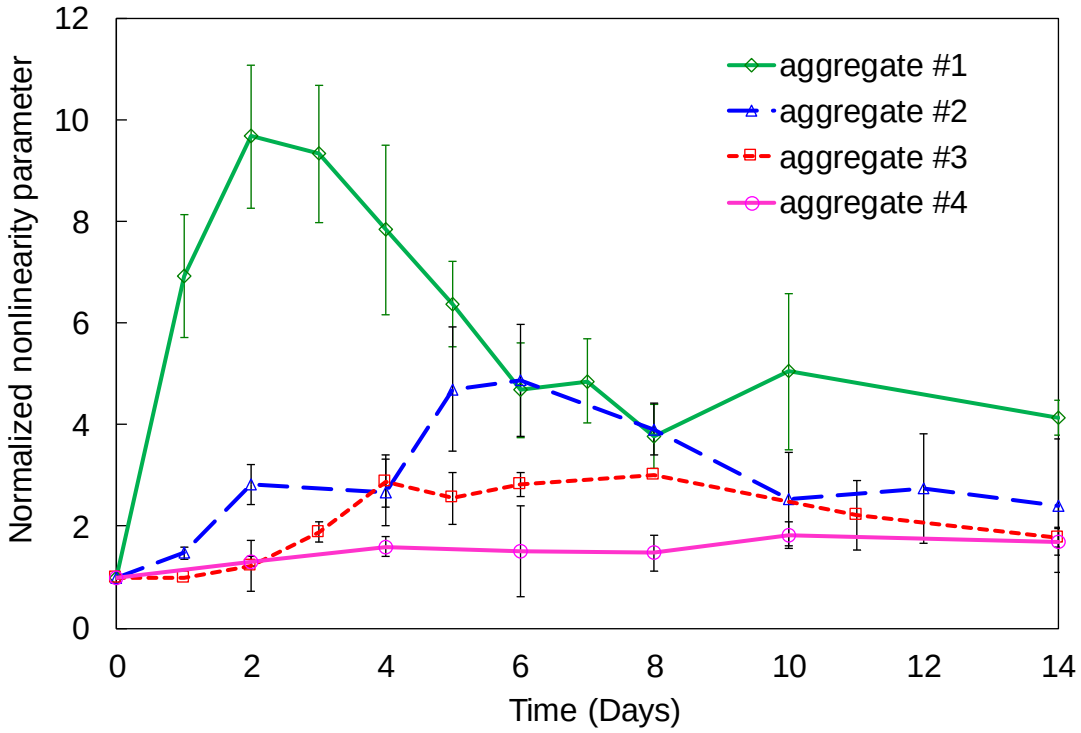
aggregate #1
aggregate #2
aggregate #3
aggregate #4
Normalized nonlinearity parameter
Time (Days)
0
2
4
6
8
10
12
0
2
4
6
8
10
12
14

(b)

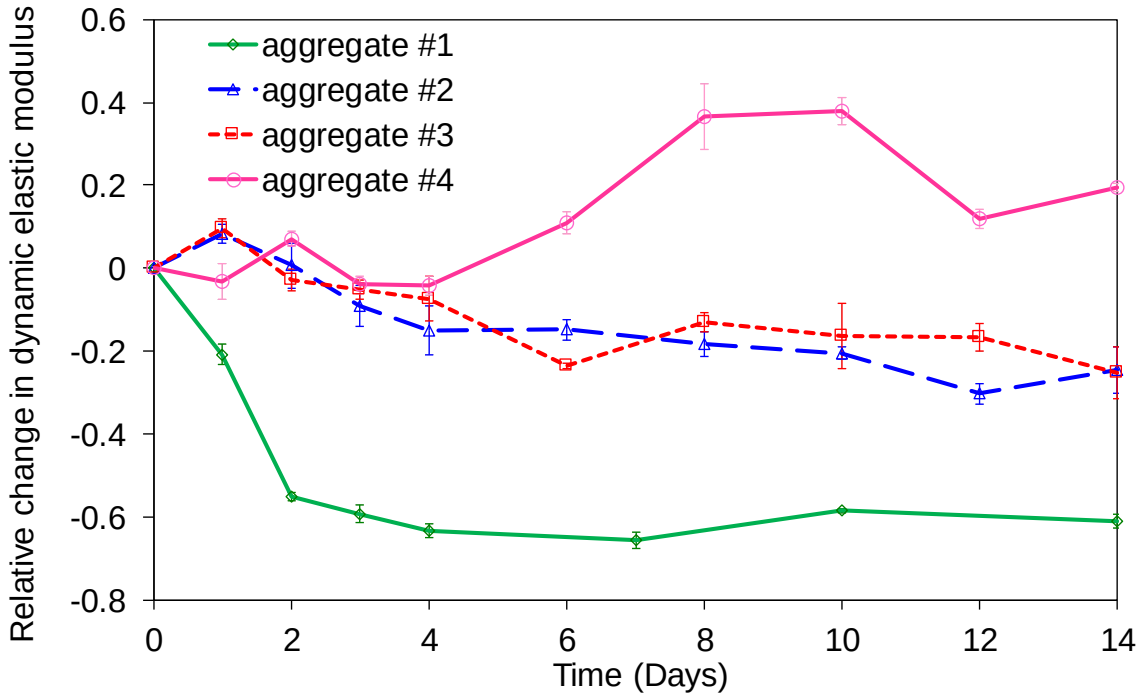

(c)

Figure 32. (a) Expansion, (b) temporal nonlinearity, and (c) relative change in the dynamic elastic modulus of mortar bars exposed to the ASTM C1260 environment [88].

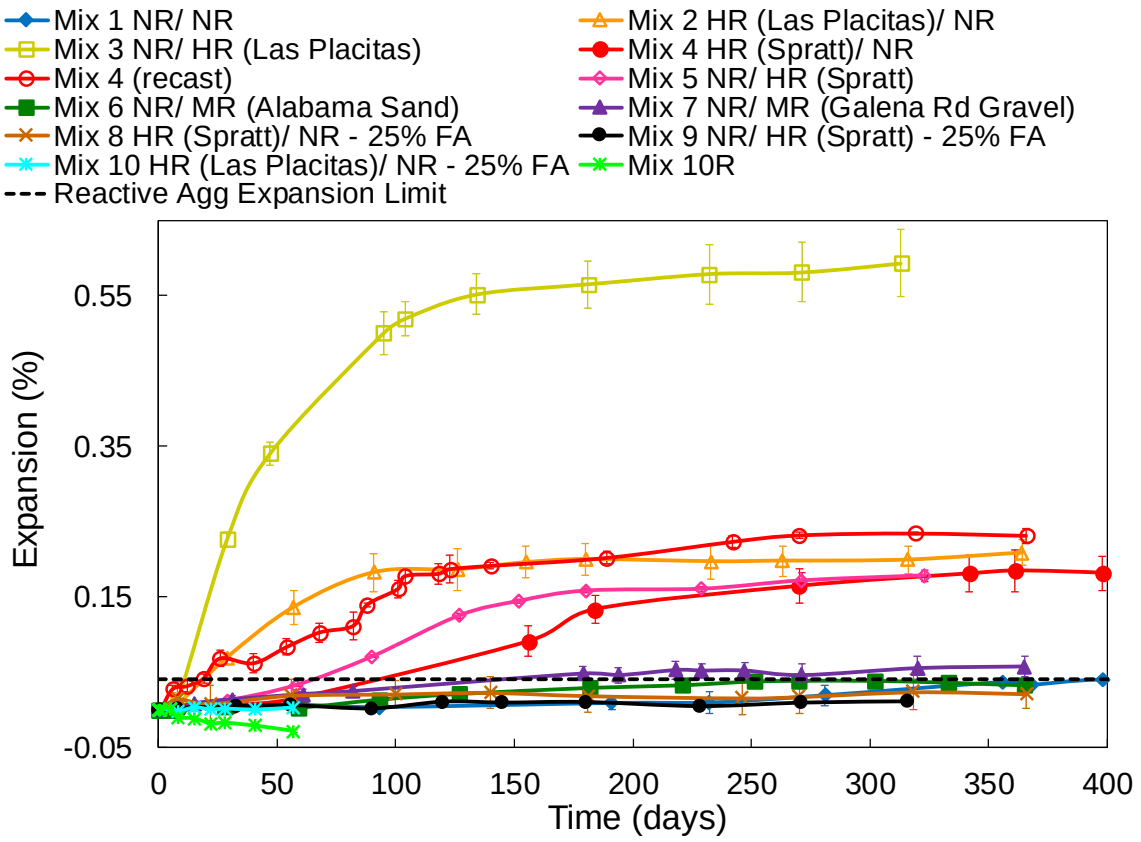
Mix 1 NR/ NR
Mix 2 HR (Las Placitas)/ NR
Mix 3 NR/ HR (Las Placitas)
Mix 4 HR (Spratt)/ NR
Mix 4 (recast)
Mix 5 NR/ HR (Spratt)
Mix 6 NR/ MR (Alabama Sand)
Mix 7 NR/ MR (Galena Rd Gravel)
Mix 8 HR (Spratt)/ NR - 25% FA
Mix 9 NR/ HR (Spratt) - 25% FA
Mix 10 HR (Las Placitas)/ NR - 25% FA
Mix 10R
Reactive Agg Expansion Limit
Expansion (%)
0.55
0.35
0.15
-0.05
0
50
100
150
200
250
300
350
400
Time (days)

(a)

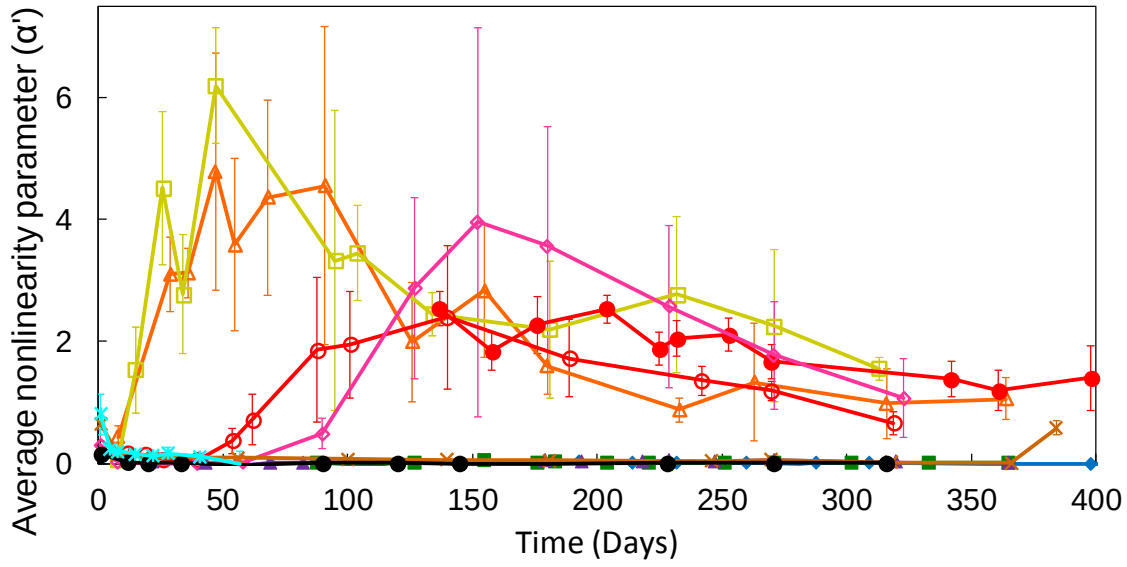
Average nonlinearity parameter (α')
6
4
2
0
0
50
100
150
200
250
300
350
400
Time (Days)

(b)

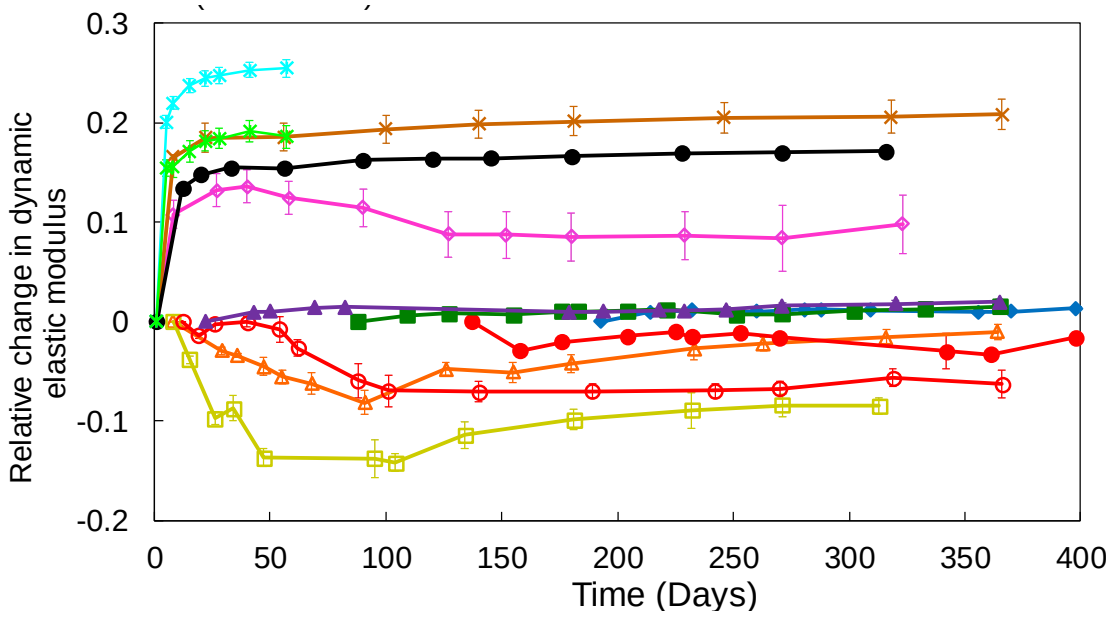

(c)

Figure 33. (a) Expansion, (b) temporal nonlinearity, and (c) relative change in the dynamic elastic modulus of concrete prisms exposed to the ASTM C1293 condition [117].

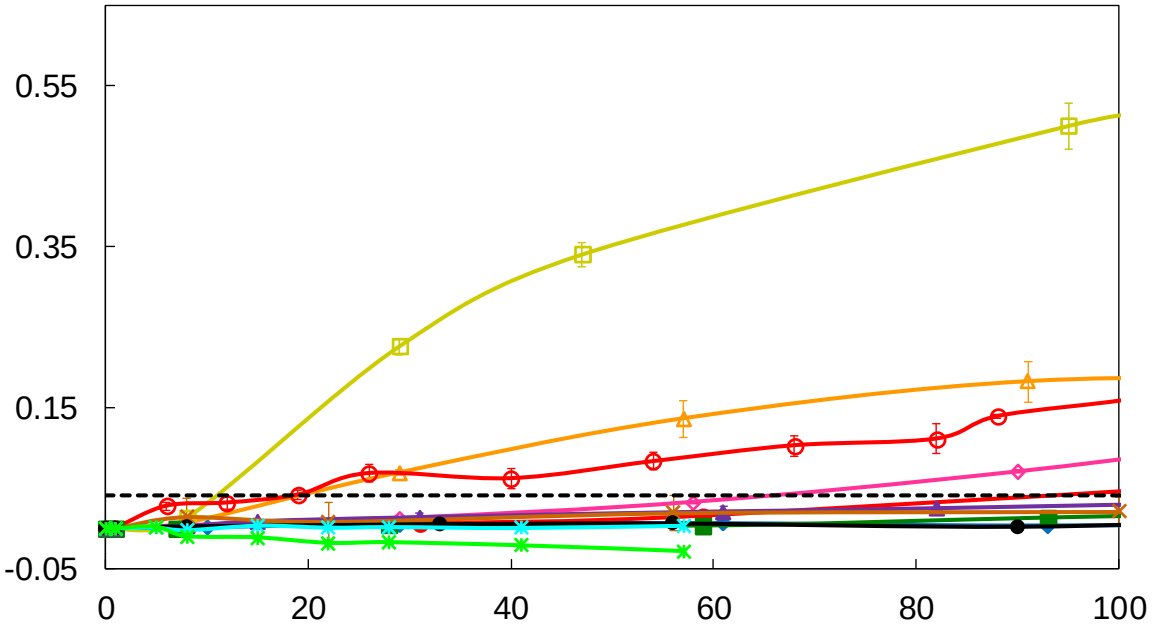

(a)

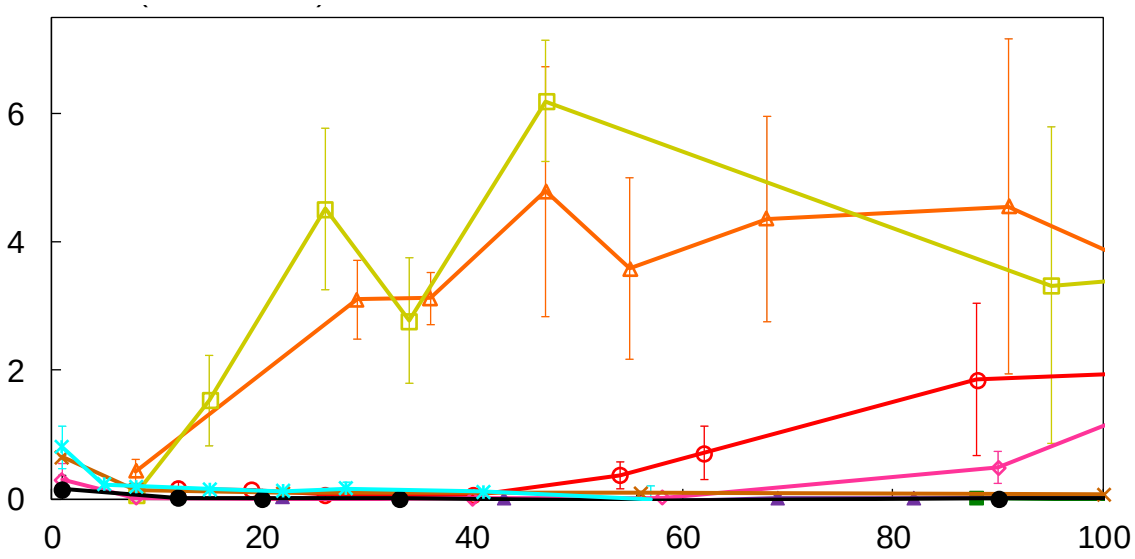

(b)

Figure 34. Early age (a) expansion and (b) temporal nonlinearity of concrete prisms exposed to the ASTM C1293 condition [117].

The important role of the interfacial transition zone (ITZ) during ASR and its role on the hysteresis nonlinearity of cement-based materials cannot be overestimated. In a width of typically less than 50 micrometer, a significant difference between the chemical properties of paste and aggregate including pH of cement paste (i.e., > 12.5) and that of aggregates (i.e., ≈ 7 unless ions are released by aggregates), creates a differential chemical potential due to the concentration of ions, and favors their transport toward the aggregate-paste interface. During ASR, as the hydroxyl ions and alkali cations break down the atomic structure of silica and dissolve it, they further weaken the ITZ region and increase the nonlinearity. However, at the early stages of ASR, the low viscosity gel (as explained in chapter 5) can pass through concrete porosity without causing damage. The higher porosity of ITZ makes the transport even easier.

Based on the above explanation, in the ASTM C1260 condition, which allows for calcium leaching, and increases

- pH and the concentration of alkali cations in mortars by soaking them in the 1N NaOH solution
- the surface area of aggregates by crushing,
- the temperature during the reaction (80 °C),

the significant level of nonlinearity in the reactive samples despite their low expansion level is mainly attributed to the dissolution of aggregates and weakening of aggregate-paste interface. At later ages, as the gel is well developed and it can cause substantial microcracking and damage, two mechanisms compete: (a) increase in nonlinearity due to microcracking effect, and (b) decrease in nonlinearity due to increased gel viscosity and pressure, which limits the interaction of microcrack asperities. As a result, nonlinearity shows variations. Afterward, as calcium replaces monovalent alkali ions through the process of alkali recycling, it forms a highly viscous and high yield stress ASR gel or structures similar to C-S-H. These products strengthen the weak interfaces, and as the high yield stress (and potentially expansive) gel does not flow to the surrounding pores during acoustic excitations, it limits the interaction of interfaces and it may even isolate aggregates from the paste (as in Figure 2), and nonlinearity significantly decreases. Such a process at later ages can be also observed in the

- partial recovery of dynamic elastic modulus for samples showing substantial ASR reactivity at the early days of the reaction, while they expand at a lower rate at later ages (i.e., Reactive-2 samples in Figure 31)

- approaching an asymptotic value for dynamic elastic modulus despite an increase in the expansion, (i.e., Reactive-1 samples in Figure 31, and aggregate #1 in Figure 32c).

Although cement hydration might have contributed to the increase in the dynamic elastic modulus of mortars, a similar phenomenon is observed for concrete prisms exposed to the ASTM C1293 condition at later ages, when the effect of hydration is minimal (Figure 33c).

For concrete samples exposed to the ASTM C1293 condition, the overall behavior of temporal nonlinearity is similar to that of mortar bars undergone ASTM C1260 condition. However, in contrast to the ASTM C1260 samples, the ASTM C1293 samples do not show a significant increase in nonlinearity prior to the initiation of expansion (Figure 34), which suggests the less significant effect of aggregate dissolution compared to the ASTM C1260 samples. This observation is consistent with the differences between exposure conditions in ASTM C1260 versus ASTM C1293. ASTM C1293 provides less source of monovalent alkali cations, lower temperature (38 °C), lower pH, and less surface area to the mass of aggregates than ASTM C1260. In addition, the concrete environment is richer in calcium due to the storage condition. In a calcium-rich environment, calcium can form a layer of C-S-H on the silicate aggregates and significantly reduce their dissolution [164].

With the initiation of expansion, as the dominating mechanism is microcracking, nonlinearity increases, and as the mechanisms of decreasing nonlinearity dominate the effect of microcracking at later ages, nonlinearity decreases. Interestingly, even when

expansion reaches an asymptotic value, nonlinearity may continue to decrease (i.e., after day 200 in Figure 33). As will be observed in the next chapter, a similar phenomenon occurs for samples undergoing DEF expansion. At later ages, presumably due to the increased microcracking of samples, the interconnectivity of pores increases, which can provide a path for relieving the expansive pressure of gel without causing damage. However, as gel passes through pores its calcium content, viscosity and potentially yield stress increases, and can fill microcracks and reduce nonlinearity.

It should be noted that acoustic nonlinearity evaluates the overall condition of a sample. For instance, in an ASR-affected sample, some aggregates may be still at the initial stages of the reaction, while in others the reaction might be quite developed (depending on the structure and availability of silica). Furthermore, the viscosity and expansivity of the gel at different locations in a sample can be quite different, which can result in different local nonlinearities in the sample.

The hypothesis provided here also explains that samples showing the same level of expansion do not necessarily show the same level of nonlinearity. At the same expansion level, for the ones that expanding at a faster rate, it is reasonable to assume that the dissolution of aggregate at the ITZ region occurs at a faster rate, and thus they may show higher nonlinearities.(See mix 2 and mix 4 at around 30 days in Figure 34). To further examine this hypothesis, the relationship between the damage measured by the quadratic acoustic nonlinearity and expansion of ASR-affected cement-based materials is investigated.

6.6.2 Quadratic acoustic nonlinearity and expansion

In contrast to the hysteresis nonlinearity, the temporal quadratic nonlinearity of ASR-affected samples tends to increase with expansion, even though a slight decrease at later ages is also observed. This difference most likely originates from (a) the nature of acoustic nonlinearity—energy dissipation in the case of α, and the presence of quadratic strain term in the stress-strain relationship of microcracks for β— and (b) the significantly larger excitation amplitude during resonance testing than the second harmonic generation (SHG) measurements. The large excitation amplitudes during resonance testing allow for the relative vibration of weak interfaces including aggregates against paste, and cause substantial energy dissipation through processes such as friction in the ITZ area. In contrast, due to the considerable lower excitation amplitudes used during SHG measurements, most likely, the effect of the weakening of ITZ is less pronounced except when significant microcracking occurs. Furthermore, it is theoretically shown that the presence of a viscous fluid inside microcracks may increase the quadratic and cubic nonlinearities [165]. However, for the ASR-affected cement-based materials the problem is more complex since typically both viscosity and the yield stress of the gel increase, which can limit the deformation of microcracks. Overall, while the trend in the behavior of temporal α and β versus expansion are different, their values for reactive aggregates are typically larger than those for potentially innocuous, and their potential decrease at later ages could be due to the formation of ASR gel with high calcium content within microcracks. The experimental results and the hypothesis presented here suggest that compared to the quadratic nonlinearity, hysteresis nonlinearity is more sensitive to the early-age detection of ASR-associated microcracks and late-age filling of them.

6.7 Summary

The results obtained from the three test methods including expansion, nonlinear acoustics, and quantitative petrographic analysis using the damage rating index (DRI) provide a better picture of how expansion and damage are linked during the AMBT test. The main findings of this chapter are as follows:

- DRI values increase over the time of exposure to the AMBT condition, and increase consistently with the expansion data for samples cast with potentially reactive aggregates, while this is not the case for the samples prepared with innocuous aggregate.
- Despite the increase in DRI and expansion, the acoustic nonlinearity measured by NIRAS tend to increase at earlier ages and then decrease by the end of AMBT exposure condition.
- A hypothesis is presented to interpret the acoustic nonlinearity of ASR-affected cement-based materials based on the different stages of ASR and underlying physics of acoustic nonlinearity parameters. It is suggested that the early increase in the hysteresis nonlinearity despite low levels of expansion is mainly due to the dissolution of aggregates and creation of low viscosity gel at early stages. This process weakens the interfacial transition zone (ITZ) and can cause substantial energy dissipation mainly due to mechanisms such as the friction hysteresis. However, at later ages, as a highly viscous and a high-yield-stress gel forms, it can strengthen weak interfaces such as the ITZ area and even isolate aggregates from the paste, which results in the decrease of acoustic nonlinearity and the partial recovery of the dynamic elastic modulus. On the other hand, since the amplitude of

excitation used for measuring the quadratic acoustic nonlinearity is substantially lower, most likely, the effect of weakening and strengthening of ITZ is less pronounced in measuring that parameter, and the value of quadratic nonlinearity tends to increase with expansion as excessive microcracking occurs.

This chapter concludes the first part of this dissertation dealing with ASR. In the second part, DEF will be studied.

CHAPTER 7. INSIGHTS INTO DEF-ASSOCIATED DAMAGE THROUGH ACOUSTIC NONLINEARITY

7.1 Overview

This chapter aims to address the third goal of this dissertation: to better understand the progression of DEF-associated damage. For this purpose, the acoustic nonlinearity (as a measure of microscale damage) and expansion of mortar bars were monitored over a year and the correlation between the two measures was examined. Samples were divided into two main categories: (a) the ones prepared with control sand (mainly quartz) and cements of varying in composition, and (b) those prepared with sulfate- and sulfide-bearing sand (acidic sand). Similarly, this chapter contains two main parts reporting the results on each of these categories and comparing them.

7.2 Results of Samples Prepared with Control Sand (CS)

To address each group of samples used in this study, the following abbreviation is used. Samples prepared with cement X and sand Y may be referred to as “X-Y samples”. For instance, samples made with Type I-A cement and control sand may be expressed as Type I-A-CS samples.

7.2.1 Expansion measurements

Expansion of mortar bars was measured periodically over 400 days of limewater storage. Data are shown for the normally-cured and heat-cured bars in Figure 35a and b, respectively; these are shown separately because of the marked differences in the ultimate

expansions experienced between the two sets of bars for each cement. For normally-cured samples, the maximum average expansions are less than 0.02% at the end of the storage period (Figure 35a). Those expansions are well below limits typically placed on mortars for deleterious expansion (0.1%) and can be attributed to water uptake [123,166].

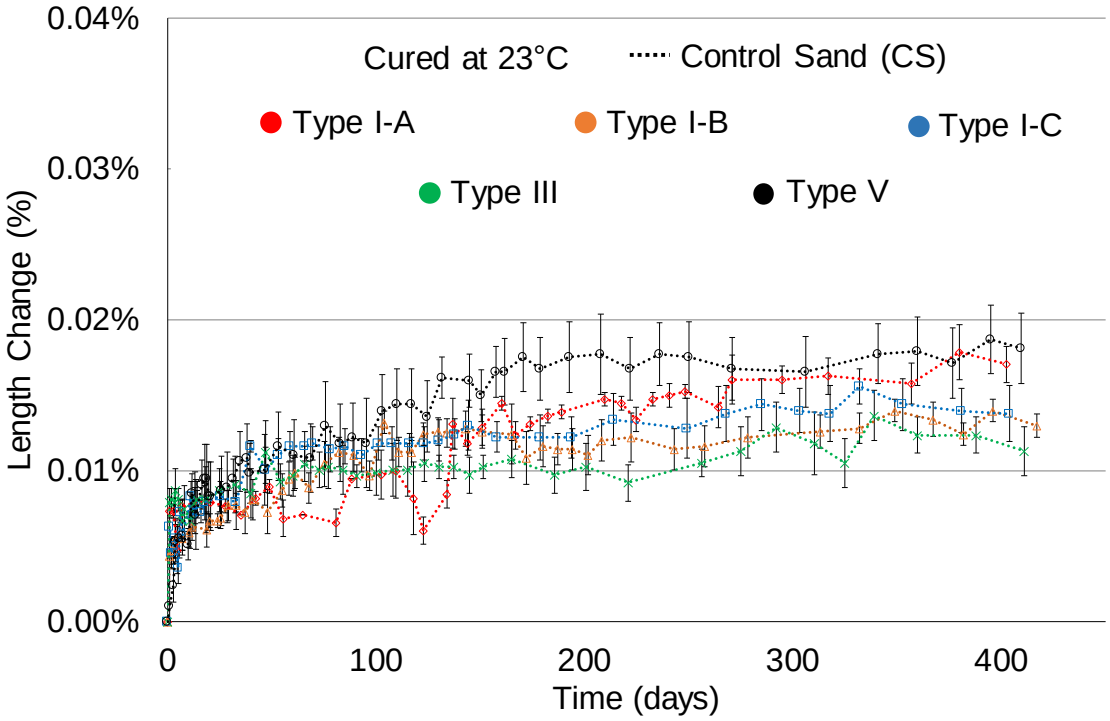

(a)

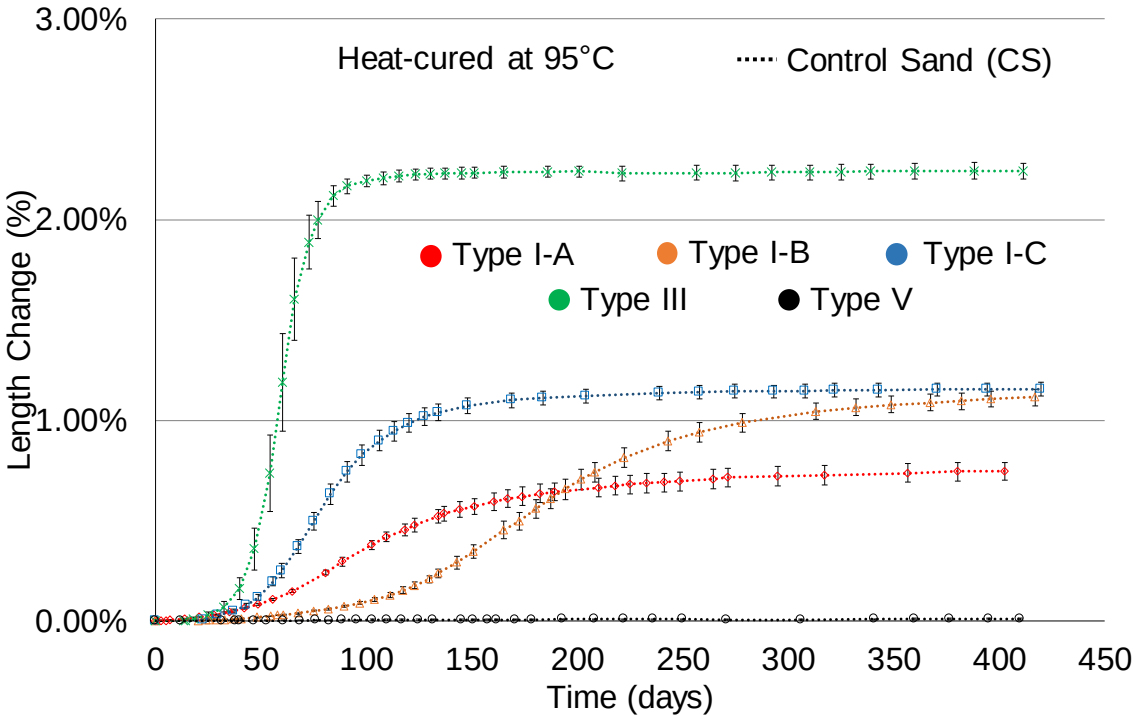

(b)

Figure 35. Length change of (a) normally-cured mortar bars (b) heat-cured mortar bars.

Results for the heat-cured bars (Figure 35b) show that mortar bars prepared with Type V cement exhibit expansion similar to normally-cured samples, suggesting that DEF did not contribute to expansion in these (further confirmation was explored by VP-SEM characterization [13]). In contrast, bars prepared with Type I and Type III cements show a 'S'-shaped expansion trend with time, which has been commonly observed for DEF-affected samples kept in laboratory testing conditions [68]. In such curves, an initial period of negligible expansion is followed by an accelerated expansion period until a final period of minor to no expansion is reached.

Considering the rate of developing expansion (shown in Figure 36 as average expansion per day) and the average expansion measured at the end of the exposure period,

specimens cast with Type III cement experience the earliest expansion and the most rapid rate of expansion among samples. The average 100-day expansion is approximately 2.2%, and the maximum rate of expansion is 0.075 (%/day), which occurs between days 53 and 54. Such behavior is likely related to the sulfate-to-alumina ratio of close to 1.0 [70], the higher sulfate and C_3A contents, and the greater fineness of Type III compared to Type I and Type V cements. According to Kelham [73], the expansion of mortar samples heat-cured at 90 °C increases with C_3A content and specific surface area of cement.

For mortar specimens prepared with Type I cements, both the rate of expansion and the ultimate expansion vary for different cement compositions (Figure 35b and Figure 36). Samples prepared with Type I-C cement experience the earliest expansion and largest expansion rate among Type I samples. While the maximum expansion of mortars cast with Type I-B cement is ultimately similar to that of specimens prepared with Type I-C cement, the early expansion rate of the Type I-B specimens is slowest among the samples cast with Type I cements. Furthermore, expansion occurs earlier for the Type I-A samples than the I-B samples, but the ultimate expansion for the Type I-A mortars is ultimately the lowest among the Type I mortars.

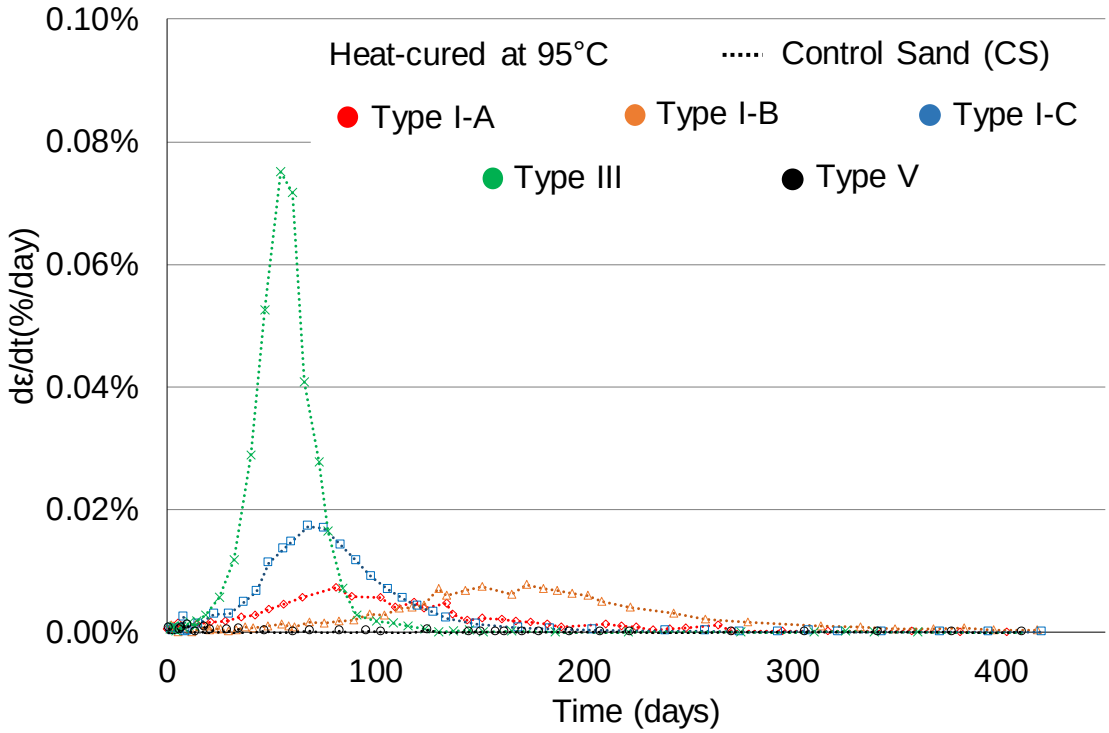

Figure 36. Rate of expansion of heat-cured mortar bars prepared with control sand.

Since the Type I cements have comparable fineness, the differences in the development of DEF derive from variations in the cement compositions. For example, with their similar alumina and C_3A contents, the higher sulfate content in cement I-B compared to cement I-A appears to be the underlying factor for the higher expansion in the Type I-B mortars (Figure 35b). That is, the higher sulfate content increases the potential amount of ettringite that can be formed for a given C_3A content [65,73]. While the I-C cement has a similar sulfate-to-alumina ratio as the less expansive I-A cement, the more accelerated and ultimately greater expansion of cement I-C bars compared to the I-A bars can be related to its higher C_3A content. The ultimate expansion of Type I-C and Type I-B mortars are similar, which is interesting considering that the C_3A content of Type I-C is higher and the SO_3/Al_2O_3 of Type I-B is higher. This analysis demonstrates that early rates of DEF

expansion appear to be more greatly influenced by C_3A content than the sulfate-to-alumina ratio, but that both factors play a role in ultimate expansion.

Referring back to the Type III mortar, which was cast from a cement with similar alumina and C_3A content to the Type I-C cement and somewhat higher SO_3/Al_2O_3 than the Type I-B cement, shows that both of these factors – along with fineness – contribute to the degree of ultimate expansion due to DEF. An existing predictive expansion model for DEF by Zhang et al. [167] incorporates the effect of SO_3/Al_2O_3 and C_3A content of cement, while the DEF model developed by Kelham [73] includes the effect of cement compositions and fineness as factors for predicting susceptibility to DEF. Although the Zhang model does not predict expansion for the Type I-A and Type I-C cements examined here, the trend in the final expansions measured for the cements considered in this study are consistent with the predicted expansions using Kelham and Zhang equations. That is, in these results as well as in predictive expansion models, Type I-A samples show the least amount of final expansion among expansive samples, Type I-B and I-C samples exhibit comparable final expansion, and Type III samples show the largest final expansion. Furthermore, the analysis of microstructure using VP-SEM with EDS microanalysis confirmed the microstructural distress due to DEF, and the higher extent of damage in the Type III samples than Type I ones. No sign of DEF-associated damage was observed in Type V samples [13].

7.2.2 NIRAS measurements

Figure 37 and Figure 38 show the temporal average nonlinearity parameter of normally-cured and heat-cured samples measured over at least one year of limewater

storage. When comparing α' values for heat-cured and normally-cured bars, a difference of approximately two orders of magnitude exists, with the normally-cured mortars having substantially lower nonlinearity at all ages than those measured in specimens undergoing DEF-expansion. The low values of α' for the normally-cured samples remain relatively constant since the first day of exposure. These values, which are typically less than 0.06, are mainly attributed to the effect of inherent defects, such as those present in the ITZ. This result indicates that no damage is developed during the 23 $^{\circ}$C storage period for the normally-cured samples. Furthermore, comparable α' measured for samples prepared with various cements indicates that difference in the hydration rate of cements during the exposure period has a negligible influence on the value of α'.

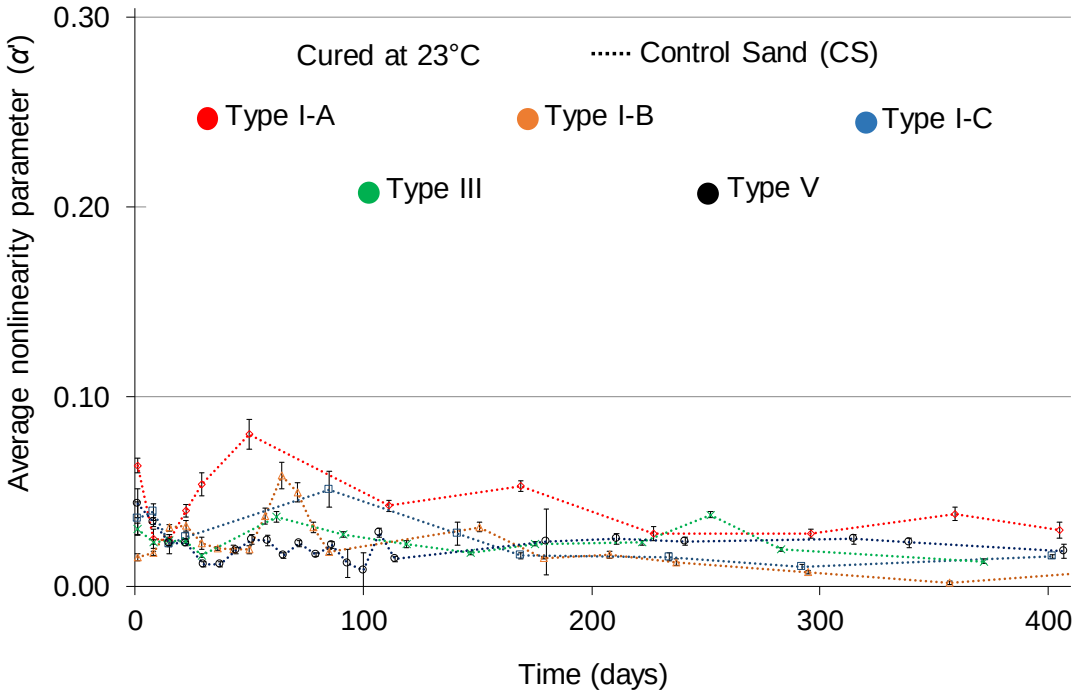

Figure 37. Temporal average nonlinearity parameter of normally-cured bars.

The temporal average nonlinearity parameter for heat-cured samples is distinct based on the cement used in the preparation of samples (Figure 38). Even for the first measurement, where α' is mainly affected by high-temperature curing cycle, samples show various damage levels. For instance, specimens cast with cements Type I-A, Type I-C, and Type III show comparable initial nonlinearities around 1.0. This is approximately six times larger than the initial nonlinearity of those heat-cured samples with cements Type I-B and Type V and more than one order of magnitude greater than nonlinearity of normally-cured samples. These results suggest that the higher initial value of α', observed in all samples exposed to the Kelham high-temperature curing cycle, is not solely due to the potential formation of microcracks as a result of the difference in the thermal expansion coefficient of mortar phases but is also related to cement composition (as it influences DEF).

Comparing the values of initial nonlinearities with the initiation of expansion, it is observed that expansion of samples cast with cements Type I-A, Type I-C and Type III initiates at an earlier age than those cast with cement I-B, and samples prepared with Type V cement show negligible expansion. This suggests a correlation between initial average nonlinearity parameter and the time when DEF-related expansion starts. According to Taylor [65], microcracking caused by thermal stresses favors the formation of DEF by providing an easier path for the transport of water, and weakens the mortar/concrete microstructure (i.e., weak aggregate-paste interface), which is responsible for resisting damage against DEF crystallization pressures. In contrast, a more intact microstructure should provide greater resistance to moisture ingress and also resistance to DEF crystallization stresses, limiting both the extent of reaction and subsequent expansion [65]. Therefore, the correlation of initial nonlinearity and the time of initiation of expansion can

be linked to the effect of microcracking caused during the high-temperature curing. This early sign of damage, detectable with NIRAS, can be an important tool for evaluation of DEF-susceptible concrete members in the field.

The average nonlinearity parameter measured at day one decreases during the first days to lower stable values. This can be likely attributed to the growth of hydration products as well secondary ettringite crystals in the weak interfaces and microcracks. Decreases in α' during this period are believed to derive from the limitation of the relative movements of weak interfaces and the decrease in the energy dissipation associated with that process. The decrease in nonlinearity is stronger for samples showing higher initial average nonlinearity, which suggest that a greater amount of DEF reaction products fill weak-interfaces in those samples than the ones showing lower initial nonlinearities. Furthermore, among samples showing higher initial nonlinearities, larger final expansion and a more significant decrease in the initial nonlinearity are observed for Type I-C and Type III samples than Type I-A samples. Therefore, for samples showing comparable initial nonlinearities, this observation may suggest a correlation between a decrease in initial nonlinearities during the early days of exposure, which is linked predominantly to secondary ettringite formation in microcracks, ITZ gaps, and voids, and the final expansion of DEF-affected mortars.

For the heat-cured samples, α' increases after reaching a local minimum. This increase occurs at day eight of exposure for samples cast with Type III and Type I-A cement, and at day 15 of exposure for those cast with Type I-B and Type I-C cement. Furthermore, the local minimum for samples cast with Type V cement occurs at day 30. Afterwards, α' in expanding samples increases with DEF-induced expansion. In contrast,

for samples cast with Type V cement the increase is very small, and except for early days of exposure where α' is affected by Kelham high-temperature curing cycle, exhibit similar values of α' compared to normally-cured samples. This trend is consistent with expansion data, where samples prepared with Type V cement show similar expansion to that of normally-cured samples (Figure 35).

The rate of increase in α' after reaching a local minimum is larger for samples showing earlier initiation of expansion. Samples cast with Type III, Type I-A, and Type I-C cements show a higher rate of increase compared to those cast with Type I-B and Type V cements. The former group of samples also exhibit higher initial α' and earlier time for the initiation of DEF expansion. In other words, samples showing stronger DEF activity also show a more significant change in nonlinearity. In contrast, for samples cast with cement Type I-B, where expansion occurs at a low rate, α' gradually increases and reaches a local maximum at day 64. At this time of exposure, the magnitude of nonlinearity is approximately four times than its magnitude at first local minimum. Such variation of α' while expansion is still at initial stages indicates the sensitivity of acoustic nonlinearity to the microstructural evolution caused by DEF.

As has been previously observed for ASR-affected mortar bars [88,95] (Chapter 6), the trend in the average nonlinearity parameter initially is increasing and then, as the reaction progresses and damage develops further, is decreasing. For samples cast with Type III cement this trend is most evident in Figure 38; nonlinearity increases after reaching the first minimum at day 8 and then decreases at day 70 of exposure. Between day 8 and 29 of exposure, when the expansion level is even less than 0.051% (well below 0.1%), an increase in nonlinearity forms a leading indication of DEF-induced damage. Furthermore,

a rapid increase of α' is observed between day 39 and 70, which coincides with the beginning of the period where DEF-expansion for the same specimens (Figure 35) increases from an average of 0.15% to 1.75%. After 70 days of exposure, when expansion is around 75% of the ultimate expansion, α' reaches a maximum average value of 27.7. To contrast, this is two orders of magnitude higher than the α' measured at first local minimum and approximately 30 times than the initial α'. The steep increase in expansion and nonlinearity suggests that the dominating damage mechanism during this period is microcracking. Afterward, a decreasing trend in nonlinearity is observed from day 70 (Figure 38), which corresponds to the start of the period of slow, asymptotic expansion. This trend is attributed to the domination of the effect of filling of microcracks by secondary ettringite formation over the generation of microcracks on α'. Precipitation of ettringite in voids, cracks, and ITZ gaps, which does not occur immediately due to transport limitations, does not lead to substantial crystallization pressure required for expansion [74]. This correlation between nonlinearity and expansion data over time shows that although in the DEF-affected samples may reach an asymptotic expansion value, the reactants may not be depleted and secondary ettringite can continue to form in the gaps and microcracks.

Similar trends are observed in the temporal average nonlinearity parameter of samples prepared with Type I cements. The temporal α' shows sensitivity to the microstructural evolution even when the expansion level is well below 0.1%. And for all Type I cement samples, it increases and then decreases after reaching an absolute maximum (Figure 38). The ratio of the absolute maximum of nonlinearity to the initial nonlinearity is around 3 for Type I-A and Type I-C samples and approximately 13 for Type I-B samples. Furthermore, the trend observed in the temporal α' is consistent with

expansion data (Figure 35). During the first 150 days of exposure, samples cast with Type I-A and Type I-C cements show more variation in α' than those prepared with cement Type I-B. The Type I-A and Type I-C mortars also exhibit larger expansion at earlier ages than those cast with cement Type I-B. In addition, the rate of decrease in nonlinearity after the absolute maximum is consistent with the expansion rate (Figure 38 and Figure 36). This observation suggests that secondary ettringite formation occurs in existing voids, microcracks, and ITZ gaps at earlier times and to a greater extent in samples which experience earlier and greater expansion. Similar to ASR samples (Chapter 6), the deposition of reaction products (secondary ettringite formation) at later ages strengthens weak interfaces and results in the partial recovery of the dynamic elastic modulus (Figure 39).

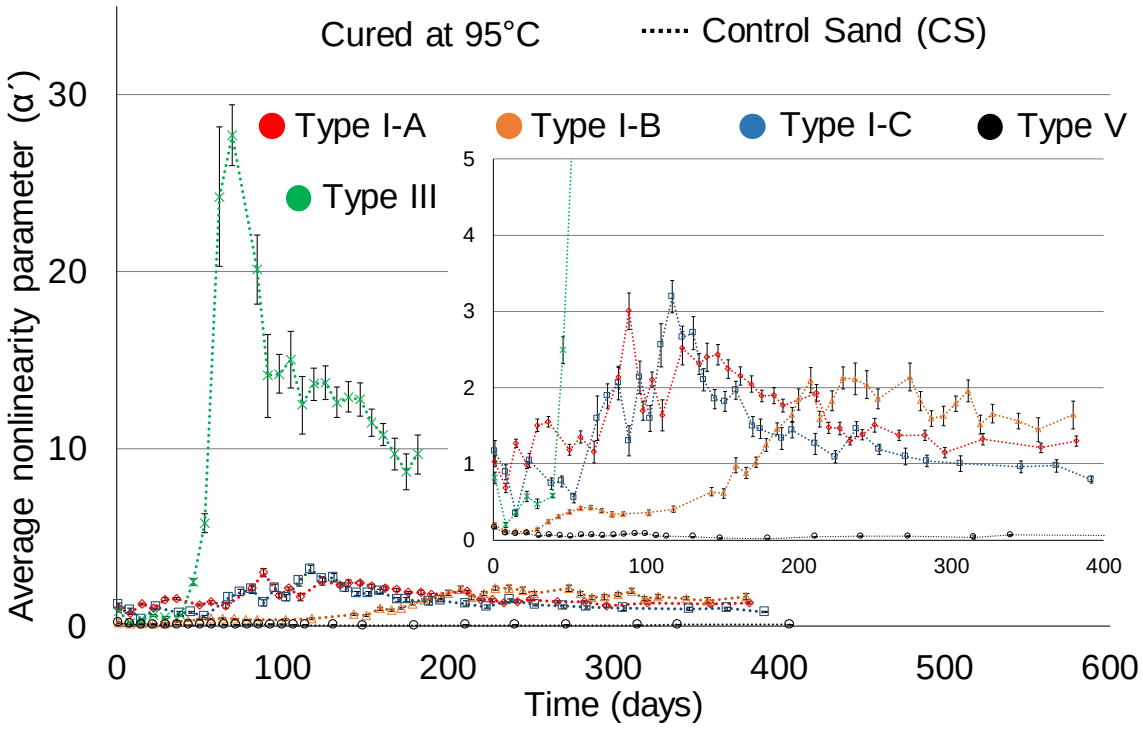

Figure 38. Temporal average nonlinearity parameter (α') for heat-cured mortar bars.

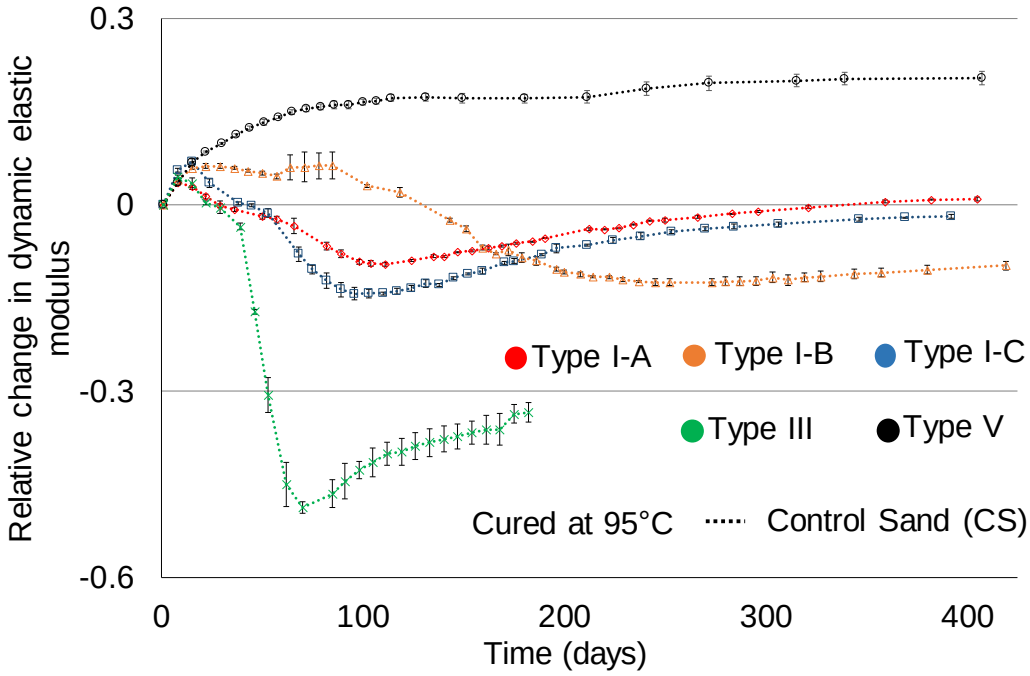

Figure 39. Relative change in the dynamic elastic modulus of heat-cured mortar bars.

In summary, regardless of the type of cement used in the preparation of mortar bars, α' of heat-cured mortars increases at a relatively rapid rate when the absolute expansion of mortar bars is between 0.13% and 0.17%, and it starts to decrease to more stable values when the expansion of mortar bars is between 75% and 90% of their asymptotic expansion value.

In the next part of this chapter, the results of expansion and nonlinear acoustic measurements of samples prepared with acidic sand (AS) are compared with the ones made with control sand (CS).

7.3 Comparison Between the Results of Samples Prepared with Acidic Sand (AS) Versus those Made with Control Sand (CS)

7.3.1 Expansion measurements

The expansion of normally-cured AS and CS samples show no significant differences, and it is substantially lower than 0.1%, indicating no effect of potential deleterious internal sulfate attack in the AS samples (Figure 40a).

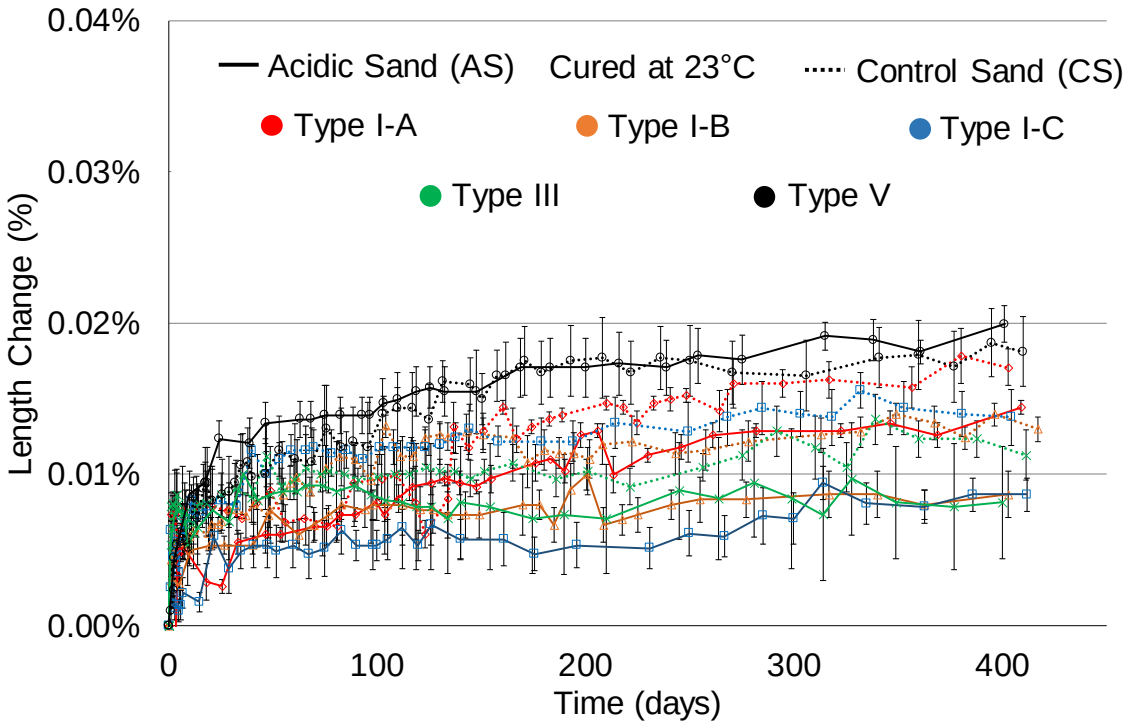

(a)

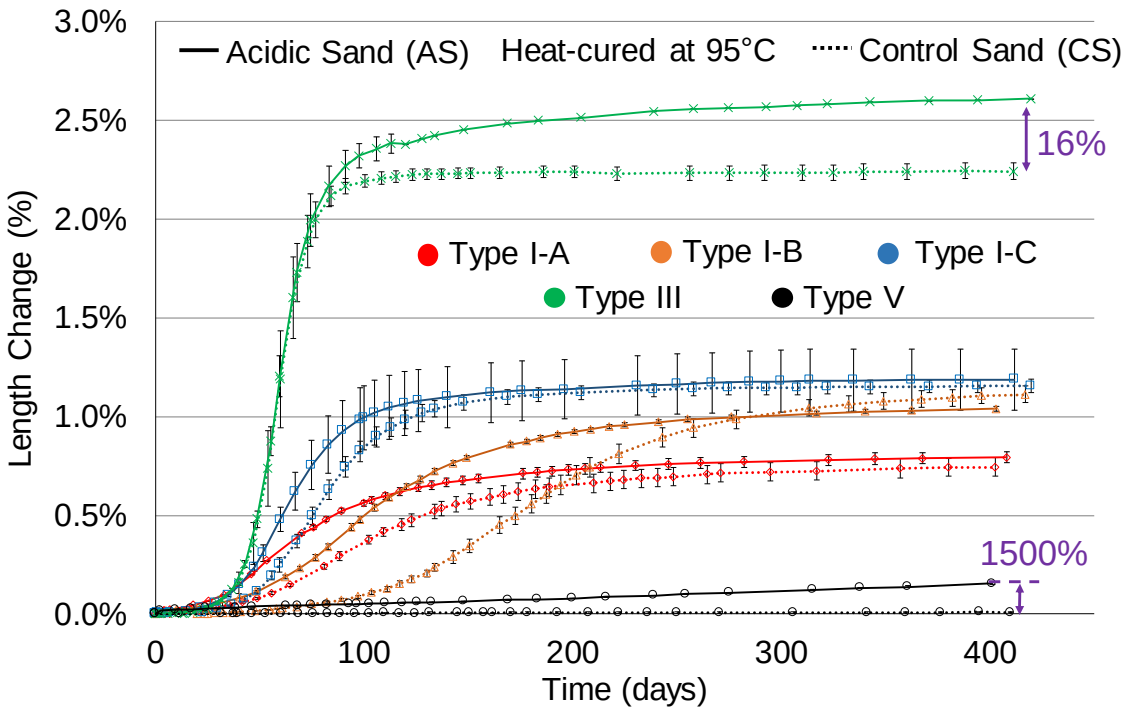

(b)

Figure 40. Length change of (a) normally-cured and (b) heat-cured mortar bars.

For the heat-cured samples, the ones prepared with acidic sand show differences in the time of initiation of expansion, maximum expansion rate, and asymptotic expansion values compared to CS samples (Figure 40b and Figure 41). The value of asymptotic expansion and maximum expansion rate of Type III-AS samples are 16%, and 9% larger than those of Type III-CS ones, respectively (Figure 41). In addition, the expansion of Type V-AS samples increases almost linearly after the third day of exposure, exceeds 0.1% by the end of one year, and reaches 0.155% at the end of the exposure period. This value is 1500% larger than the corresponding expansion value of Type V-CS samples. Such a significant difference between the expansion behavior of Type V-AS and Type V-CS

indicates the important role of aggregate type in mixes exposed to early-age high-temperature curing cycles.

For samples prepared with Type I cements, the use of acidic sand accelerates the initiation of expansion and increases the maximum expansion rate (%/day) by 19-30 %, however, does not have a significant effect on the asymptotic expansion values. The difference between the time of initiation of expansion for AS and CS samples is more significant in samples developing expansion at a slower rate, that is Type V> Type I-B> Type I-A> Type I-C> Type III. Therefore, in the field concrete, where DEF-associated expansion may occur over years and even decades, the use of acidic sands can threaten the durability and performance of structures.

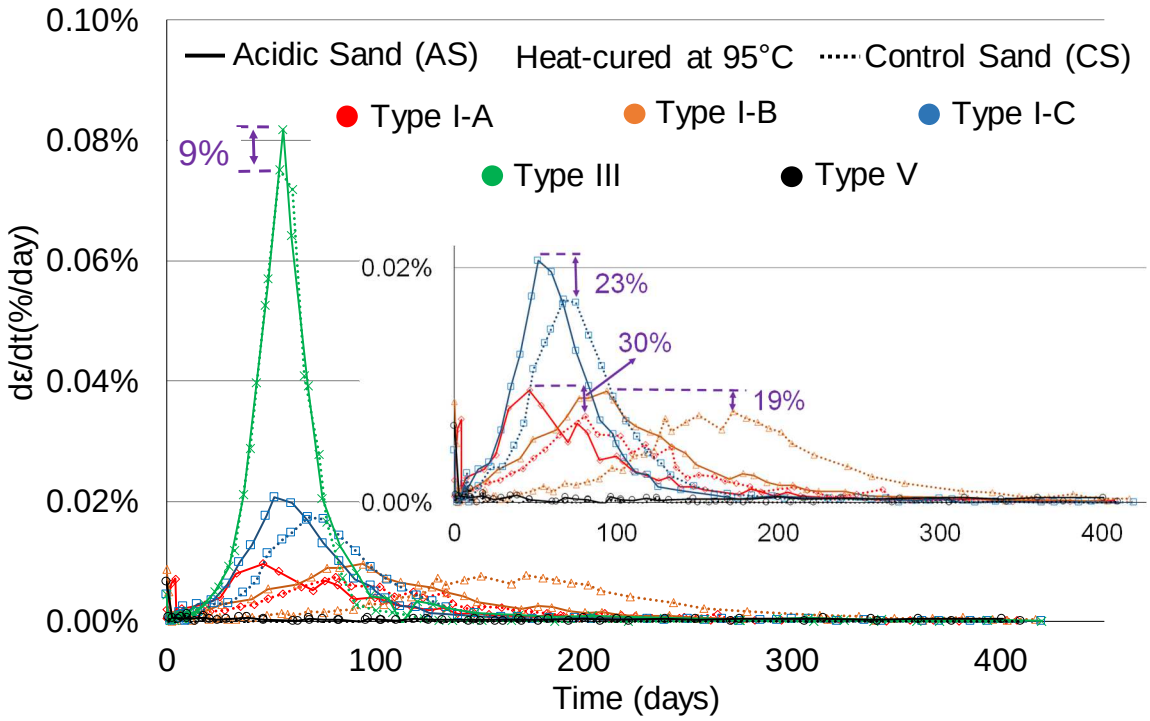

Figure 41. Rate of expansion of heat-cured mortar bars.

7.3.2 NIRAS measurements

The temporal acoustic nonlinearity of normally-cured and heat-cured samples are shown in Figure 42 and Figure 43, respectively. For the normally-cured samples, the acoustic nonlinearity of AS samples shows generally higher values than the CS samples at early ages (i.e., < 100 days in Figure 42) and reaches values comparable to the CS samples at later ages. This behavior could be attributed to the attack of calcium hydroxide on the alkali-feldspar aggregates to weaken ITZ and forming calcium aluminate products such as tetra calcium aluminate hydrate [168]. At later ages, with the release of sulfate from aggregates the calcium-aluminate forms ettringite [169] to strengthen the ITZ and reduce the acoustic nonlinearity.

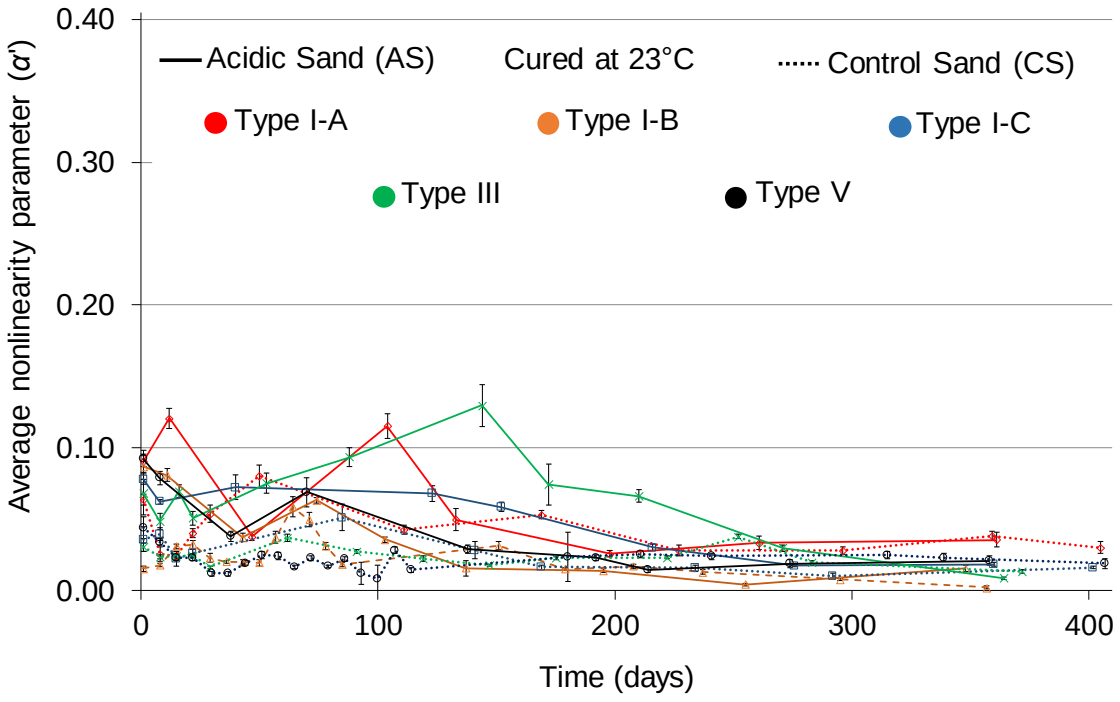

Figure 42. Temporal acoustic nonlinearity of normally-cured mortar bars.

For the heat-cured samples, regardless of cement used in this study, the temporal acoustic nonlinearity of acidic sand samples is distinct from that of control sand ones (Figure 43). The most significant difference between the AS and CS samples was measured right after the early-age high-temperature curing, with the damage in acidic sand samples (as measured by acoustic nonlinearity) is approximately an order of magnitude higher than the one in control samples. The initial nonlinearity in AS samples differs for each cement. Samples with higher initial nonlinearity tend to develop expansion at a faster rate. Presumably, the formation of excessive microcracking during the high-temperature curing contributes to this observation [13].

The significantly larger initial nonlinearity in the AS samples compared to the CS ones is attributed to the attack of $Ca(OH)_2$ on the alkali-feldspar aggregates. At 95 °C, this process degrades aggregates at a fast rate and results in the formation of hydrogarnet and C-S-H, and the release of alkali ions [170]. The release of alkali ions also increases the alkalinity of pore solution and results in the higher concentration of sulfate adsorbed by C-S-H [122]. The degradation of alkali feldspars and the evidence for the release of alkali ions were observed by microstructural analysis using VP-SEM with EDS microanalysis [122]. Aardt [170] hypothesize that if the concentration of released alkali ions reaches a certain level, it can further dissolve the C-S-H around the aggregate and weaken the aggregate-paste interface. Both the degradation of alkali feldspars and weakening of aggregate-paste interface favor the relative movement of asperities and increase of acoustic nonlinearity. The clear differences between the nonlinearity of AS and CS samples immediately after heat-curing suggest the potential for NIRAS as a rapid evaluation

technique for the quality control of aggregates prior to use in mass concrete or precast industries, where excessive heat may be produced.

CS and AS samples developing a substantial level of DEF-associated expansion show the general trend of decreasing in initial nonlinearity to reach a minimum followed by an increasing trend and later a decreasing behavior (except for Type I-C-AS samples where a clear absolute peak is not observed) (Figure 43). However, they also show differences: for instance, compared to Type III-CS samples, Type III-AS ones show more post-peak variations, which is attributed to their continued expansion, while the expansion of Type III-CS samples plateaus and the variation of nonlinearity diminishes (Figure 43a). Furthermore, for Type V samples, the heat-cured CS samples show nonlinearity values comparable to the normally-cured ones (consistent with expansion measurements), while the acoustic nonlinearity of AS samples increases after reaching an absolute minimum. Nonlinearity of these samples does not decrease at later ages as expansion monotonically increases and does not reach an asymptotic value.

Similar to Type V and Type III samples, the temporal acoustic nonlinearity of Type I samples is consistent with expansion. Type I-A-AS and Type I-B-AS samples show an earlier both increase in nonlinearity after reaching an absolute minimum, and reduction in nonlinearity at later ages compared to Type I-A-CS and Type I-B-CS samples, respectively. This observation is consistent with the first part of this chapter, which indicates that samples developing expansion at a faster rate, tend to experience an earlier decrease in nonlinearity due to the secondary ettringite formation. Furthermore, the lower levels of nonlinearity at later ages for the Type I-AS samples suggests the higher extent of secondary ettringite formation in these samples presumably due to the release of excessive

sulfate and sulfide from the acidic sand and adsorbed sulfate from C-S-H. However, given the significant difference between the absolute peak of nonlinearity between the Type III-AS and Type III-CS, and the continued expansion of Type III-AS samples, this statement does not necessarily imply less amount of secondary ettringite formation in former samples.

Type I-C-AS samples do not exhibit a clear absolute peak for the temporal nonlinearity. This observation could be attributed to the comparable rate of microcracking and deposition of ettringite in the microcracks. The high C_3A content of Type I-C cement and available sulfate could have resulted in the production of substantial levels of ettringite in nanopores and large porosities including microcracks. Overall, three main parameters seem to contribute to the differences in the expansion behavior and the microscale damage of samples prepared with control sand versus the ones made with acidic sand:

- accelerated attack of calcium hydroxide on alkali-feldspars at 95 °C to weaken microstructure and create microcracks
- release of alkali ions from alkali-feldspars to increase the sulfate concentration in pore solution and sulfate uptake by C-S-H [68]
- release of sulfate and sulfide from acidic sand to facilitate ettringite formation.

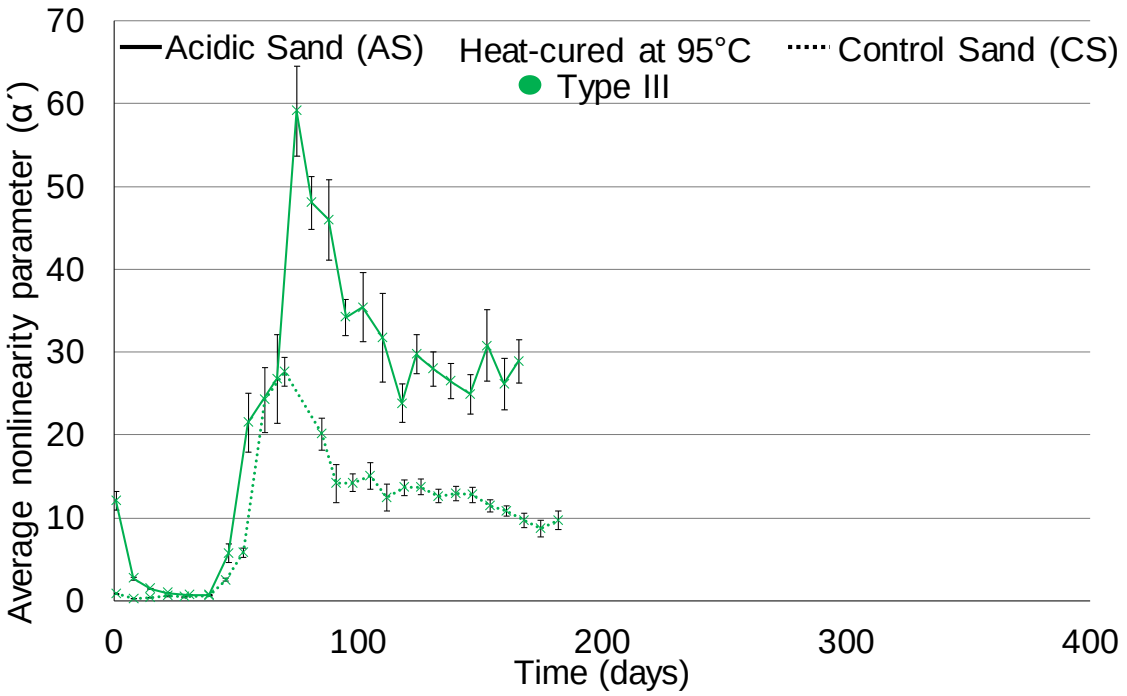
Acidic Sand (AS)
Heat-cured at 95°C
Control Sand (CS)
Type III
Average nonlinearity parameter (α′)
Time (days)
0
10
20
30
40
50
60
70
0
100
200
300
400

(a)

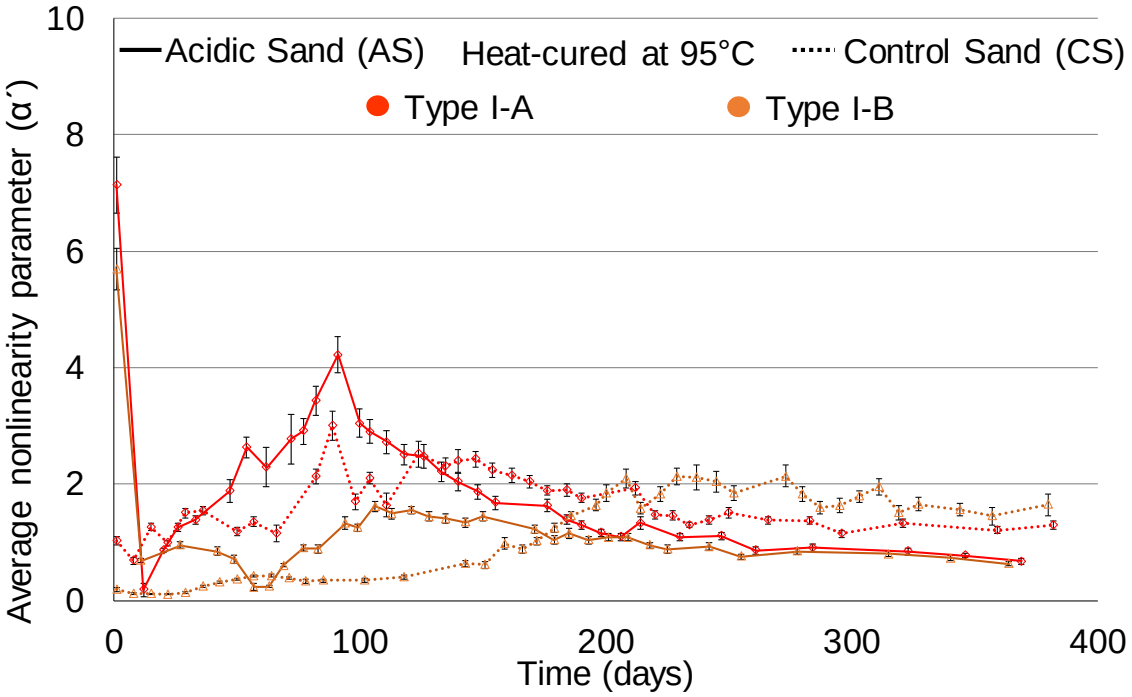
Acidic Sand (AS)
Heat-cured at 95°C
Control Sand (CS)
Type I-A
Type I-B
Average nonlinearity parameter (α′)
Time (days)
0
2
4
6
8
10
0
100
200
300
400

(b)

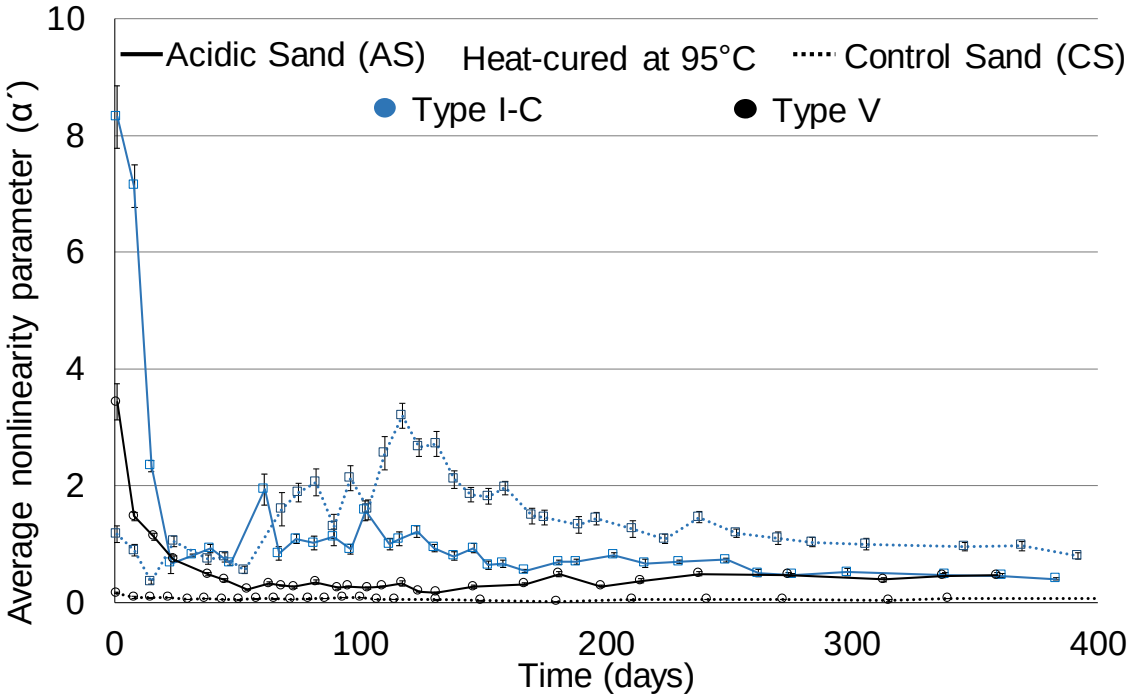

(c)

Figure 43. Temporal acoustic nonlinearity of heat-cured mortar bars (a) Type III (b) Type I-A and Type I-B, and (C) Type I-C and Type V samples.

7.4 Summary

Results obtained from expansion and nonlinear acoustic measurements are combined to improve the understanding of the role of cement composition and sulfate- and sulfide-bearing sand on the expansion and DEF damage in mortars subjected to the early-age high-temperature curing cycle. The main findings of this chapter are as follows:

- The early-age high-temperature curing cycle does generate microcracking which is measurable by NIRAS. For mortars prepared with control sand, which is mainly

quartz, the degree of initial microcracking varies for different cements. Mortar samples showing higher initial microcracking (as measured by nonlinearity parameter, α') are also the ones to develop the DEF expansion at earlier ages. Afterwards, in the first days of exposure to limewater, α' may decrease to lower values as hydration products and potential ettringite formation restrict the movements of microcracks during the NIRAS measurements. Later, for samples developing DEF-associated expansion, α' shows variation as mechanisms that decrease α' such as the formation of ettringite in microcracks, dominate those that increase α', such as microcracking. However, α' increases at a relatively fast rate when the absolute expansion of mortar bars is between 0.13% and 0.17%, and the overall trend of temporal α' is ascending. Then, as DEF progresses and expansion of mortar bars reaches values between 75%-90% of their asymptotic expansion, temporal α' also reaches its absolute maximum. The ratio of absolute maximum to the initial nonlinearity of mortar samples varies between 3 to 30, indicating that not only the range of damage experienced during the exposure period varies among the different cements but also demonstrates that the DEF damage can increase more than an order of magnitude greater than that experienced during the initial high-temperature curing cycle. Later, α' starts to decrease as the dominating mechanism is the formation of secondary ettringite in voids, ITZ gaps and cracks, which occurs earlier and to a greater extent in samples experiencing earlier and greater extent of expansion. However, since secondary ettringite does not generate large crystallization pressures required for expansion, subsequently the expansion rate slows and may reach an asymptotic value. In contrast, α' continues to decrease and

variations diminish, indicating that ettringite may continue to form in the voids, cracks, and ITZ gaps long after expansion reaches an asymptotic level.

- Results also show that the use of sulfate- and sulfide-bearing sand (acidic sand) accelerates the DEF-associated expansion, and it can further increase the long-term expansion level. The acceleration of expansion is more significant for samples showing low expansion rate when prepared with control sand (mainly quartz). Even with the use of sulfate-resistant cement, mixes made with this sand may develop deleterious expansion values when exposed to an early-age high-temperature curing and subsequent moist environment.
- While the initial acoustic nonlinearity of acidic sand samples varies based on the cement composition, those values are approximately an order of magnitude larger than the ones measured for the heat-cured samples made with control sand. The significantly higher level of damage is attributed to the accelerated attack of calcium hydroxide on the alkali-feldspars at 95 °C and the release of alkali ions to the pore solution. Alkali-feldspars form a significant portion of acidic sand particles. The main contributors to the differences in microscale damage and expansion behavior of acidic sand samples versus control ones seem to be
    - the accelerated attack of calcium hydroxide on the alkali-feldspars at 95 °C
    - the release of alkali cations from alkali-feldspars to increase the concentration of sulfate in pore solution and adsorbed sulfate in C-S-H
    - the release of excessive sulfate and sulfide from acidic sand
- Acidic sand samples that reach an asymptotic expansion values tend to develop expansion and nonlinearity at a faster rate, and exhibit lower values of nonlinearity

at later ages compared to the control ones, suggesting the deposition of more ettringite in the microcracks. Overall, the trend in the temporal nonlinearity and expansion are in agreement with each other.

- This study also shows the great potential for NIRAS as a fast nondestructive technique for the quality control of aggregates prior to use in mass concrete or in precast industries, where concrete mixes may be exposed to high temperatures.

CHAPTER 8. CONCLUSIONS AND FUTURE WORK

Overall, this dissertation uses an interdisciplinary approach to improve understanding of damage evolution due to alkali-silica reaction (ASR) and delayed ettringite formation (DEF), expansive chemical reactions damaging concrete structures. This research explores the role of reactant and product composition and structure in generating microscale damage, providing insight through the use of advanced characterization techniques, including nonlinear acoustics, damage rating index, nuclear magnetic resonance spectroscopy, small angle neutron scattering, and rheological measurements.

8.1 Summary of Findings

8.1.1 The role of composition in the structure of ASR sol and gel, and damage

- Small angle neutron scattering (SANS) results indicate that with the increase in the silica to alkali (S/A) molar ratio (SiO_2/A_2O, A= Na or K), the formation of dense mass fractal agglomerates is favored. However, the Na-based mixes tend to show more agglomeration. While the correlation length of agglomerates tends to grow with the further increase in S/A, at S/A=5, the ones in the K-based mixes are denser, as measured by their higher mass fractal dimension.
- The spin-spin relaxation rate of protons measured by the proton nuclear magnetic resonance relaxometry (^{1}H NMR) test indicates a bilinear trend with increase in the S/A of alkali-silicate mixes. The initial smaller slope is associated with sols, while the larger slope at higher S/A represents the higher ability of gels/precipitates in binding water. Although at low S/A, the Na-based mixes tend to show more water

binding abilities, at higher S/A results indicate the better ability of K-based samples in binding water.

- The dynamic viscosity of sols tends to linearly increase with S/A. However, as mass fractal agglomerates start to form, a clear deviation from the linear trend observed, with Na-based mixes tend to show higher viscosity than K-based ones. Overall, the dynamic viscosity, ^{1}H NMR, and SANS measurements are in a good agreement with each other.
- K-based sols can likely cause less extent of damage than Na-based sols due to their lower tendency toward agglomeration. They may pass through concrete porosities without causing damage.

8.1.2 Relationship between expansion, acoustic nonlinearity, and microstructural distress due to ASR

- Similar to the ASR-affected concrete, the extent of damage in the ASR-affected mortar can be evaluated by the quantitative petrographic analysis using damage-rating index (DRI). DRI values for the ASR-affected mortars are in a good agreement with expansion.
- In an alkali-rich environment, while expansion and the damage evaluated by DRI tend to consistently increase during the test duration for mortars containing potentially reactive aggregates, the temporal hysteresis acoustic nonlinearity does not monotonically increase. Instead, it follows an increasing and then decreasing trend. Based on the hypothesis presented in chapter 6, the increase in the hysteresis nonlinearity despite the low level of expansion is mainly due to the dissolution of

aggregates in the interfacial transition zone (ITZ) area, and the further weakening of the paste-aggregate interface. During the nonlinear acoustic measurement, the relative movement of aggregates against paste can substantially contribute to the energy dissipation through mechanisms such as friction, and cause a significant increase in the hysteresis nonlinearity. This behavior can be best seen in the mortar samples containing reactive aggregates and exposed to the ASTM C1260 condition, where the excessive availability of Na^+, high pH, high temperature, and increased surface area of aggregates facilitate their dissolution, and forms a low viscous gel, which can easily pass through the high porosity ITZ region without causing damage. Afterwards, as reaction develops and the viscosity and the yield stress of the gel increases due to the further dissolution of silica and incorporation of calcium, the gel is able to apply substantial pressure to the microstructure of cement-based materials and causes cracking. At this stage, two mechanisms compete: (a) the increase of nonlinearity due to excessive microcracking, and (b) the decrease of nonlinearity due to the increased gel pressure within microcracks, which can restrain the interaction of crack asperities. As a result, temporal nonlinearity shows variation as each of the mechanisms dominates the other one. At later ages, with the increased porosity of ASR-affected cement-based materials due to the excessive microcracking, ASR gel pressure can be relieved with the movement of gel through porosities, which can cause further incorporation of calcium in the gel structure and form structures similar to C-S-H. In addition, the presence of thick, high yield stress and viscous gel can isolate the aggregates from

the paste, and reduce nonlinearity. This layer also acts as the diffusion barrier for further alkali-silica reactivity.

8.1.3 Better understanding of the progression of DEF-associated damage

- NIRAS measurements on samples exposed to the early-age high-temperature curing and subsequent 23 °C-limewater storage indicate that heat-curing causes microcracking in all samples, with the DEF-associated expansion tend to initiate at an earlier age for samples showing higher levels of damage (as measured by acoustic nonlinearity) at the end of the heat-curing cycle. Afterwards, nonlinearity may decrease to lower values as hydration products and potentially ettringite fill microcracks. Similar to ASR, in the case of DEF two mechanism of increasing nonlinearity due to microcracking and decreasing nonlinearity due to deposition of reaction products (which is ettringite for DEF) compete with each other, and as each of them dominates the other one, nonlinearity shows variations. At later ages when the dominating mechanism is the deposition of secondary ettringite in large pores and microcracks, nonlinearity drops to lower values and its variation diminishes. Regardless of cement used in mixes prepared with control sand, which is mainly quartz, a noticeable increase in nonlinearity observed when expansion is in the range 0.13%-0.17%, and a clear decrease in nonlinearity is observed when expansion exceeds 75%-90% of its asymptotic value. The reduction of nonlinearity may continue long after expansion reaches an asymptotic value
- Depending on the cement, and curing and exposure conditions, the use of sulfate- and sulfide-bearing sand (acidic sand) can accelerate expansion, increase the maximum daily expansion rate, and even lead to the higher level of expansion at

the end of the exposure period. The acceleration of expansion is more significant for samples showing slower expansion development. Similar to the samples prepared with control sand (mainly quartz), the ones made with acidic sand show different damage levels at the end of heat curing, with their acoustic nonlinearity tends to be approximately an order of magnitude higher than that of samples made with control sand. Given that a significant portion of acidic sand particles used in this dissertation is composed of alkali-feldspar minerals, the higher nonlinearity of acidic sand samples at the end of heat curing is attributed to the accelerated attack of calcium hydroxide on the alkali-feldspars at 95 °C. Through this process, aggregates degrade, and alkali ions are released to the pore solution, which can increase the sulfate uptake by C-S-H. The later potential release of sulfate from C-S-H and from aggregates can exacerbate the damage due to DEF, and increase the ultimate expansion level.

For both ASR and DEF, this research shows the sensitivity of NIRAS to the presence of microcracking. It is also shown that while ASR and DEF are two distinctive expansive chemical reactions that may happen in cement-based materials, their temporal hysteresis acoustic nonlinearity share similarities such as decrease of temporal acoustic nonlinearity at later ages, and the partial recovery of the dynamic elastic modulus.

8.2 Recommendations

8.2.1 Recommendations for practice

Based on the results provided in this dissertation, it is recommended to continue using NaOH as the source of alkali cations in the standard test methods for the evaluation

of alkali-silica reactivity of aggregates. Although potassium seems to be the dominant alkali cation provided by cement in the field concrete, given the lower tendency of potassium-based sols toward agglomeration, most likely, potassium-based sols can cause less extent of damage compared to their corresponding sodium-based ones. Therefore, using NaOH in the standard test methods for ASR is likely a conservative approach for the screening of aggregates.

It is also shown that the nonlinear impact resonance acoustic spectroscopy (NIRAS) is an excellent technique to investigate the degradation of cement-based materials. While this technique is currently available in AASHTO TP 109 [171] for the ASR-affected concrete prisms, this dissertation brings new insights to the test results, which is important for the enhanced understanding of the state of ASR. Furthermore, although this study investigated the evolution of microcracks due to ASR and DEF, given the high sensitivity of NIRAS to the presence of weak interfaces, it is recommended to apply NIRAS to other degradation mechanisms. An area of interest is improving ASTM C666 test method [172], which evaluates the resistance of concrete to the accelerated freezing and thawing cycles. The test limits the number of cycles to 300 unless the dynamic elastic modulus of specimens drops to 60% of its initial values. Improving the standard by setting the relative change in nonlinearity as the criterion for accepting mixes allows for the lower number of cycles and makes the test more convenient.

NIRAS does not have the limitations associated with the standard test methods, which require a specific proportioning of aggregates, water, and cement, and an exposure condition for a certain period. As a result, NIRAS is recommended for the quality control of job mixes. Furthermore, one of the problems with the current standard test methods for

ASR is that either they are fast (16 days) but too aggressive as in ASTM C1260, or long (1-2 year of exposure) but more realistic as in ASTM C1293. This issue originates from using expansion as the criterion for differentiating between potentially reactive versus nonreactive aggregates. However, as shown in this dissertation, prior to the development of expansive gel, dissolution of aggregates occurs. The sensitivity of NIRAS to the early detection of ASR originates from its significant sensitivity to the presence of microcracks caused by dissolution of aggregates and expansion. It is recommended to use the absolute maximum of temporal acoustic nonlinearity for differentiating among potentially reactive versus nonreactive mixes. For susceptibility to DEF, it is also recommended to perform NIRAS on mixes exposed to the early-age high-temperature curing of above 70 °C. The initial high nonlinearity could be an indication for the accelerated DEF-associated expansion. However, there are also limitations with performing NIRAS on the field structures. Since this test requires a significant level of excitation energy, the current application of NIRAS is limited to the lab-produced samples or the cores from field structures. Furthermore, the results from NIRAS, as in other linear and nonlinear acoustic measurements, are sensitive to the environmental conditions including relative humidity and temperature. Therefore, for the direct comparison of acoustic nonlinearity of samples, it is recommended to expose samples to the same environmental condition prior to the test.

8.2.2 Recommendations for further research

While this dissertation studies different aspects of ASR and DEF, further studies are needed to confirm the relationships found here and to expand the application of current findings.

In chapter 5, the SANS measurements were only performed on the sols up to the S/A of 5. Given that the ^{1}H NMR results show larger differences between Na- and K-based gels/precipitates at higher S/A, it is recommended to perform SANS on alkali-silicate mixes at higher S/As. In such a case, the results of ultra-small angle neutron scattering (USANS) may need to be combined with SANS due to the increased correlation length of agglomerates. Furthermore, since the gels produced in the field concrete contain calcium, further studies on the role of calcium in the ASR mixes are needed.

In chapter 6 the relationship between expansion and damage measured by quantitative microstructural analysis using DRI, and hysteresis acoustic nonlinearity is investigated. However, it is important to note that the pattern of ASR damage varies with different aggregate sources and environmental conditions. For example, the accelerated test conditions used here may produce gel compositions and behaviors, which may or may not be representative of those found in the field, even for these aggregate sources. Therefore, further studies on mortars and concretes cast with aggregates varying in mineralogy and reactivity, exposed to both accelerated and field conditions, is needed to examine the correlations and trends observed in chapter 6.

Chapter 7 only investigates the role of five cements and two types of aggregates in mortars undergone Kelham early-age high-temperature curing cycle. As a result, further applications of NIRAS to various mortar and concrete mixes heat cured at different temperatures are needed to bring new knowledge on the effect of aggregate type and curing condition on the initial damage measured by nonlinearity, decrease of initial nonlinearity, time of initiation of expansion and ultimate DEF expansion of cement-based materials. Since NIRAS evaluates the state of weak interfaces including ITZ, the effect of aggregates

varying in morphology on the quality of aggregate-paste bonds after the heat curing can be investigated. For instance, it has been observed that expansion develops more quickly in the mixes prepared with quartz aggregates compared to other types of aggregates (i.e., limestone aggregates) due to the weaker bond between quartz aggregates and cement paste [65]. In addition, the effect of various curing conditions on the thermal damage (measured by material nonlinearity) and its effect on the temporal nonlinearity during the exposure period can be further studied. For the specific case of alkali-feldspar aggregates, NIRAS can be further applied for studying alkali release from alkali-feldspars at various temperatures. Numerous studies indicate a substantial amount of alkali release from this type of aggregate at 40 °C [173]. In other words, even by keeping the temperature below 70 °C in mass or precast concrete to avoid DEF, the alkali release from alkali-feldspars may contribute to alkali-silica reaction, indicating the importance of quality control of aggregates, especially in critical infrastructure.

In addition, further research is needed to better understand the mechanisms that affect the acoustic nonlinearity and properties of reaction products including:

- Developing physics-based models for the acoustic nonlinearity of cement-based materials

Despite the growing application of nonlinear acoustics to the evaluation of damage in cement-based materials, most of the studies remain at the observation level. This dissertation contributed to the body of knowledge by connecting the knowledge of nonlinear acoustics to that of cement-based materials. However, a physics-based model approach for the interpretation of acoustic nonlinearity of cement-based materials is still

missing. For ASR, a physics-based model can be developed based on the hypothesis presented in chapter 6. The model, which considers the gel-solid coupling at the microcracks' asperities, can be also used as a platform for modeling other chemical reactions such as DEF.

- Improving the current understanding of friction hysteresis in materials

Although friction hysteresis significantly contributes to the hysteresis acoustic nonlinearity of materials, it is not well understood. In fact, the most widely used model for hysteresis nonlinearity has a phenomenological nature, which ignores the surface morphology of microcracks. Further research in this area is needed to better understand the amplitude dependent internal friction of materials.

- Investigating the acoustic nonlinearity of highly nonlinear materials

Although the typical equation used for measuring the hysteresis acoustic nonlinearity of materials shows a linear relationship between the normalized downward shifts in the resonance frequency versus amplitude of excitation, it is not necessarily the case for highly nonlinear materials, including cement-based materials depending on their damage level. In fact, for highly nonlinear materials, the relationship can be quadratic [174]. Further studies in this area, especially through modeling, can bring insights to this behavior.

- Combining SANS measurements with ^{29}Si NMR results

Combining the information from SANS and ^{29}Si NMR allows for studying the structure of ASR gel at the atomic and molecular scales. For instance, although SANS provides information about the correlation length of agglomerates and how dense they are, it is not

sensitive to the heterogeneities at the atomic scale, and it does not provide knowledge about the connection of silicate tetrahedrons. This information can provide insights into the role of composition (including lithium and calcium), aging, pH, and temperature on the structural properties of ASR sol and gel.

- Investigating the differences between the nature of bonds between calcium and silicate structures versus those between monovalent alkali cations and silicates in ASR sol and gel

Although both monovalent alkali cations and calcium contribute to the structure of ASR products, the nature of their bond with silicate tetrahedrons seems to be different. Iler [37] argues that since Na- and K-based alkali-silicate gels can disintegrate in water, these cations may have bridged between silicate structures. However, C-S-H is stable in water. As a result better understanding of the difference in the nature of bond (i.e., in sphere versus out of sphere bonds) contributes to the fundamental understanding of both ASR sol and gel, and C-S-H.

APPENDIX A. MEASURING THE ACOUSTIC NONLINEARITY OF SMALL SAMPLES: BRIDGING BETWEEN NONLINEAR ACOUSTIC AND MICROWAVE MATERIALS CHARACTERIZATION TECHNIQUES

A.1 Overview

This chapter demonstrates the feasibility of performing NIRAS for evaluating the alkali-silica reaction damage of samples prepared for the S-band frequency range microwave measurements, the most appropriate frequency range to study cement-based materials [175].

A.2 Methodology

A.2.1 Materials, sample preparation, and exposure condition

Materials, sample preparation, and exposure condition are identical to those of chapter 3 for samples exposed to ASTM C1260 condition. The only difference is the sample size. For each aggregate, three cuboid mortar samples with the cross-section of 72.0×34.0 mm, and the thickness 20-30 mm were prepared. The samples were originally used for measuring the dielectric properties of mortars at the S-band frequency range (2.6-3.95 GHz) at the end of 14-day ASTM C1260 exposure [95]. The variation in the thickness of cuboid samples does not affect the dielectric properties of materials.

The acoustic nonlinearity of cuboid samples was measured approximately four years after casting. Although samples were kept in sealed containers at the lab temperature

(23 ± 1.5 °C) after the exposure period, by the time of nonlinear acoustic measurements, they seemed dry. Further details about sample preparation can be found in ref. [95].

A.2.2 NIRAS measurements

NIRAS measurements were performed as explained in chapter 2, except an impactor typically used for measuring the dynamic elastic modulus of concrete applied impacts (Figure 44). Compared to a hammer used in the NIRAS measurements of mortar bars and concrete prisms, the impactor has a significantly smaller mass, and the impact energy is substantially smaller, which allows for the stability of samples during the experiment. Signals were captured at the sampling frequency of 1.25 mega samples per second with the window of 0.4 seconds. A sample of time domain is shown in Figure 45, while Figure 46 shows the frequency domain response of a sample to multiple impacts, and the calculated acoustic nonlinearity.

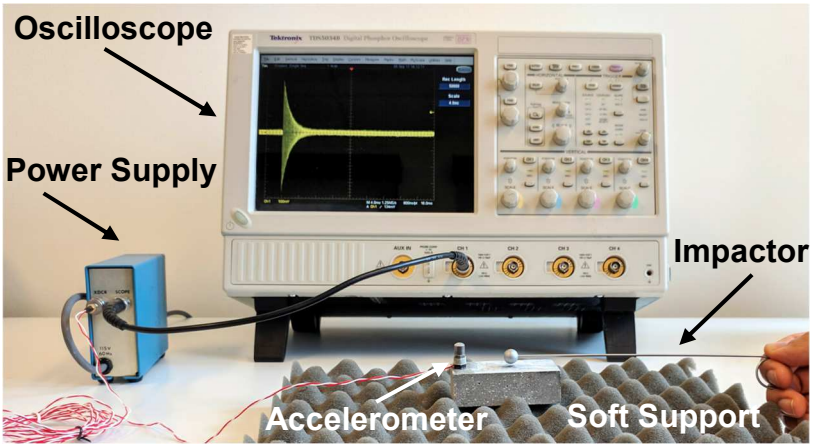

Figure 44. NIRAS experimental setup for measuring the acoustic nonlinearity of microwave samples.

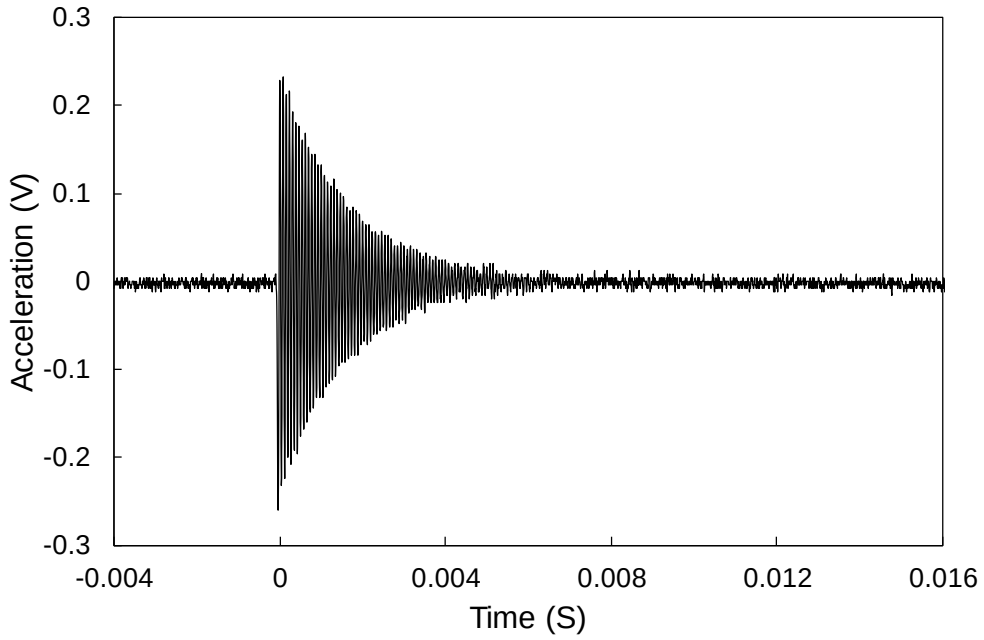

Figure 45. A sample of the time domain signal during NIRAS measurement of microwave samples.

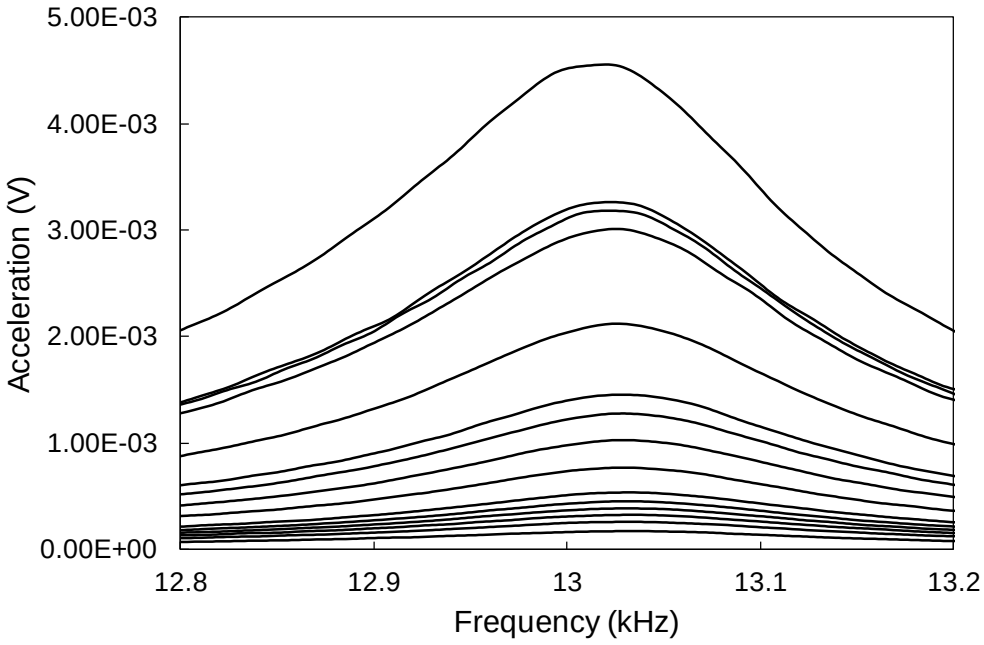

(a)

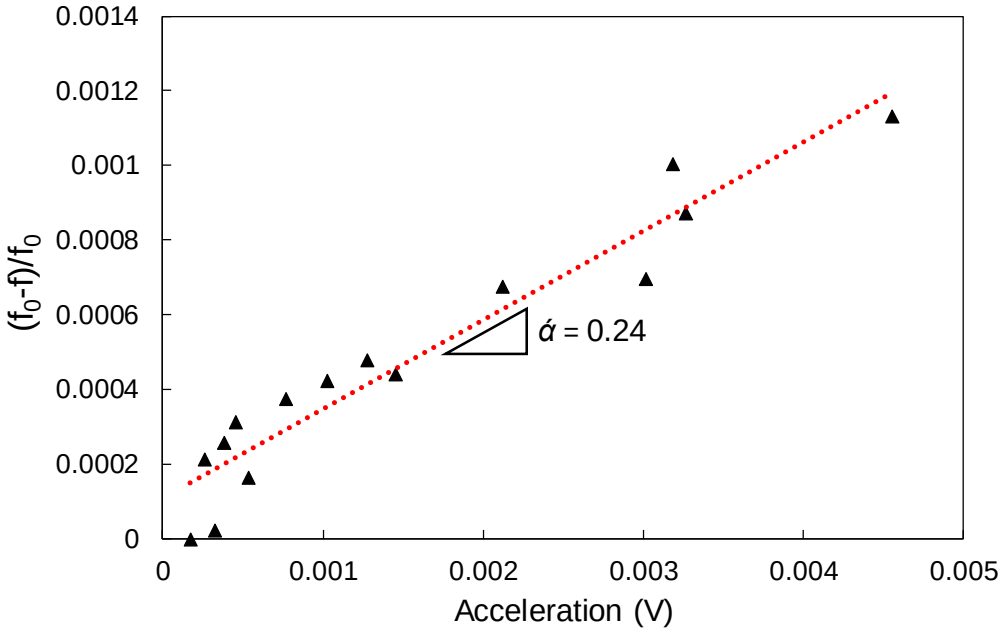

(b)

Figure 46. (a) Frequency domain of a sample's response to the impacts (b) evaluation of the acoustic nonlinearity of the sample.

A.3 Results and Discussion

The acoustic nonlinearity of microwave samples is in agreement with those of mortar bars measured at the end of ASTM C1260 condition (Figure 47). Similar to mortar bar results, Reactive-1 samples show the highest acoustic nonlinearity followed by Reactive-2 and Non-Reactive samples. The significantly lower acoustic nonlinearity of microwave samples than that of mortar bars is attributed to two main parameters: (a) their significantly smaller size than mortar bars (b) environmental condition. Since microwave samples have a significantly smaller size than mortar bars, at the same state of reaction and acoustic excitation level, the number of weak interfaces and their overall energy dissipation is lower than mortar bars, which results in the lower acoustic nonlinearity. The second parameter

that contributes to the significantly lower acoustic nonlinearity of microwave samples is their relative humidity. The microwave samples looked dry by the time of the experiment, while the acoustic nonlinearity of mortar bars was measured immediately after removing from the NaOH baths. It has been shown that the lower humidity of samples substantially decreases their acoustic nonlinearity [97,176]. Increase in the water saturation level of earth materials causes softening and activates further hysteresis elastic elements responsible for the acoustic nonlinearity of a material [176]. Furthermore, in the cement-based materials, the decrease in the humidity can cause supersaturation of pore solution and precipitation of reaction products in interfaces, which can reduce nonlinearity [13]. For the case of ASR-affected cement-based materials, the reduction of humidity can increase the gel viscosity and its elastic modulus. The drop of acoustic nonlinearity due to the decrease in the moisture content seems to dominate its potential increase due to the drying shrinkage microcracking, and the overall nonlinearity decreases [97]. The third parameter that can contribute to the lower nonlinearity of microwave samples is the temperature during the experiment. In contrast to mortar bars, which were tested immediately after removing from the 80 °C NaOH baths, the temperature of microwave samples during the test was identical to the lab temperature (23 ± 1.5 °C). At the same damage level, the nonlinearity of ASR-affected members can increase with temperature [177]. Despite the differences between the acoustic nonlinearity of mortar bars and microwave samples, the agreement between those measures suggests the validity of performing NIRAS on small samples, which allows for the multiphysics study of cement-based materials on the same sample.

The acoustic nonlinearity of microwave samples also shows higher variability than mortar bars. This observation is most likely due to the variation in the thickness of

microwave samples, which affects the diffusion of alkali ions into the samples and their damage level. In contrast, the geometry of mortar bars are approximately the same, and the standard deviation of nonlinearity parameter in those samples is mainly attributed due to the non-uniform distribution of ASR reactive sites.

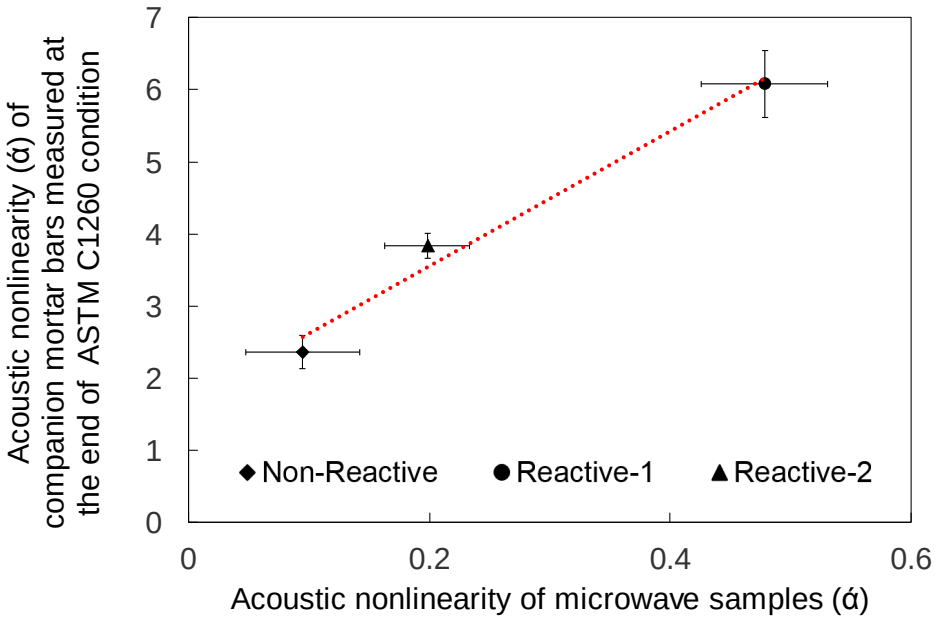

Figure 47. Acoustic nonlinearity of microwave samples versus that of mortar bars at the end of ASTM C1260 condition.

A.4 Summary

The acoustic nonlinearity of microwave samples prepared for the S-band frequency range measurements is substantially lower, but in agreement with than that of mortar bars at the end of ASTM C1260 condition. This observation is attributed to the significantly smaller size of microwave samples, and their lower moisture content and temperature than mortar bars at the time of the experiment. Overall, this chapter creates opportunities for the multiphysics study of materials where NIRAS evaluates the progression of damage, and

microwave measurements provide information about the change in the physical and chemical properties of the same sample.

REFERENCES

[1] R.G. Charlwood, Z. V Solymar, Long-term management of AAR-affected structures - An international perspective, in: Committee on Large Dams, Denver, CO (United States), United States, 1995. http://www.osti.gov/scitech/servlets/purl/192153.

[2] T. Ichikawa, T. Kimura, Effect of nuclear radiation on alkali-silica reaction of concrete, J. Nucl. Sci. Technol. 44 (2007) 1281–1284.

[3] I. Pignatelli, A. Kumar, K.G. Field, B. Wang, Y. Yu, Y. Le Pape, M. Bauchy, G. Sant, Direct experimental evidence for differing reactivity alterations of minerals following irradiation: the case of calcite and quartz, Sci. Rep. 6 (2016).

[4] K.G. Field, I. Remec, Y. Le Pape, Radiation effects in concrete for nuclear power plants - Part I: Quantification of radiation exposure and radiation effects, Nucl. Eng. Des. 282 (2015) 126–143. doi:10.1016/j.nucengdes.2014.10.003.

[5] Y. Le Pape, K.G. Field, I. Remec, Radiation effects in concrete for nuclear power plants, Part II: Perspective from micromechanical modeling, Nucl. Eng. Des. 282 (2015) 144–157.

[6] V.E. Saouma, M.A. Hariri-Ardebili, A proposed aging management program for alkali silica reactions in a nuclear power plant, Nucl. Eng. Des. 277 (2014) 248–264.

[7] M.D.A. Thomas, B. Fournier, K.J. Folliard, J.H. Ideker, Y. Resendez, The Use of Lithium to Prevent or Mitigate Alkali-Silica Reactions in Concrete Pavements and Structures, 2007.

[8] A. Hashemi, K.M. Donnell, R. Zoughi, M. Rashidi, K.E. Kurtis, Effect of exposure conditions on the long-term dielectric properties of mortar samples containing ASR gel, in: AIP Conf. Proc., AIP Publishing, 2017: p. 120004.

[9] M.D.A. Thomas, T. Ramlochan, Field cases of delayed ettringite formation, Int. RILEM TC. (2002) 85–97.

[10] M. Thomas, K. Folliard, T. Drimalas, T. Ramlochan, Diagnosing delayed ettringite formation in concrete structures, Cem. Concr. Res. 38 (2008) 841–847.

[11] R.A. Livingston, C. Ormsby, A.M. Amde, M.S. Ceary, N. McMorris, P.G. Finnerty, Field survey of delayed ettringite formation-related damage in concrete bridges in the State of Maryland, Spec. Publ. 234 (2006) 251–268.

[12] R.C. Mielenz, S.L. Marusin, W.G. Hime, Z.T. Jugovic, Investigation of Prestressed Concrete Raiway Tie Distress, Concr. Int. 17 (1995) 62–68.

[13] M. Rashidi, A. Paul, J.-Y. Kim, L.J. Jacobs, K.E. Kurtis, Insights into delayed ettringite formation damage through acoustic nonlinearity, Cem. Concr. Res. 95 (2017) 1–8. doi:10.1016/j.cemconres.2017.02.004.

[14] K.J. Leśnicki, J.-Y. Kim, K.E. Kurtis, L.J. Jacobs, Characterization of ASR damage in concrete using nonlinear impact resonance acoustic spectroscopy technique, NDT E Int. 44 (2011) 721–727. doi:10.1016/j.ndteint.2011.07.010.

[15] V.E. Nazarov, L.A. Ostrovsky, I.A. Soustova, A.M. Sutin, Nonlinear acoustics of micro-inhomogeneous media, Phys. Earth Planet. Inter. 50 (1988) 65–73. doi:10.1016/0031-9201(88)90094-5.

[16] T.E. Stanton, Expansion of concrete through reaction between cement and aggregate, Am. Soc. Civ. Eng. 66 (1940) 1781–1811.

[17] L.S.D. Glasser, N. Kataoka, The chemistry of "alkali-aggregate"reaction, Cem. Concr. Res. 11 (1981) 1–9.

[18] F. Gaboriaud, A. Nonat, D. Chaumont, A. Craievich, Aggregation and Gel Formation in Basic Silico− Calco− Alkaline Solutions Studied: A SAXS, SANS, and ELS Study, J. Phys. Chem. B. 103 (1999) 5775–5781.

[19] R.F. Bleszynski, M.D.A. Thomas, Microstructural studies of alkali-silica reaction in fly ash concrete immersed in alkaline solutions, Adv. Cem. Based Mater. 7 (1998) 66–78.

[20] M. Prezzi, P.J.M. Monteiro, G. Sposito, The alkali–silica reaction: Part I. Use of the double-layer theory to explain the behavior of reaction-product gels, ACI Mater. J. 94 (1997) 10–17.

[21] F. Rajabipour, E. Giannini, C. Dunant, J.H. Ideker, M.D.A. Thomas, Alkali–silica reaction: current understanding of the reaction mechanisms and the knowledge gaps, Cem. Concr. Res. 76 (2015) 130–146.

[22] S. Chatterji, N. Thaulow, A.D. Jensen, Studies of alkali-silica reaction. Part 4. Effect of different alkali salt solutions on expansion, Cem. Concr. Res. 17 (1987) 777–783.

[23] N. Marinoni, M. Voltolini, L. Mancini, F. Cella, Influence of aggregate mineralogy on alkali–silica reaction studied by X-ray powder diffraction and imaging techniques, J. Mater. Sci. 47 (2012) 2845–2855.

[24] N. Thaulow, U.H. Jakobsen, B. Clark, Composition of alkali silica gel and ettringite in concrete railroad ties: SEM-EDX and X-ray diffraction analyses, Cem. Concr. Res. 26 (1996) 309–318.

[25] M. Rashidi, A. Paul, K.E. Kurtis, Investigating the Role of Alkalis in the Alkali-Silica Reaction (ASR) Sol and Gel, Cem. Concr. Res. (In Prep. (n.d.).

[26] L.-O. Nilsson, Moisture effects on the alkali-silica reaction, in: Proc., 1983.

[27] U. Ludwig, Effects of environmental conditions on alkali-aggregate reaction and preventive measures, in: Proc. 8th Int. Conf. AlkaliąAggregate React. Japan Soc. Mater. Sci. Kyoto, 1989: p. 583ą596.

[28] H. Olafsson, The effect of relative humidity and temperature on alkali expansion of mortar bars, in: Proc., 7th Int. Conf. Alkali Aggreg. React. Concr., 1986: pp. 461–465.

[29] D.W. Hobbs, Alkali-silica reaction in concrete, Thomas Telford Publishing, 1988.

[30] A.G. Vayghan, F. Rajabipour, J.L. Rosenberger, Composition–rheology relationships in alkali–silica reaction gels and the impact on the Gel's deleterious behavior, Cem. Concr. Res. 83 (2016) 45–56.

[31] X. Hou, R.J. Kirkpatrick, L.J. Struble, P.J.M. Monteiro, Structural investigations of alkali silicate gels, J. Am. Ceram. Soc. 88 (2005) 943–949.

[32] X. Hou, L.J. Struble, R.J. Kirkpatrick, Formation of ASR gel and the roles of CSH and portlandite, Cem. Concr. Res. 34 (2004) 1683–1696.

[33] R.J. Kirkpatrick, A.G. Kalinichev, X. Hou, L. Struble, Experimental and molecular dynamics modeling studies of interlayer swelling: water incorporation in kanemite and ASR gel, Mater. Struct. 38 (2005) 449–458.

[34] L.A.J. Garvie, B. Devouard, T.L. Groy, F. Cámara, P.R. Buseck, Crystal structure of kanemite, NaHSi2O5· 3H2O, from the Aris phonolite, Namibia, Am. Mineral. 84 (1999) 1170–1175.

[35] F. Gaboriaud, A. Nonat, D. Chaumont, A. Craievich, Aggregation processes and formation of silico-calco-alkaline gels under high ionic strength, J. Colloid Interface Sci. 253 (2002) 140–149.

[36] T. Ichikawa, M. Miura, Modified model of alkali-silica reaction, Cem. Concr. Res. 37 (2007) 1291–1297.

[37] K.R. Iler, The chemistry of silica, Solubility, Polym. Colloid Surf. Prop. Biochem. Silica. (1979).

[38] P.H. Bolt, T.P.M. Beelen, R.A. Van Santen, A small angle X-ray scattering study on high pH silica precipitations, Colloids Surfaces A Physicochem. Eng. Asp. 122 (1997) 183–187.

[39] C. Huang, A.N. Cormack, Structural differences and phase separation in alkali silicate glasses, J. Chem. Phys. 95 (1991) 3634–3642.

[40] A. Gholizadeh-Vayghan, F. Rajabipour, The influence of alkali–silica reaction (ASR) gel composition on its hydrophilic properties and free swelling in contact with water vapor, Cem. Concr. Res. 94 (2017) 49–58.

[41] A. Gholizadeh-Vayghan, F. Rajabipour, Quantifying the swelling properties of alkali-silica reaction (ASR) gels as a function of their composition, J. Am. Ceram. Soc. 100 (2017) 3801–3818.

[42] Standard Specification for Portland Cement, ASTM International, West

Conshohocken, PA, (2017).

[43] A.G. Volkov, S. Paula, D.W. Deamer, Two mechanisms of permeation of small neutral molecules and hydrated ions across phospholipid bilayers, Bioelectrochemistry Bioenerg. 42 (1997) 153–160. doi:10.1016/S0302-4598(96)05097-0.

[44] A. V McCormick, A.T. Bell, C.J. Radke, Evidence from alkali-metal NMR spectroscopy for ion pairing in alkaline silicate solutions, J. Phys. Chem. 93 (1989) 1733–1737.

[45] P. Wijnen, T.P.M. Beelen, J.W. De Haan, C.P.J. Rummens, L.J.M. Van de Ven, R.A. Van Santen, Silica gel dissolution in aqueous alkali metal hydroxides studied by 29Si□ NMR, J. Non. Cryst. Solids. 109 (1989) 85–94.

[46] Standard Test Method for Potential Alkali Reactivity of Aggregates (Mortar-Bar Method), West Conshohocken, PA: ASTM International, (2014).

[47] Standard Test Method for Determination of Length Change of Concrete Due to Alkali-Silica Reaction, ASTM International, West Conshohocken, PA, (2015).

[48] Standard Test Method for Potential Alkali Reactivity of Cement-Aggregate Combinations (Mortar-Bar Method), ASTM International, West Conshohocken, PA, (2010).

[49] Standard Test Method for Determining the Potential Alkali-Silica Reactivity of Combinations of Cementitious Materials and Aggregate (Accelerated Mortar-Bar Method), ASTM International, West Conshohocken, PA, (2013).

[50] CSA A23.2-27A, Standard practice to identify degree of alkali-reactivity of aggregates and to identify measures to avoid deleterious expansion in concrete, CSA A23.2-00 Methods of Test for Concrete, Canadian Standards Association, Toronto, Canada, (2000).

[51] CSA A23.2-28A, Standard practice for laboratory testing to demonstrate the effectiveness of supplementary cement materials and chemical admixtures to prevent alkali–silica reaction in concrete, CSA A23.2-00 Methods of Test for Concrete, Canadian Standards, (2004).

[52] CSA-A23.2-14A, Potential Expansivity of Aggregates; Procedure for Length Change Due to Alkali-Aggregate Reaction in Concrete Prisms,CSA A23.2-00 Methods of Test for Concrete, Canadian Standards, (2014).

[53] CSA-A23.2-25A, Test Method for Detection of Alkali-Silica Reactive Aggregate by Accelerated Expansion of Mortar Bars, CSA A23.2-00 Methods of Test for Concrete, Canadian Standards, (n.d.).

[54] AASHTO T 303-00. Standard method of test for accelerated detection of potentially deleterious expansion of mortar bars due to alkali–silica reaction. Standard specifications for transportation materials and methods of sampling and testing part

2B: tests, , (2006).

[55] L.A. Feigin, D.I. Svergun, Structure analysis by small-angle X-ray and neutron scattering, Springer, 1987.

[56] P.W.J.G. Wijnen, T.P.M. Beelen, K.P.J. Rummens, H.C.P.L. Saeijs, R.A. van Santen, Silica gel from water glass: a SAXS study of the formation and ageing of fractal aggregates, J. Appl. Crystallogr. 24 (1991) 759–764.

[57] F. Gaboriaud, A. Nonat, D. Chaumont, A. Craievich, B. Hanquet, 29Si NMR and small-angle X-ray scattering studies of the effect of alkaline ions (Li^+, Na^+, and K^+) in silico-alkaline sols, J. Phys. Chem. B. 103 (1999) 2091–2099.

[58] C.J. Brinker, G.W. Scherer, Sol→ gel→ glass: I. Gelation and gel structure, J. Non. Cryst. Solids. 70 (1985) 301–322.

[59] X.-D. Cong, R.J. Kirkpatrick, S. Diamond, 29Si MAS NMR spectroscopic investigation of alkali silica reaction product gels, Cem. Concr. Res. 23 (1993) 811–823.

[60] C.E. Tambelli, J.F. Schneider, N.P. Hasparyk, P.J.M. Monteiro, Study of the structure of alkali–silica reaction gel by high-resolution NMR spectroscopy, J. Non. Cryst. Solids. 352 (2006) 3429–3436.

[61] P. Duxson, G.C. Lukey, F. Separovic, J.S.J. Van Deventer, Effect of alkali cations on aluminum incorporation in geopolymeric gels, Ind. Eng. Chem. Res. 44 (2005) 832–839.

[62] J.W. Phair, R.A. Livingston, C.M. Brown, A.J. Benesi, Investigation of the state of water in hydrating layered sodium disilicate in crystalline and amorphous forms by quasi-elastic neutron scattering, Chem. Mater. 16 (2004) 5042–5050.

[63] M. Xia, H. Shi, X. Guo, Probing the structural evolution during the geopolymerization process at an early age using proton NMR spin-lattice relaxation, Mater. Lett. 136 (2014) 222–224.

[64] J.L. Provis, J.S.J. Van Deventer, Alkali Activated Materials, Springer, Dordrecht, 2014. doi:10.1007/978-94-007-7672-2.

[65] H.F.W. Taylor, C. Famy, K.L. Scrivener, Delayed ettringite formation, Cem. Concr. Res. 31 (2001) 683–693.

[66] R. Yang, C.D. Lawrence, C.J. Lynsdale, J.H. Sharp, Delayed ettringite formation in heat-cured Portland cement mortars, Cem. Concr. Res. 29 (1999) 17–25.

[67] E. L'Hôpital, B. Lothenbach, G. Le Saout, D. Kulik, K. Scrivener, Incorporation of aluminium in calcium-silicate-hydrates, Cem. Concr. Res. 75 (2015) 91–103.

[68] T. Ramlochan, M.D.A. Thomas, R.D. Hooton, The effect of pozzolans and slag on the expansion of mortars cured at elevated temperature: Part II: Microstructural and

microchemical investigations, Cem. Concr. Res. 34 (2004) 1341–1356.

[69] S.L. Tracy, S.R. Boyd, J.D. Connolly, Effect of curing temperature and cement chemistry on the potential for concrete expansion due to DEF, PCI J. 49 (2004) 46–57.

[70] E. Grabowski, B. Czarnecki, J.E. Gillott, C.R. Duggan, J.F. Scott, Rapid test of concrete expansivity due to internal sulfate attack, Mater. J. 89 (1992) 469–480.

[71] A. Pavoine, X. Brunetaud, L. Divet, The impact of cement parameters on Delayed Ettringite Formation, Cem. Concr. Compos. 34 (2012) 521–528.

[72] F.P. Glasser, The role of sulfate mineralogy and cure temperature in delayed ettringite formation, Cem. Concr. Compos. 18 (1996) 187–193.

[73] S. Kelham, The effect of cement composition and fineness on expansion associated with delayed ettringite formation, Cem. Concr. Compos. 18 (1996) 171–179.

[74] R.J. Flatt, G.W. Scherer, Thermodynamics of crystallization stresses in DEF, Cem. Concr. Res. 38 (2008) 325–336.

[75] K. Tosun, B. Baradan, Effect of ettringite morphology on DEF-related expansion, Cem. Concr. Compos. 32 (2010) 271–280.

[76] C. Famy, H.F.W. Taylor, Ettringite in hydration of Portland cement concrete and its occurrence in mature concretes, Mater. J. 98 (2001) 350–356.

[77] H.M.Z. Al-Abidien, Aggregates in Saudi Arabia: a survey of their properties and suitability for concrete, Mater. Struct. 20 (1987) 260–264. doi:10.1007/BF02485921.

[78] H.N. Atahan, D. Dikme, Use of mineral admixtures for enhanced resistance against sulfate attack, Constr. Build. Mater. 25 (2011) 3450–3457. doi:10.1016/j.conbuildmat.2011.03.036.

[79] A. Paul, K.E. Kurtis, L.F. Kahn, P.M. Singh, Assessment of Sand Quality on Concrete Performance : Examination of Acidic and Sulfate / Sulfide-Bearing Sands, 2014.

[80] A. Rodrigues, J. Duchesne, B. Fournier, B. Durand, P. Rivard, M. Shehata, Mineralogical and chemical assessment of concrete damaged by the oxidation of sulfide-bearing aggregates: Importance of thaumasite formation on reaction mechanisms, Cem. Concr. Res. 42 (2012) 1336–1347. doi:10.1016/j.cemconres.2012.06.008.

[81] W.H. Anderson, Foundation problems and pyrite oxidation in the Chattanooga Shale, Estill County, Kentucky, (2008). http://kgs.uky.edu/kgsweb/PubsSearching/MoreInfo.asp?titleInput=17221&map=0.

[82] K. Wille, R. Zhong, Investigating the Deterioration of Basement Walls Made of Concrete in CT, Department of Civil and Environmental Engineering, Advanced Cementitious Materials and Composites Laboratory, University of Connecticut, 2016.

[83] N. Petrov, A. Tagnit-Hamou, Is microcracking really a precursor to delayed ettringite formation and consequent expansion?, ACI Mater. J. 101 (2004) 442–447.

[84] G. Tovar-Rodríguez, M. Barra, S. Pialarissi, D. Aponte, E. Vázquez, Expansion of mortars with gypsum contaminated fine recycled aggregates, Constr. Build. Mater. 38 (2013) 1211–1220.

[85] P.K. Mehta, P.J.M. Monteiro, Concrete: microstructure, properties, and materials. 2006, (2006).

[86] S. Mindess, J.F. Young, D. Darwin, Concrete, Prentice Hall, 2003.

[87] M. Sargolzahi, S.A. Kodjo, P. Rivard, J. Rhazi, Effectiveness of nondestructive testing for the evaluation of alkali–silica reaction in concrete, Constr. Build. Mater. 24 (2010) 1398–1403.

[88] J. Chen, A.R. Jayapalan, J.-Y. Kim, K.E. Kurtis, L.J. Jacobs, Rapid evaluation of alkali–silica reactivity of aggregates using a nonlinear resonance spectroscopy technique, Cem. Concr. Res. 40 (2010) 914–923. doi:10.1016/j.cemconres.2010.01.003.

[89] R.A. Guyer, P.A. Johnson, Nonlinear mesoscopic elasticity: Evidence for a new class of materials, Phys. Today. 52 (1999) 30–36.

[90] V.E. Nazarov, A.M. Sutin, Nonlinear elastic constants of solids with cracks, J. Acoust. Soc. Am. 102 (1997) 3349–3354.

[91] K.-A. Van Den Abeele, P.A. Johnson, A. Sutin, Nonlinear elastic wave spectroscopy (NEWS) techniques to discern material damage, part I: nonlinear wave modulation spectroscopy (NWMS), Res. Nondestruct. Eval. 12 (2000) 17–30.

[92] K.H. Matlack, J.-Y. Kim, L.J. Jacobs, J. Qu, Review of second harmonic generation measurement techniques for material state determination in metals, J. Nondestruct. Eval. 34 (2015) 273.

[93] M.F. Hamilton, D.T. Blackstock, Nonlinear acoustics, Academic press San Diego, 1998.

[94] I.Y. Solodov, Ultrasonics of non-linear contacts: propagation, reflection and NDE-applications, Ultrasonics. 36 (1998) 383–390.

[95] M. Rashidi, M.C.L. Knapp, A. Hashemi, J.-Y. Kim, K.M. Donnell, R. Zoughi, L.J. Jacobs, K.E. Kurtis, Detecting alkali-silica reaction: A multi-physics approach, Cem. Concr. Compos. 73 (2016). doi:10.1016/j.cemconcomp.2016.07.001.

[96] J.A. Ten Cate, T.J. Shankland, Slow dynamics in the nonlinear elastic response of Berea sandstone, Geophys. Res. Lett. 23 (1996) 3019–3022.

[97] J.N. Eiras, J.S. Popovics, M. V Borrachero, J. Monzó, J. Payá, The effects of moisture and micro-structural modifications in drying mortars on vibration-based NDT methods, Constr. Build. Mater. 94 (2015) 565–571.

[98] V. Genovés, L. Soriano, M. V Borrachero, J. Eiras, J. Payá, Preliminary study on short-term sulphate attack evaluation by non-linear impact resonance acoustic spectroscopy technique, Constr. Build. Mater. 78 (2015) 295–302.

[99] J. Chen, L. Zhang, Experimental study of effects of water–cement ratio and curing time on nonlinear resonance of concrete, Mater. Struct. 48 (2015) 423–433.

[100] J.N. Eiras, T. Kundu, J.S. Popovics, J. Monzó, L. Soriano, J. Payá, Evaluation of frost damage in cement-based materials by a nonlinear elastic wave technique, in: SPIE Smart Struct. Mater. Nondestruct. Eval. Heal. Monit., International Society for Optics and Photonics, 2014: p. 90641G–90641G.

[101] J. Chen, R. Bharata, T. Yin, Q. Wang, H. Wang, T. Zhang, Assessment of sulfate attack and freeze–thaw cycle damage of cement-based materials by a nonlinear acoustic technique, Mater. Struct. 50 (2017) 105.

[102] I. Ben Ammar, A. El Mahi, C. Karra, R. El Guerjouma, M. Haddar, Characterization of sandwich beams with shear damages by linear and nonlinear vibration methods, J. Compos. Mater. (2017) 21998317702436.

[103] J. Jin, M.G. Moreno, J. Riviere, P. Shokouhi, Impact-Based Nonlinear Acoustic Testing for Characterizing Distributed Damage in Concrete, J. Nondestruct. Eval. 36 (2017) 51.

[104] U. Dahlen, N. Ryden, A. Jakobsson, Damage identification in concrete using impact non-linear reverberation spectroscopy, Ndt E Int. 75 (2015) 15–25.

[105] S.-J. Park, H.J. Yim, H.-G. Kwak, Nonlinear resonance vibration method to estimate the damage level on heat-exposed concrete, Fire Saf. J. 69 (2014) 36–42.

[106] K.E.A. Van Den Abeele, P.A. Johnson, R.A. Guyer, K.R. McCall, On the quasi-analytic treatment of hysteretic nonlinear response in elastic wave propagation, J. Acoust. Soc. Am. 101 (1997) 1885–1898.

[107] K.-A. Van Den Abeele, J. Carmeliet, J.A. Ten Cate, P.A. Johnson, Nonlinear elastic wave spectroscopy (NEWS) techniques to discern material damage, Part II: Single-mode nonlinear resonance acoustic spectroscopy, J. Res. Nondestruct. Eval. 12 (2000) 31–42.

[108] V. Aleshin, K. Van Den Abeele, Microcontact-based theory for acoustics in microdamaged materials, J. Mech. Phys. Solids. 55 (2007) 366–390.

[109] J.-Y. Kim, A. Baltazar, S.I. Rokhlin, Ultrasonic assessment of rough surface contact

between solids from elastoplastic loading–unloading hysteresis cycle, J. Mech. Phys. Solids. 52 (2004) 1911–1934.

[110] A.S. Kodjo, P. Rivard, F. Cohen-Tenoudji, J.-L. Gallias, Impact of the alkali–silica reaction products on slow dynamics behavior of concrete, Cem. Concr. Res. 41 (2011) 422–428.

[111] M. Liu, G. Tang, L.J. Jacobs, J. Qu, A nonlinear wave mixing method for detecting Alkali-Silica reactivity of aggregates, in: AIP Conf. Proc., AIP, 2012: pp. 1524–1531.

[112] X.J. Chen, J.-Y. Kim, K.E. Kurtis, J. Qu, C.W. Shen, L.J. Jacobs, Characterization of progressive microcracking in Portland cement mortar using nonlinear ultrasonics, NDT E Int. 41 (2008) 112–118.

[113] F. Moradi-Marani, S.A. Kodjo, P. Rivard, C.-P. Lamarche, Nonlinear acoustic technique of time shift for evaluation of alkali-silica reaction damage in concrete structures, ACI Mater. J. 111 (2014) 581–592.

[114] J.A. TenCate, New nonlinear acoustic techniques for NDE, in: AIP Conf. Proc., AIP, 2001: pp. 1229–1235.

[115] J.A. TenCate, E. Smith, L.W. Byers, A.S. Michel, Nonlinear resonant ultrasound for damage detection, in: AIP Conf. Proc., AIP, 2000: pp. 1387–1392.

[116] P.A. Johnson, J.A. TenCate, R.A. Guyer, K.E.A. Van Den Abeele, Resonant nonlinear ultrasound spectroscopy, (2001).

[117] K.J. Leśnicki, J.-Y. Kim, K.E. Kurtis, L.J. Jacobs, Assessment of alkali--silica reaction damage through quantification of concrete nonlinearity, Mater. Struct. 46 (2013) 497–509. doi:10.1617/s11527-012-9942-y.

[118] Y. Boukari, D. Bulteel, P. Rivard, N.-E. Abriak, Combining nonlinear acoustics and physico-chemical analysis of aggregates to improve alkali–silica reaction monitoring, Cem. Concr. Res. 67 (2015) 44–51. doi:10.1016/j.cemconres.2014.08.005.

[119] T. Ju, J.D. Achenbach, L.J. Jacobs, M. Guimaraes, J. Qu, Ultrasonic nondestructive evaluation of alkali–silica reaction damage in concrete prism samples, Mater. Struct. 50 (2017) 60.

[120] G. Kim, E. Giannini, N. Klenke, J.-Y. Kim, K.E. Kurtis, L.J. Jacobs, Measuring Alkali-Silica Reaction (ASR) Microscale Damage in Large-Scale Concrete Slabs Using Nonlinear Rayleigh Surface Waves, J. Nondestruct. Eval. 36 (2017) 29.

[121] J. Zhang, J.L. Provis, D. Feng, J.S.J. van Deventer, Geopolymers for immobilization of Cr^{6+}, Cd^{2+}, and Pb^{2+}, J. Hazard. Mater. 157 (2008) 587–598.

[122] A. Paul, Understanding the Role of Materials in the Durability of Prestressed Concrete in Marine Environments, (2015).

[123] K.J. Folliard, R. Barborak, T. Drimalas, L. Du, S. Garber, J. Ideker, T. Ley, S. Williams, M. Juenger, B. Fournier, Preventing ASR/DEF in new concrete: Final report, Cent. Transp. Res. Univ. Texas Austin. Fed. Highw. Adm. Rep. FHWA/TX-06/0-4085-5. (2006).

[124] S. Kelham, Effect of cement composition and hydration temperature on volume stability of mortar, in: Proc. 10th Int. Congr. Chem. Cem. 1997, 1997: p. 4.

[125] M.C. Lewis, K.L. Scrivener, S. Kelham, Heat curing and delayed ettringite formation, MRS Online Proc. Libr. Arch. 370 (1994).

[126] S. Bauer, B. Cornell, D. Figurski, T. Ley, J. Miralles, K. Folliard, Alkali-silica reaction and delayed ettringite formation in concrete: A literature review, 2006.

[127] J. Zhao, Data processing for the SNS EQ-SANS diffractometer, Nucl. Instruments Methods Phys. Res. Sect. A Accel. Spectrometers, Detect. Assoc. Equip. 647 (2011) 107–111.

[128] Operating Instructions MARAN 23 Ultra Magnetic Resonance Analyzer, (n.d.).

[129] S. Meiboom, D. Gill, Modified spin-echo method for measuring nuclear relaxation times, Rev. Sci. Instrum. 29 (1958) 688–691.

[130] P. Rivard, B. Fournier, G. Ballivy, The damage rating index method for ASR affected concrete—a critical review of petrographic features of deterioration and evaluation criteria, Cem. Concr. Aggregates. 24 (2002) 1–11.

[131] P.E. Grattan-Bellew, Laboratory evaluation of alkali-silica reaction in concrete from Saunders Generating Station, Mater. J. 92 (1995) 126–134.

[132] P. Rivard, G. Ballivy, Assessment of the expansion related to alkali-silica reaction by the Damage Rating Index method, Constr. Build. Mater. 19 (2005) 83–90.

[133] K.C. Natesaiyer, K.C. Hover, Further study of an in-situ identification method for alkali-silica reaction products in concrete, Cem. Concr. Res. 19 (1989) 770–778.

[134] C. ASTM, 856 (2004):"Standard Practice for Petrographic Examination of Hardened Concrete," ASTM Int. West Conshohocken. (n.d.).

[135] J. Teixeira, Small-angle scattering by fractal systems, J. Appl. Crystallogr. 21 (1988) 781–785.

[136] D.W. Schaefer, K.D. Keefer, Structure of random porous materials: silica aerogel, Phys. Rev. Lett. 56 (1986) 2199.

[137] Hammouda, B., Scattering From Fractal Systems, (2016). https://www.ncnr.nist.gov/staff/hammouda/distance_learning/chapter_33.pdf.

[138] M. Carpineti, M. Giglio, Transition from semiorder to disorder in the aggregation of dense colloidal solutions, Phys. Rev. Lett. 70 (1993) 3828.

[139] T.A. Witten Jr, L.M. Sander, Diffusion-limited aggregation, a kinetic critical phenomenon, Phys. Rev. Lett. 47 (1981) 1400.

[140] Vicsek, T., Fractal growth phenomena, World scientific, Singapore, 1992.

[141] M. Kolb, R. Jullien, Chemically limited versus diffusion limited aggregation, J. Phys. Lettres. 45 (1984) 977–981.

[142] M. Kallala, R. Jullien, B. Cabane, Crossover from gelation to precipitation, J. Phys. II. 2 (1992) 7–25.

[143] P.W.J.G. Wijnen, T.P.M. Beelen, K.P.J. Rummens, H.C.P.L. Saeijs, J.W. De Haan, L.J.M. Van De Ven, R.A. Van Santen, The molecular basis of aging of aqueous silica gel, J. Colloid Interface Sci. 145 (1991) 17–32.

[144] P.W.J.G. Wijnenl, T.P.M. Beelen, R.A. van Santen, Silica Gels from Aqueous Silicate Solutions, Colloid Chem. Silica. (1994) 517–531.

[145] R.W. Pekala, D.W. Schaefer, Structure of organic aerogels. 1. Morphology and scaling, Macromolecules. 26 (1993) 5487–5493.

[146] A. Hasmy, R. Vacher, R. Jullien, Small-angle scattering by fractal aggregates: A numerical investigation of the crossover between the fractal regime and the Porod regime, Phys. Rev. B. 50 (1994) 1305.

[147] E. Lifshin, X-ray Characterization of Materials, John Wiley & Sons, 2008.

[148] H. Akaike, A new look at the statistical model identification, IEEE Trans. Automat. Contr. 19 (1974) 716–723.

[149] A. Amiri, G. Øye, J. Sjöblom, Influence of pH, high salinity and particle concentration on stability and rheological properties of aqueous suspensions of fumed silica, Colloids Surfaces A Physicochem. Eng. Asp. 349 (2009) 43–54.

[150] L.H. Allen, E. Matijević, Stability of colloidal silica: I. Effect of simple electrolytes, J. Colloid Interface Sci. 31 (1969) 287–296.

[151] J. Depasse, A. Watillon, The stability of amorphous colloidal silica, J. Colloid Interface Sci. 33 (1970) 430–438.

[152] J. Depasse, Coagulation of colloidal silica by alkaline cations: Surface dehydration or interparticle bridging?, J. Colloid Interface Sci. 194 (1997) 260–262.

[153] J. Depasse, Simple experiments to emphasize the main characteristics of the coagulation of silica hydrosols by alkaline cations: Application to the analysis of the model of Colic et al., J. Colloid Interface Sci. 220 (1999) 174–176.

[154] P.G. Hartley, I. Larson, P.J. Scales, Electrokinetic and direct force measurements between silica and mica surfaces in dilute electrolyte solutions, Langmuir. 13 (1997) 2207–2214.

[155] G. Peschel, P. Belouschek, M.M. Müller, M.R. Müller, R. König, The interaction of solid surfaces in aqueous systems, Colloid Polym. Sci. 260 (1982) 444–451.

[156] J.-P. Chapel, Electrolyte species dependent hydration forces between silica surfaces, Langmuir. 10 (1994) 4237–4243.

[157] M. Colic, G. V Franks, M.L. Fisher, F.F. Lange, Effect of counterion size on short range repulsive forces at high ionic strengths, Langmuir. 13 (1997) 3129–3135.

[158] T.F. Tadros, J. Lyklema, Adsorption of potential-determining ions at the silica-aqueous electrolyte interface and the role of some cations, J. Electroanal. Chem. Interfacial Electrochem. 17 (1968) 267–275.

[159] F.A. Rodrigues, P.J.M. Monteiro, G. Sposito, The alkali-silica reaction: The surface charge density of silica and its effect on expansive pressure, Cem. Concr. Res. 29 (1999) 527–530. doi:http://dx.doi.org/10.1016/S0008-8846(98)00220-8.

[160] P. Hudon, D.R. Baker, The nature of phase separation in binary oxide melts and glasses. I. Silicate systems, J. Non. Cryst. Solids. 303 (2002) 299–345.

[161] A. Valori, P.J. McDonald, K.L. Scrivener, The morphology of C–S–H: Lessons from 1 H nuclear magnetic resonance relaxometry, Cem. Concr. Res. 49 (2013) 65–81.

[162] J.R. Zimmerman, W.E. Brittin, Nuclear magnetic resonance studies in multiple phase systems: lifetime of a water molecule in an adsorbing phase on silica gel, J. Phys. Chem. 61 (1957) 1328–1333.

[163] P. Steins, A. Poulesquen, F. Frizon, O. Diat, J. Jestin, J. Causse, D. Lambertin, S. Rossignol, Effect of aging and alkali activator on the porous structure of a geopolymer, J. Appl. Crystallogr. 47 (2014) 316–324.

[164] H. Maraghechi, F. Rajabipour, C.G. Pantano, W.D. Burgos, Effect of calcium on dissolution and precipitation reactions of amorphous silica at high alkalinity, Cem. Concr. Res. 87 (2016) 1–13.

[165] V.E. Nazarov, Acoustic nonlinearity of cracks partially filled with liquid: Cubic approximation, J. Acoust. Soc. Am. 109 (2001) 2642–2648.

[166] M. Al Shamaa, S. Lavaud, L. Divet, G. Nahas, J.M. Torrenti, Influence of relative humidity on delayed ettringite formation, Cem. Concr. Compos. 58 (2015) 14–22.

[167] Z. Zhang, J. Olek, S. Diamond, Studies on delayed ettringite formation in heat-cured mortars: II. Characteristics of cement that may be susceptible to DEF, Cem. Concr. Res. 32 (2002) 1737–1742.

[168] J.H.P. Van Aardt, S. Visser, Calcium hydroxide attack on feldspars and clays: possible relevance to cement-aggregate reactions, Cem. Concr. Res. 7 (1977) 643–648.

[169] J.H.P. Van Aardt, S. Visser, Reaction of Ca $(OH)_2$ and of Ca $(OH)_2$+ CaSO4. $2H_2O$ at various temperatures with feldspars in aggregates used for concrete making, Cem. Concr. Res. 8 (1978) 677–681.

[170] J.H. van Aardt, S. Visser, Formation of hydrogarnets: calcium hydroxide attack on clays and feldspars, Cem. Concr. Res. 7 (1977) 39–44.

[171] Standard Method of Test for Nonlinear Impact Resonance Acoustic Spectroscopy (NIRAS) for Concrete Specimens with Damage from the Alkali-Silica Reaction (ASR), (2014).

[172] Standard Test Method for Resistance of Concrete to Rapid Freezing and Thawing, (2015).

[173] D. Constantiner, S. Diamond, Alkali release from feldspars into pore solutions, Cem. Concr. Res. 33 (2003) 549–554.

[174] P.A. Johnson, X. Jia, Nonlinear dynamics, granular media and dynamic earthquake triggering, Nature. 437 (2005) 871–874.

[175] A. Hashemi, M. Horst, K.E. Kurtis, K.M. Donnell, R. Zoughi, Comparison of alkali–silica reaction gel behavior in mortar at microwave frequencies, IEEE Trans. Instrum. Meas. 64 (2015) 1907–1915.

[176] K. Van Den Abeele, J. Carmeliet, P.A. Johnson, B. Zinszner, Influence of water saturation on the nonlinear elastic mesoscopic response in Earth materials and the implications to the mechanism of nonlinearity, J. Geophys. Res. Solid Earth. 107 (2002).

[177] F. Moradi-Marani, S.A. Kodjo, P. Rivard, C.-P. Lamarche, Effect of the Temperature on the Nonlinear Acoustic Behavior of Reinforced Concrete Using Dynamic Acoustoelastic Method of Time Shift, J. Nondestruct. Eval. 33 (2014) 288–298.